# EXPERIMENTAL PHASE DIAGRAM STUDIES ON THE Mg-Mn-Ce TERNARY SYSTEM AT Mg-RICH CORNER

By
Xin Zhang

A Thesis Submitted to the Faculty of Graduate Studies and Research in Partial Fulfillment of the Requirements for the Degree of Doctor of Philosophy

Department of Mining and Materials Engineering
McGill University
Montreal, Canada

January 2010
©

# ABSTRACT

The ternary Mg-Mn-Ce phase diagram was experimentally studied and thermodynamically calculated at the Mg-rich corner. More than twenty binary and ternary alloys were synthesized and heat-treated at both ambient and elevated temperatures. The microstructures and lattice parameters of the samples were studied via XRD, SEM/EDS and EPMA to determine phase equilibria. The ternary phase diagram was also calculated via thermodynamic calculation software FactSage. The results from both experiment and the assessment were compared and discussed.

The binary phase diagrams were re-examined, especially the Mg-Ce system. In order to investigate the composition range of the intermetallic compounds $Mg_{12}Ce$ and $Mg_{41}Ce_5$, and to clarify data in the existing phase diagram, both the solid-liquid diffusion couple method and alloys synthesized with target phases were analyzed. Pure Mg - Ce contact was vacuum-encapsulated in quartz tube and the Mg and Ce inter-diffused at 400$^{o}$C. Alloys prepared were cast and annealed at a temperature range of 300-550$^{o}$C. All the four single-phase zones corresponding to the Mg-Ce phase diagram were observed via the diffusion couple technique. However, the stoichiometry of $Mg_{12}Ce$ studied on the synthesized and annealed alloys showed that on the Mg rich side of the present phase diagram, the compositional range of $Mg_{12}Ce$ should be redesignated as $Mg_{(11.17-10.81)}Ce$ at ambient temperature, and $Mg_{(11.31-10.75)}Ce$ at 530$^{o}$C. $Mg_{41}Ce_5$, on the other hand, has been confirmed as a line compound, but with composition 11.3at% Ce, rather than 10.9at% Ce.

The binary phase diagram study was also extended to the Ce-rich side of Mg-Ce system. A new phase, $Mg_4Ce$, was found in the study of phase $Mg_3Ce$. Based on the investigation of the intermetallics in the Mg-Ce binary system, a modified phase

diagram was suggested to accommodate the stoichiometry of $Mg_{11}Ce$, $Mg_{39}Ce_5$, and $Mg_3Ce$.

The experimental study on the ternary phase diagram was conducted on three isopleths: 0.6, 1.8 and 2.5wt% Mn, respectively, and Ce varied between 0 and 25wt%. All alloys were synthesized from high purity starting materials. Two types of thermal analyses, namely, cooling curve analysis (CCA) and differential scanning calorimetry (DSC), were used to determine the liquidus and solid phase transformation temperatures. The heating/quenching tests on selected samples were conducted for phase analysis. The results showed that only one invariant point for ternary eutectic reaction was observed in the three isopleths, and the composition is 1wt% Mn and 22wt% Ce at 592$^{o}$C. Furthermore, a solid-solution type of ternary intermetallic compound $(Mg, Mn)_{11}Ce$ is formed, holding the same tetragonal structure as $Mg_{12}Ce$. The solid solution of Mn in $Mg_{12}Ce$ varies between 0.3~0.6 at%, depending on alloy composition and quenching temperature.

Finally, the phase diagram calculation with FactSage program was conducted and the small disagreement between the modeling results and present experimental data were found, especially for the eutectic temperature for $L \rightarrow Mg(hcp) + Mg_{12}Ce$. This is mainly because the present experimental data were not available when the thermodynamic modeling had been performed. The Gibbs energy of $Mg_{12}Ce$ phase was re-optimized and the revised data can accurately reproduce the experimental results within experimental error limits.

# RÉSUMÉ

Le diagramme de phase ternaire Mg-Mn-Ce a été étudié expérimentalement et calculé thermodynamiquement à son extrémité riche en magnésium. Plus de 20 alliages binaires et ternaires ont été synthétisés et traités thermiquement à température pièce et températures élevées. La microstructure et les paramètres de maille des échantillons ont été étudiés via XRD, SEM/EDS et EPMA pour déterminer les phases à l'équilibre. Le diagramme de phase ternaire a aussi été calculé à l'aide du logiciel de calcul thermodynamique Factsage. Les résultats provenant des expériences ainsi que de l'évaluation thermodynamique ont été comparés et discutés.

Les diagrammes de phase binaires ont été re-examinés, spécialement pour le système Mg-Ce. Dans le but d'évaluer l'étendue de composition des composés intermétalliques $Mg_{12}Ce$ et $Mg_{41}Ce_5$, ainsi que de clarifier les données des diagrammes de phase existants, les méthodes de couple de diffusion solide-liquide et de synthèse d'alliages aux phases ciblées ont été utilisés. Deux blocs de Mg et de Ce purs en contact étroit ont été encapsulés sous vide dans un tube de quartz à 400°C, laissant le Mg et Ce inter-diffuser. Les alliages préparés ont été coulés puis recuits à des températures variant entre 300 et 550°C. Toutes les zones à phase unique correspondant au diagramme de phase Mg-Ce ont été observées par la technique de couple de diffusion. Par contre, l'étude stoechiométrique du $Mg_{12}Ce$ par les alliages synthétisés et recuits a montré que, dans la partie riche en Mg du diagramme de phase, l'écart de composition du $Mg_{12}Ce$ devrait être redéfini par $Mg_{(11.17-10.81)}Ce$ à température ambiante et $Mg_{(11.31-10.75)}Ce$ à 530°C. Il a été confirmé que le composé $Mg_{41}Ce_5$ est bien un intermétallique stoechiométrique, mais avec une composition de 11.3at% Ce plutôt que de 10.9at% Ce.

L'étude du diagramme de phase binaire a été prolongée à l'extrémité riche en Ce du système Mg-Ce. Une nouvelle phase, $Mg_4Ce$, a été trouvée lors de l'étude de la phase $Mg_3Ce$. En se basant sur l'étude des composés intermétalliques du système binaire Mg-Ce, un diagramme de phase modifié a été suggéré pour accommoder la stoechiométrie de $Mg_{11}Ce$, $Mg_{39}Ce_5$, et $Mg_3Ce$.

L'étude expérimentale du diagramme de phase ternaire a été conduite sur trois isoplèthes: 0.6, 1.8 et 2.5wt% Mn, respectivement, et Ce a été varié entre 0 et 25wt%. Tous les alliages ont été produits à partir de matériaux initiaux de haute pureté. Deux types d'analyses thermiques, soit l'analyse des courbes de refroidissement et l'analyse calorimétrique différentielle (DSC), ont été utilisées pour déterminer le liquidus et la température de transformation en phase solide. Des tests de chauffe suivis de trempe sur certains échantillons sélectionnés ont été conduits pour analyse des phases. Les résultats ont démontrés qu'un seul *point invariant de réaction eutectique ternaire* est présent sur les trois isoplèthes, et que sa composition s'étend entre 1wt% Mn et 22wt% Ce à 592$^{o}$C. De plus, un intermétallique ternaire de type solution solide, $(Mg, Mn)_{11}Ce$, possédant la même structure tétragonale que le $Mg_{12}Ce$, est formé. La solution solide de Mn dans $Mg_{12}Ce$ varie entre 0.3~0.6 at%, dépendamment de la composition de l'alliage et des températures de trempe.

Finalement, les calculs de diagramme de phase provenant du logiciel FactSage ont été fait et de petites divergences entre les résultats modélisés et ceux expérimentaux ont été observées, spécialement pour la température eutectique de $L \rightarrow Mg(hcp) + Mg_{12}Ce$. Cela est principalement dû au fait que les résultats expérimentaux de cette présente étude n'étaient pas disponibles lorsque la modélisation thermodynamique a été performée. L'énergie de Gibbs de la phase $Mg_{12}Ce$ a été optimisée et les données révisées peuvent précisément reproduire les résultats expérimentaux à l'intérieur des limites d'erreurs expérimentales.

# ACKNOWLEDGEMENTS

I would like to express my deepest gratitude to Professor Mihriban O. Pekguleryuz, supervisor of this research, for her invaluable guidance, help and patience. I was strongly impressed not only by her solid knowledge of the physical metallurgy of light metals and her creativity in novel alloy development, but also her devotion to teaching and her students.

Special thanks go to Dr. Dmytro Kevorkov and Prof. In-Ho Jung, for many valuable discussions and for sharing their knowledge and expertise. I am also grateful to Pierre Vermette for his in-depth industrial experience and the safety training in experimental procedures, Helen Campbell and Lang Shi for their help in electron microanalysis, Monique Reindeau for the XRD analysis and Barbara Hanley for keeping us informed and updated of research information.

Many thanks go to Luke, Ana, Elvi, Yingling, Erol, Mert, and Mohsen, for the helpful discussions in our group meetings. This made my stay in the group pleasant. My appreciation also goes to my friends in the department, especially Lihong, Fazard, Dominique, Paula, Yaneth, Lydia, Mayeli, Romona, Elmira, Lan, Xinran, John, Naser, Max, Andreas, Cecile, and Faramarz. They made my life at McGill more than just a researcher. I will never forget the fun times in graduate baseball games, as well as the international potluck at the Thompson house.

There are also friends outside the department who deserve my sincere appreciation: Gu Jianglin, Guo Liping, Wang Yan, Cui Ying, Zhou Xiang, Zeng Qiaoling, Li Yuxiang, Qin Zhen, Sun Hong and Rick. The time we spent together was full of joy, surprise and amusement.

Finally, I owe special thanks to my parents and brothers. I always have strong support in every step in my career. The same for this work; it would not have been possible without their endless love and support.

# CONTRIBUTIONS OF AUTHORS

This thesis was prepared according to the guidelines for manuscript-based thesis. These guidelines are listed as Article C of the Thesis Preparation of McGill University. The information related to the authors of the manuscripts is cited as follows:

“In general, when co-authored papers are included in a thesis, the candidate must be the primary author (the author who has made the most substantial contribution) for all papers included in the thesis. In addition, the candidate is required to make an explicit statement in the thesis as to who contributed to such work and to what extent. This statement should appear in a single section entitled "Contributions of Authors" as a preface to the thesis. The supervisor must attest to the accuracy of this statement at the doctoral oral defence. Since the task of the examiners is made more difficult in these cases, it is in the candidate's interest to clearly specify the responsibilities of all the authors of the co-authored papers.”

The following manuscripts are used to prepare the thesis. The first four are incorporated in Chapter 4, which is 4.1, 4.2, 4.3 and 4.4, respectively. Manuscript 5 makes Chapter 5. The manuscripts have either been published, or accepted for publication, or submitted, as indicated.

1. X. Zhang, D. Kevorkov, M. Pekguleryuz, “Study of Phase Equilibria in Mg-Ce System via the Diffusion Couple Technique”, Magnesium Technology, A.Luo, N. Neelameggham, R. Beals, Eds., TMS, 2006, pp. 441-4.)

2. X. Zhang, D. Kevorkov, M. Pekguleryuz, "Stoichiometry Study on the Binary Compounds in the Mg-Ce System-Part I", J. Alloys Compounds, 475 (2009) 361-367

3. X. Zhang, D. Kevorkov, M. Pekguleryuz, "Study on the Binary Intermetallic Compounds in the Mg-Ce System", Intermetallics, 17 (2009) 496-503

4. X. Zhang, D. Kevorkov, M. Pekguleryuz, "Study on the Intermetallic Phases in the Mg-Ce System, Part II: Diffusion Couple Investigation", submitted to J. Alloys Compounds.

5. X. Zhang, D. Kevorkov, I-H. Jung, M. Pekguleryuz, "Phase Equilibria on the Ternary Mg-Mn-Ce System at Mg-Rich Corner", J. Alloys Compounds, 482 (2009) 420-428

All the manuscripts are co-authored by Prof. M. O. Pekguleryuz, who is the project research supervisor. All the experiments were conducted by the candidate. All the manuscripts include Dr. Dmytro Kevorkov (Research Associate, Department of Mechanical Engineering, Concordia University) for his contribution in understanding the crystal structure of the intermetallic compounds, as well as his guidance in experimental determination of ternary phase diagrams. Manuscript 5 includes Prof. In-Ho Jung (Department of Mining and Materials Engineering, McGill University) for his contribution in thermodynamic evaluation of ternary phase diagrams. All the work presented in this thesis apart from the co-author contributions mentioned above, was performed by the candidate.

# TABLE OF CONTENTS

# LIST OF FIGURES

# LIST OF TABLES

# CHAPTER 1

# INTRODUCTION

Mn was first introduced to the Mg-Al alloys due to its capability of lowering the iron content, so that the corrosion resistance of the alloys can be increased. Mg alloys containing Mn also present good ductility, making it possible to form sheet, extrusion and tube alloys. The shortcoming of manganese is that it displays little effect on the tensile properties of either cast or wrought Mg alloys. Cerium mischmetal, on the contrary, has been known to improve the elevated temperature properties of Mg alloys. Therefore, magnesium containing both Mn and Ce is great potential in developing magnesium wrought alloys.

Phase diagrams are the basis of the activities related to the development of new alloys, improvement of the alloy mechanical properties and process design. Experimental study of an unknown alloy system can obtain not only the conventional thermal information such as the liquidus temperature and enthalpy of phase transition, but also the formation of intermetallic compound, as well as the solid solution range of either terminal elements or intermetallic compounds. The computation of the experimental data using thermodynamic software will then generate the phase diagram.

In experimental phase diagram study, diffusion couple is a fundamental and valuable technique. Phases formed between two or more terminal materials are the result from diffusion at a given temperature. Assuming sufficient diffusion time, the process is infinitely close to equilibrium. From the diffusion couple, a brief phase diagram could be built at the initial stage. Thermal analysis (CCA and DTA/DSC) is often used for phase diagram study because any phase transformation is related to heat evolution. Thus these thermal behaviours could be recorded as thermal arrest in the cooling curve and transformation temperature/enthalpy in DTA/DSC. Besides these, XRD, SEM and TEM are the valuable tools to study the microstructure and identify the unknown phases.

In present work, the Mg-Mn-Ce phase diagram in the Mg-rich region has been constructed. To do this, each of the binary systems was investigated, and some uncertain information on the binary intermetallic compounds were re-evaluated using the techniques mentioned above. Ternary compositions up to 10 wt% Mn and 30 wt% Ce were prepared for thermal analyses and microstructure observation. Meanwhile, the identification of the ternary intermetallic compound, as well as the determination of the ternary phase boundary were also conducted. The calculation of the ternary phase diagram is based on the thermodynamic modeling of the experimental data via FACTSage program.

This work includes literature survey of the study on the binary and ternary equilibria of the Mg-Mn-Ce system in Chapter 2, followed by a review of the research methodology and experimental techniques in Chapter 3. The detailed phase diagram investigation of the binary systems is presented in Chapter 4. The ternary phase diagram study at Mg-rich corner is in Chapter 5. The conclusions as well as the contribution to original knowledge are stated in Chapter 6 and 7, respectively.

# CHAPTER 2

# LITERATURE REVIEW

## 2.1 Binary Phase Diagrams

### 2.1.1 Mg-Ce System

The recent version of the Mg-Ce phase diagram is shown in Fig. 2.1a [1], and six intermetallic compounds were reported, i.e. $Mg_{12}Ce$, $Mg_{41}Ce_5$, $Mg_3Ce$, MgCe, $Mg_{10.3}Ce$ and $Mg_2Ce$. All are formed from the liquid by peritectic reactions except for $Mg_3Ce$ that melts congruently.

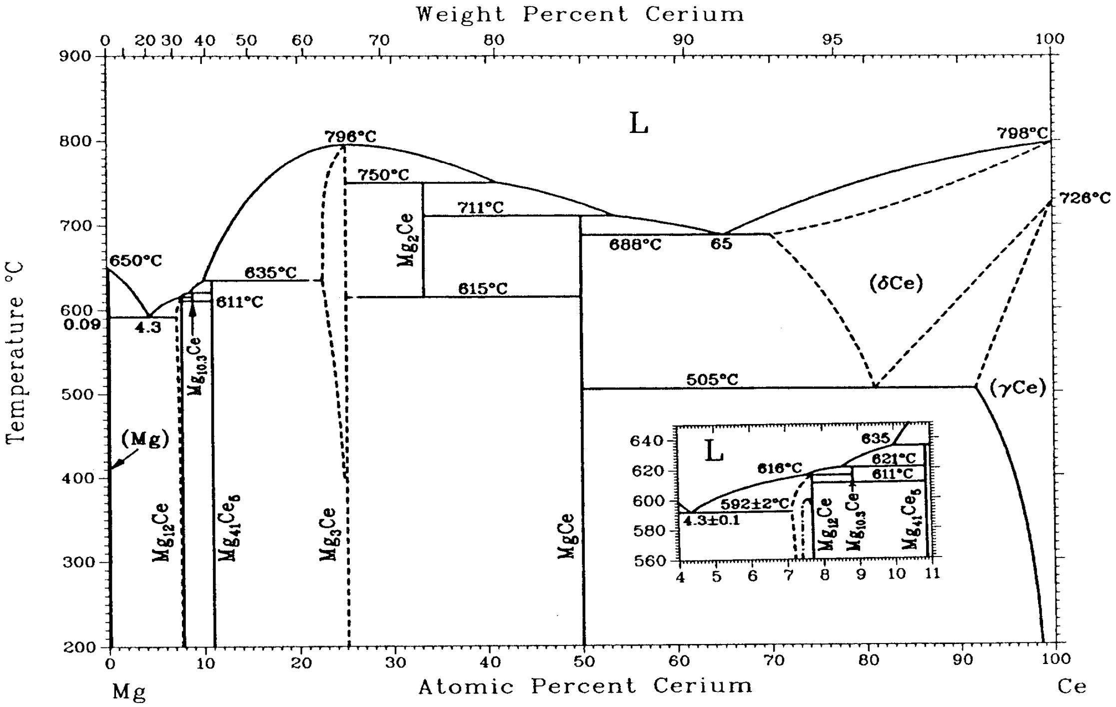

*Fig. 2.1 (a) Assessed [1] Mg-Ce phase diagram*

In the earliest study of this system by Vogel [2], $Mg_9Ce$ was postulated due to the similarity between magnesium-cerium and the magnesium-lanthanum diagram. However, the work from Wood and Cramer [3] by conventional methods of DTA, XRD and metallography showed that instead of $Mg_9Ce$, three compounds formed peritectically ($Mg_{12}Ce$, $Mg_{17}Ce_2$, $Mg_{8.25}Ce$) in this composition region. $Mg_{17}Ce_2$ compound has been repeatedly studied, and the formula $Mg_{10.3}Ce$ was also suggested due to the enriched Mg in lattice parameter analyses. No study has been conducted yet for the solid solution range of the compounds $Mg_{12}Ce$ and $Mg_3Ce$ that are marked by dotted lines on the phase diagram. The solid solution of Ce in Mg is low (0.09 at% Ce) compared to the significant solid solubility of Mg in δ-Ce. However, the solubility range was not determined.

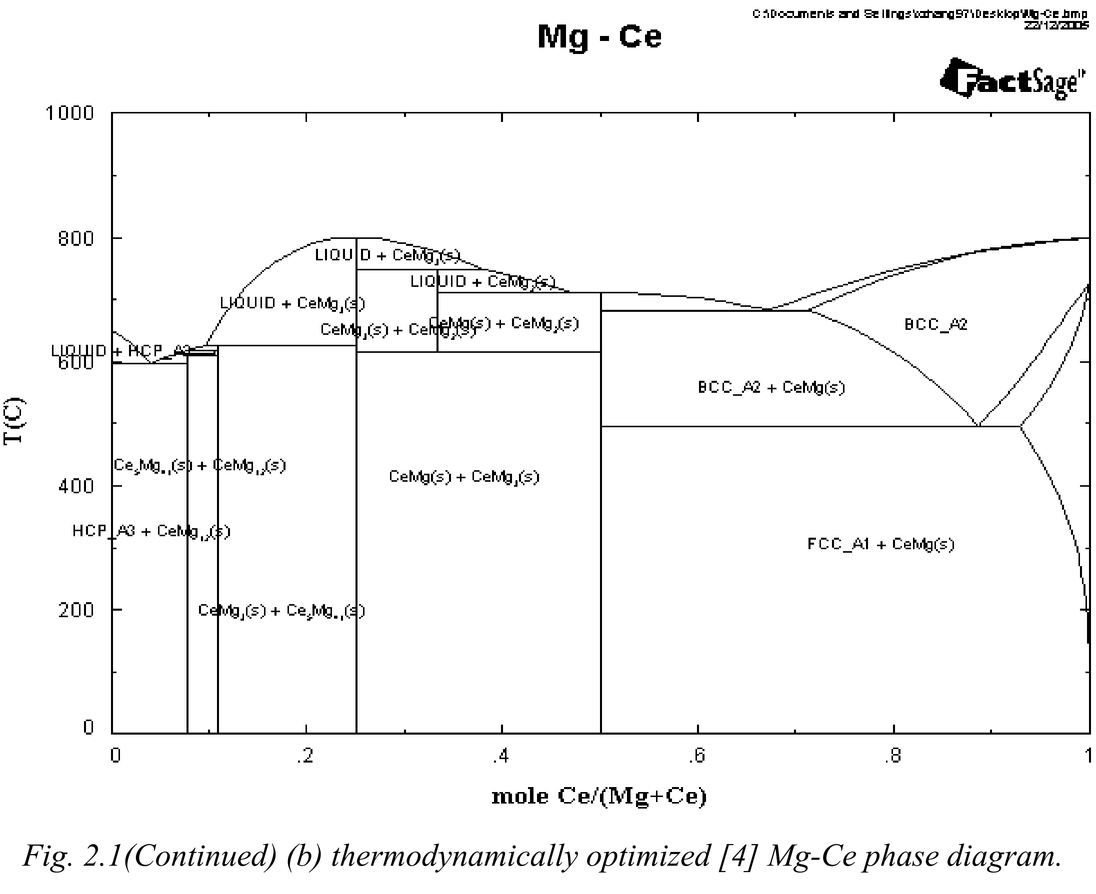

*Fig. 2.1(Continued) (b) thermodynamically optimized [4] Mg-Ce phase diagram.*

This system is also thermodynamically optimized using FACTSage [4] and the phase diagram has been reproduced reasonably well, except the solubility of Ce in Mg and the solubility range for $Mg_{12}Ce$ and MgCe (Fig. 2.1b). There is no published report investigating the solid solution range of these two compounds, therefore, no data could be input for optimization.

### 2.1.2 Mg-Mn System

Only a small portion (0-3.0 at% Mn) of the Mg-Mn system has been studied based on the thermal analyses, microscopic observation, and hardness tests of Petrov and co-workers [5], and the electrical resistivity measurement of Drits and co-workers [6]. There exists a peritectic reaction at 653°C at the composition of 0.996 at% Mn (Fig. 2.2a), and the solid solubility of manganese in HCP magnesium is low. No intermediate compounds were reported.

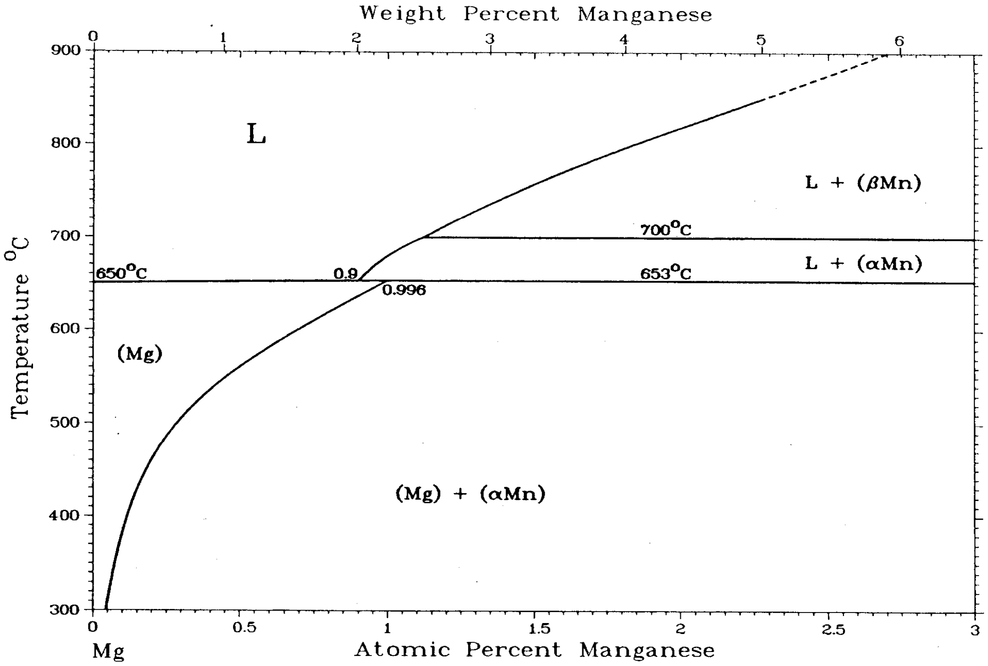

*Fig. 2.2 (a) Assessed [1] Mg-Mn phase diagram.*

FACTSage extrapolated the complete phase diagram based on the information from the Mg side (Fig. 2.2b). Only a monotectic reaction on Mn side could be produced and needs to be experimentally validated.

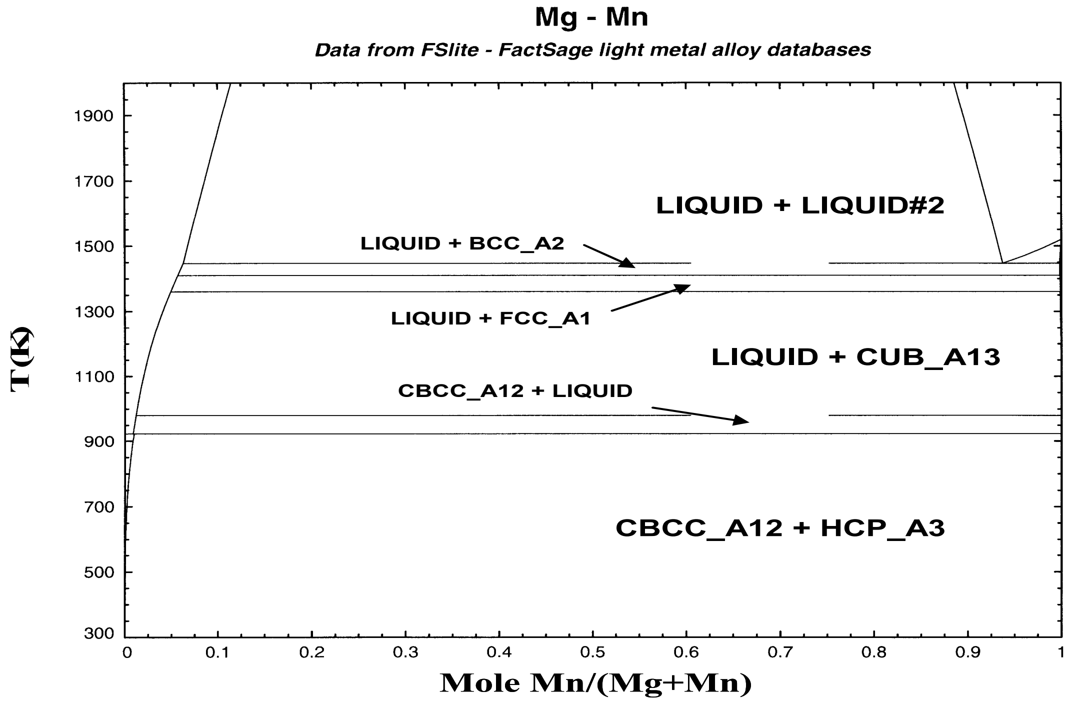

*Fig. 2.2(Continued) (b) thermodynamically optimized [4] Mg-Mn phase diagram.*

### 2.1.3 Ce-Mn system

The complete range of Ce-Mn system was studied initially by Iandelli [7] using thermal analysis and is given in Fig. 2.3. No intermediate compounds were found and no further investigation was conducted of the terminal solubilities. Then the study by Mirgalovskaya and Strel'nikova [8] agreed substantially with Iandelli except the allotropic temperature related to the allotropic transition of manganese. Later on, Thamer [9] investigated the cerium-rich part by DTA and XRD, and stated that the solubility of Mn is 5 at% in δ-Ce and 2 at% in γ-Ce at 638°C. No experimental data are available on the Mn side, but Iandelli [7] concluded non-solubility of Ce in α-Mn at room temperature with an unchanged lattice parameter of α-Mn in an alloy of 30wt% Mn.

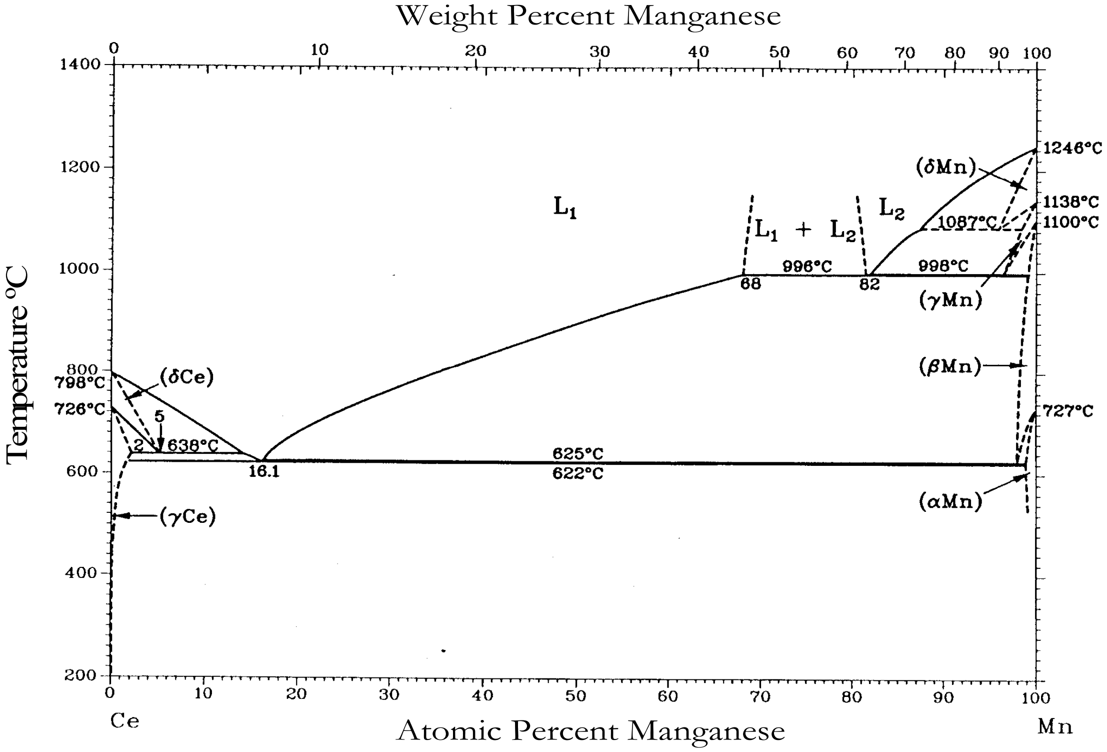

*Fig. 2.3 Assessed Ce-Mn phase diagram [1].*

## 2.2 Mg-Mn-Ce Ternary Phase Diagram

### 2.2.1 The Construction of the Ternary Mg-Mn-Ce Phase Diagram

Although cerium and manganese have been used as alloying elements in steel or light metal based alloys, little information on the ternary Mg-Mn-Ce system has been published. Emley [10] studied the ternary isopleths of the Mg-Mn-Ce system with maximum 3 wt% Mn and Ce at 0.3 and 1.6 wt% respectively (Fig. 2.4). In this section, no ternary compound formed, and the binary compound $Mg_9Ce$ is incorrect due to the limited study.

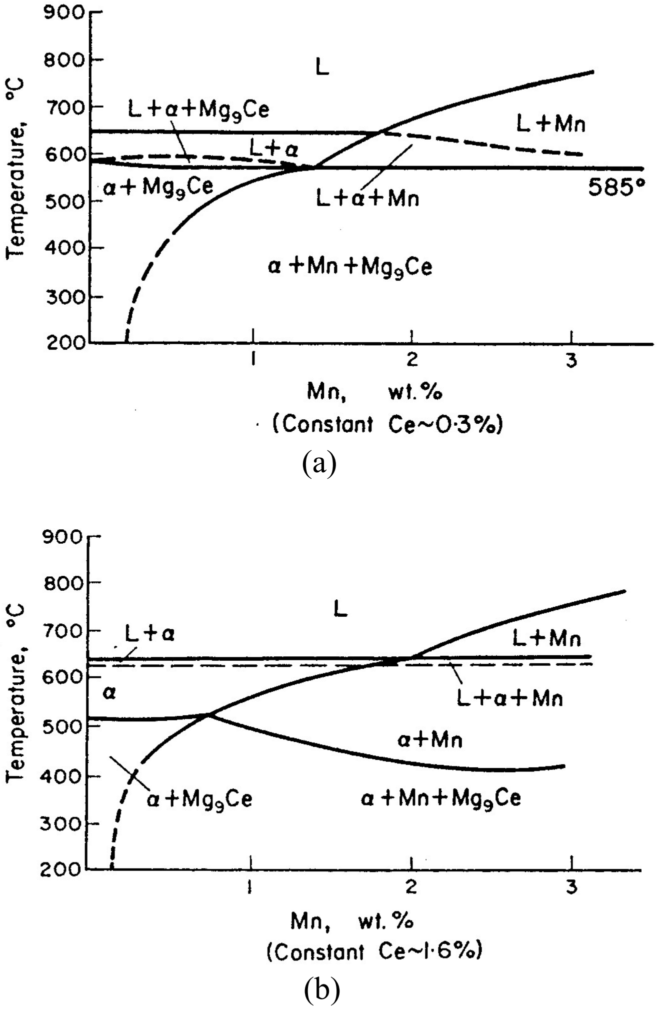

*Fig. 2.4 Polythermal sections of Mg-Mn-Ce system [10], at (a) Ce ~0.3wt%, and (b) Ce ~1.6wt%*

On the other hand, the $Mg_{11}MnCe$ ternary compound was reported in the study of Ce-Mg-M systems (M= V, Cr, Mn, Fe, and Co) and the author proposed to use this compound for hydrogen storage [11]. Pearson's handbook [12] thus compiled this ternary compound $Mg_{11}MnCe$ with the lattice parameters measured by the author. Close examination of this paper reveals that $Mg_{11}MnCe$ is only a chemical formula. The author must have intended to substitute 1 mol Mn for 1mol magnesium and measure the hydrogen capacity when chemical reaction occurred. There are some hydrogen variations in different M, but the alloys are still a mixture of $Mg_{11}Ce$ and the transition metals. $Mg_{12}Ce$ is reported as $Mg_{11}Ce$ for no apparent reason and may have been a mistake. Therefore, the lattice parameters are not representative as this ternary compound and the existence of a ternary compound should be reexamined.

### 2.2.2 Thermodynamic Modeling of the Ternary Mg-Mn-Ce Phase Diagram

The advantage of thermodynamic modeling in constructing ternary, quaternary, and higher order phase diagrams is that modeling can predict the liquid surface and eutectic points, and reduce the number of experiments. The disadvantage is that it cannot calculate new phases if they are not discovered via experiments. However, if appropriate thermodynamic models together with some key experiments are combined firstly to optimize the binary systems, the binary data can therefore be extrapolated into ternary and higher order systems [13].

FactSage is one of the largest database computing systems to calculate multicomponent and multiphase equilibria. It is the combination of two programs: ChemSage (GTT Technologies) and FACT-Win (Thermfact), and becomes a reliable tool for thermodynamic assessment. So far two binary systems, Mg-Ce and Mg-Mn, have been optimized by the FactSage program, but for the Ce-Mn system, the experimental data is limited, and has not been optimized. Although researchers have increased knowledge by modeling the Mg-Mn-(Sr, Gd, Y, Zr) [14] or Al-Ce-Mg [15] system based on the well-established binary ones, no Mg-Mn-Ce ternary system optimization has been reported.

### 2.3 Metal Purity in Phase Diagram Studies

The construction of phase diagram requires the use of pure elements, and although these do not exist, the higher purity, the more accurate the phase diagram. As even a small quantity of impurities may have the great effect on the mechanical properties of metals and alloys, the purity has to be strictly controlled. The same principle applies to the starting materials used for phase diagram study in that the purity strongly influences the make up of phase diagrams.

Taking a Mg-Ce phase diagram development as an example, when the cerium employed contained 6.5% of impurity, the eutectic composition and temperature reported were 27 wt% Ce at 585$^o$C [16]. When the cerium was 97.7% purity, the measurement changed to 21wt% cerium at 590$^o$C [17], which is very close to the present publication of 20.6 wt% Ce at 592±2$^o$C [3]. It should be noted that there are interstitial impurities such as H, O, N, and C, which may increase or decrease the melting points of rare earth metals, but they are seldom quantified [18].

Gschneidner, Jr. [19] reviewed the effect of interstitial impurities on some of the properties of the pure rare earth metals by comparing the low temperature heat capacity of purified Gd to Gd containing oxygen around 2 at%. It was concluded that heat capacity peaks are due to the oxygen behaviour and non-equilibrium structure of the metals is stabilized by interstitial impurities. *i.e.,* some structures which are now known not existing in high purity rare earth metals are due to the reaction with O, N, and H during the experimental process (mechanical milling). Therefore, a purification process, named zone refining and solid state electrotransport (SSE) were designed and assessed on some rare earth metals [20,21].

In zone refining, the impurities that lower the metal's melting point are carried to the end of the rod sample, whereas the impurities that increase the melting point migrate towards the beginning of the sample when a hot zone is passed repeatedly in one direction. In SSE a rod sample is connected to a direct electrical current but not melt the sample. In rare earth metals, the interstitial impurities migrate faster than the metal, and condense towards one electrode. Fig. 2.5 shows the evolution of these processes of Gd. The rod sample of Gd was first subjected to zone refining. The two ends were removed and the rest of the rod was remelted and subject to two times SSE.

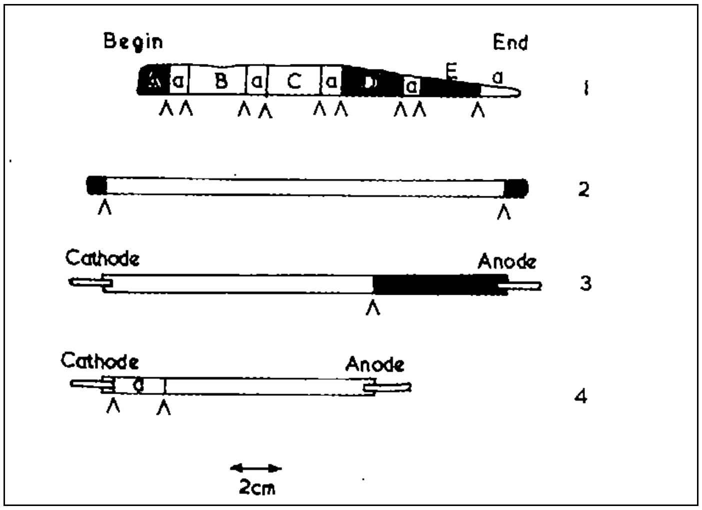

*Fig. 2.5 Schematic diagrams showing the size and shape of the sample (Gd): (1) after zone refining, (2) after remelting parts B and C and swaging, (3) after the first stage of SSE, and (4) after the second stage of SSE. The sample was cut at the position marked ^ [20].*

The chemistry of the purified part shows in Table 2.1. This sample contains 2441 atomic ppm O, H, N, C interstitial impurity out of the total 2481 at. ppm (the rest is 40 atomic ppm Zr, Ni, Fe, Al metallic impurity) before the two processes. However, it reduced to 1236 at. ppm after zone refining (average value of begin, ¼ and ½ of the total length) and further to 579 atomic ppm after SSE at the cathode end. Although neither of these two methods can remove the impurities from the sample, zone refining has been found efficient in redistributing metallic impurities, and SSE is good to transport interstitial impurities.

Table 2.1 Analysis of start metal, Gd, at five positions after zone refining and at the cathode after SSE [20]

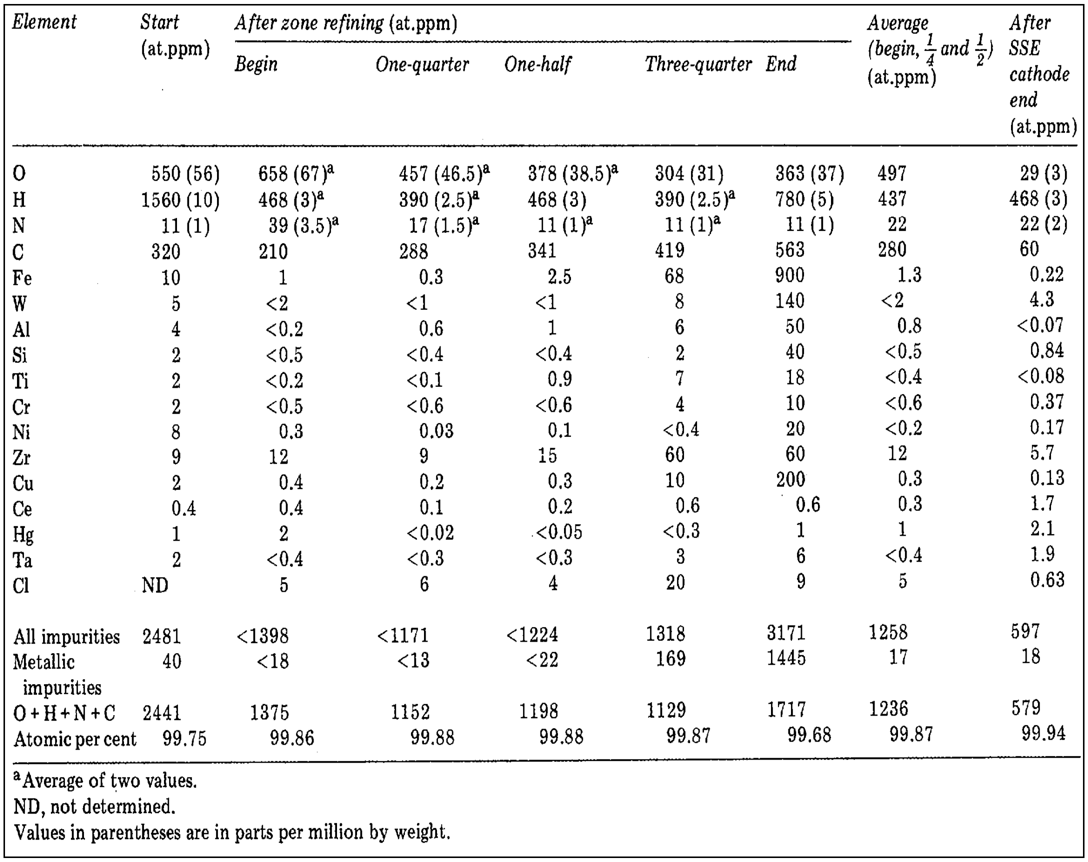

| *Element* | *Start* (at.ppm) | *After zone refining* (at.ppm) | | | | | *Average* (*begin*, $\frac{1}{4}$ *and* $\frac{1}{2}$) (at.ppm) | *After SSE cathode end* (at.ppm) |
|---|---|---|---|---|---|---|---|---|
| | | *Begin* | *One-quarter* | *One-half* | *Three-quarter* | *End* | | |
| O | 550 (56) | 658 (67)[a] | 457 (46.5)[a] | 378 (38.5)[a] | 304 (31) | 363 (37) | 497 | 29 (3) |
| H | 1560 (10) | 468 (3)[a] | 390 (2.5)[a] | 468 (3) | 390 (2.5)[a] | 780 (5) | 437 | 468 (3) |
| N | 11 (1) | 39 (3.5)[a] | 17 (1.5)[a] | 11 (1)[a] | 11 (1)[a] | 11 (1) | 22 | 22 (2) |
| C | 320 | 210 | 288 | 341 | 419 | 563 | 280 | 60 |
| Fe | 10 | 1 | 0.3 | 2.5 | 68 | 900 | 1.3 | 0.22 |
| W | 5 | <2 | <1 | <1 | 8 | 140 | <2 | 4.3 |
| Al | 4 | <0.2 | 0.6 | 1 | 6 | 50 | 0.8 | <0.07 |
| Si | 2 | <0.5 | <0.4 | <0.4 | 2 | 40 | <0.5 | 0.84 |
| Ti | 2 | <0.2 | <0.1 | 0.9 | 7 | 18 | <0.4 | <0.08 |
| Cr | 2 | <0.5 | <0.6 | <0.6 | 4 | 10 | <0.6 | 0.37 |
| Ni | 8 | 0.3 | 0.03 | 0.1 | <0.4 | 20 | <0.2 | 0.17 |
| Zr | 9 | 12 | 9 | 15 | 60 | 60 | 12 | 5.7 |
| Cu | 2 | 0.4 | 0.2 | 0.3 | 10 | 200 | 0.3 | 0.13 |
| Ce | 0.4 | 0.4 | 0.1 | 0.2 | 0.6 | 0.6 | 0.3 | 1.7 |
| Hg | 1 | 2 | <0.02 | <0.05 | <0.3 | 1 | 1 | 2.1 |
| Ta | 2 | <0.4 | <0.3 | <0.3 | 3 | 6 | <0.4 | 1.9 |
| Cl | ND | 5 | 6 | 4 | 20 | 9 | 5 | 0.63 |
| All impurities | 2481 | <1398 | <1171 | <1224 | 1318 | 3171 | 1258 | 597 |
| Metallic impurities | 40 | <18 | <13 | <22 | 169 | 1445 | 17 | 18 |
| O + H + N + C | 2441 | 1375 | 1152 | 1198 | 1129 | 1717 | 1236 | 579 |
| Atomic per cent | 99.75 | 99.86 | 99.88 | 99.88 | 99.87 | 99.68 | 99.87 | 99.94 |

[a] Average of two values.

ND, not determined.

Values in parentheses are in parts per million by weight.

## 2.4 References

1. T. B. Massalski, editor-in-chief, Binary Alloy Phase Diagrams, Materials Park, Ohio: ASM International, 1990.
2. R. Vogel, Z. anorg. Chem. Vol.91, p.277, 1915
3. D. H. Wood and E. M. Cramer, Phase Relations in the Magnesium-rich Portion of the Cerium-Magnesium System, Journal of the Less-Common Metals, Vol. 9, p.p. 321-337, 1965.
4. FACTSage Thermochemical Software and Databases, Ecole Polytechnique, 2005
5. D. A. Petrov, M. S. Mirgalovskaya, I. A. Strelnikova, and E. M. Komova, Trans. Inst. Met. A. A. Baikova, Akad. Nauk SSSR, Vol.1, p.142-143, 1957, (in Russian).
6. M. E. Drits, Z. A. Sviderskaya, and L. L. Rokhlin, Izv. Nauka, Moscow, p.p. 272-278, 1964, (in Russian).
7. A. Iandelli, The Ce-Mn Alloys, Atti. Accad. Naz. Lincei. Rend., Vol. 13, p.p. 265-268, 1952.
8. M. S. Mirgalovskaya and I. A. Strel'nikova, Investigation in the Mn-Ce System, Trudy Inst. Met. Im A. A. Baikova, Akad. Nauk SSSR, p.p. 135-138, 1957.
9. B. J. Thamer, The System Ce-Mn in the Range of 0-20 Atomic Percent Manganese, Journal of the Less-Common Metals, Vol.7, p.341-346, 1964.
10. E. F. Emley, Principles of Magnesium Technology, Pergamon press Ltd., London, 1966.
11. M. Pezat, A. Hbika and B. Darriet, Study on Alloys of CeMgM Composition (M=V, Cr, Mn, Fe, Co) and Their Use in Hydrogen Storage, Materials Research Bulletin, Vol. 15, p.p. 139-146, 1980.
12. P. Villars and L.D. Calvert, Pearson's Handbook of Crystallographic Data for Intermetallic Phases, 2nd ed., Materials Park, OH: ASM International, 1991.

13. M. Hotch, Calculation of Ternary, Quaternary, and Higher-Order Phase Diagrams from Binary Diagrams and Binary Thermodynamic Data, Journal of Phase Equilibria, 14 (6), p.p. 710-717, 1993.
14. J. Grobner, and R. Schmid-Fetzer, Selection of Promising Quaternary Candidates from Mg-Mn-(Sr, Gd,Y, Zr) for Development of Creep-resistant Magnesium Alloys, Journal of Alloys and Compounds, Vol.320, p.296-301, 2001.
15. J. Grobner, D. Kevorkov, and R. Schmid-Fitzer, Thermodynamic Modeling of Al-Ce-Mg Phase Equilibria Coupled with Key Experiments, Intermetallics, Vol. 10, p.p. 415-422, 2002.
16. G.V. Raynor, The Physical Metallurgy of Magnesium and its Alloys, Pergamon press Ltd., p. 371, 1959
17. J. L. Haughton, and T. H. Schofield, Alloys of Magnesium, Part V: The Constitution of The Magnesium-rich Alloys of Magnesium and Cerium, Journal of the Institute of the Metals, vol. 60, p.339, 1937
18. K. A. Gschneidner, Jr. and B. J. Beaudry, Comments on The Paper "DTA Determination of The Temperature and Enthalpy Changes of The $\alpha \rightarrow \beta$ and Solid $\rightarrow$Liquid Phase Transitions of Pure Neodymium, Scripta Metalurgica et Materialia, vol. 25, p. 745-748, 1991
19. K. A. Gschneidner, Jr., Metals, Alloys and Compounds-High Purities Do Make A Difference! Journal of Alloys and Compounds, 193 (1993) 1-6
20. D. Fort, B. J. Beaudry and K. A. Gschneidner, Jr., The Ultrapurification of Rare Earth Metals: Gadolinium and Neodymium, Journal of The Less-Common Metals, 134 (1987) 27-44
21. D. Fort, The Purification and Crystal Growth of Rare Earth Metals Using Solid State Electrotransport, Journal of The Less-Common Metals, 134 (1987) 45-65

# CHAPTER 3

## REVIEW ON EXPERIMENTAL METHODS OF PHASE DIAGRAM STUDY

The construction of phase diagram is a complex process that various experimental techniques are employed. The result of one method needs to be re-examined by several other techniques to obtain an accurate and reliable phase diagram. This section reviews the techniques that are conventionally used in phase diagram studies. Only the main techniques for phase diagram construction are reviewed. Each technique has its own advantages and limitations. The reliable and accurate results are obtained by a combination of these methods.

### 3.1 Diffusion Couple Technique

Diffusion couple is a frequently used technique to study phase diagrams. Two or more metals are mechanically or thermally coupled to have intimate contact, and subject to heat treatment at elevated temperature. The irreversible, spontaneous, and thermally activated atomic migration starts. The diffusion zone forms after a long heat treatment, and ideally all the phases become visible after diffusion. The coupled materials are not limited to pure metals, metal-alloy, or alloy-alloy couples are often seen. The relation between the diffusion couple and the phase diagram is that the sequence of the layers in the diffusion zone conforms to the intermediate phases in the phase diagram. The diffusion zone only consists of single-phase layers in a binary system, and both single and two-phase layers in a ternary system, when local equilibrium is reached.

As an example, in the study of the diffusion mechanism and formation of intermetallic compounds in the Mg-Cu system, the diffusion couple made of pure Mg and Cu was used [1]. Two intermetallic compounds $Mg_2Cu$ and $MgCu_2$ were revealed after diffusion anneals at 475°C for 370.8ks.

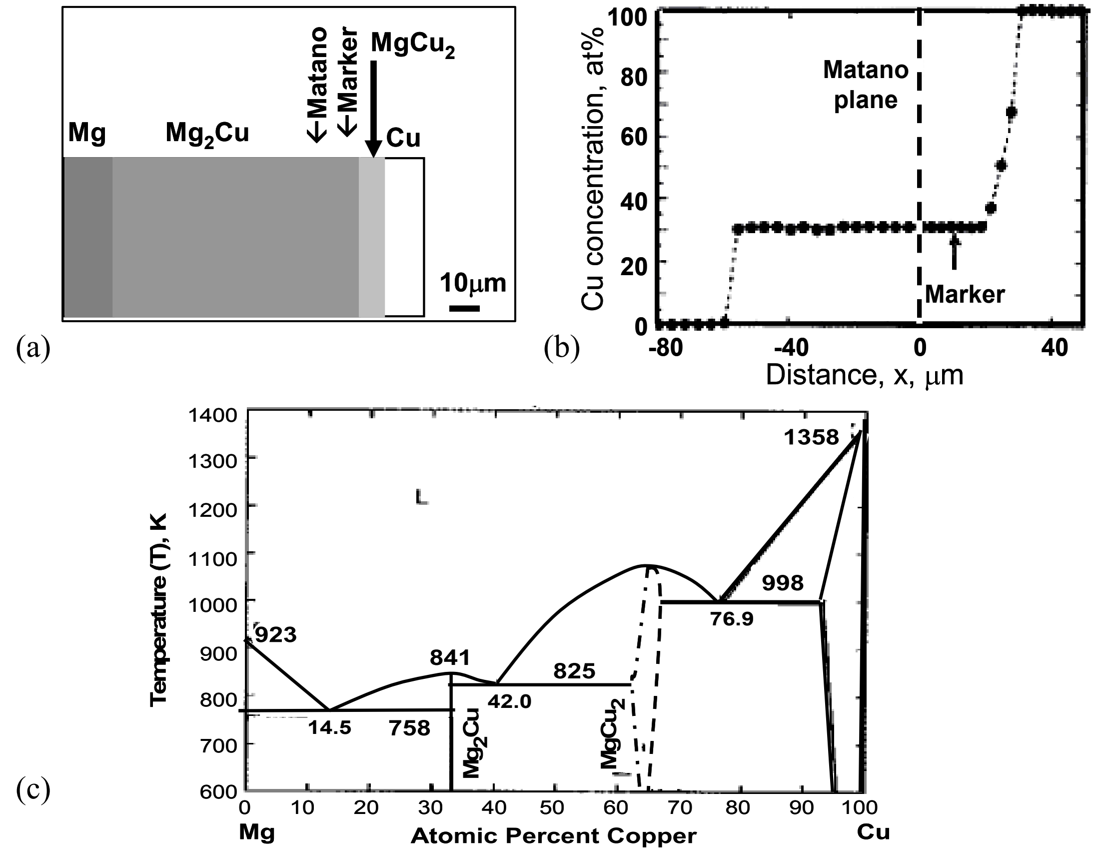

*Fig. 3.1 (a) Illustration micrograph of Mg-Cu diffusion couple annealed at 475°C for 370.8ks, (b) Concentration profile of the diffusion couple, (c) the Mg-Cu phase diagram showing the line compound $Mg_2Cu$ and the possible non-stoichiometric compound $MgCu_2$ [1].*

Fig. 3.1a and b show the SEM micrograph of the diffusion layers and the concentration profile across the diffusion zone measured by EPMA. The EPMA profile indicates $Mg_2Cu$ a line compound with the constant horizontal line. This agrees with the Mg-Cu phase diagram (Fig. 3.1c). However, the interdiffusivity of $MgCu_2$ was unable to be evaluated because the thickness of this layer is too small, the concentration range showing off-stoichiometry may be due to the limited resolution of microprobe analysis. This might be resolved for the sample annealed at higher temperatures for longer times.

There are two ways to make diffusion couples: solid-solid and solid-liquid. Solid-solid coupling applies to two elements having similar melting point, but the limitation is that the subsequent solid state diffusion is relatively slow and the appearance of all equilibria phases is not always guaranteed due to the diffusion coefficient of the atoms in various intermediate phases. Solid-liquid coupling is adopted by dissimilar metals, for example, metals that have large difference in melting point. In this case, the contact is good and the diffusion is faster by involving one element in liquid phase. However, the following annealing in solid state is necessary to reach local equilibrium of the diffusion layers. Diffusion couples have been employed in a number of studies to determine phases in alloy systems.

1. Solid solubility [2-4]

The solid solubility study using diffusion couples is usually combined with EPMA. Fig. 3.2a is the study on the solid solubility of Zr in Mg conducted by Poole et al [2] at a temperature range of 596-639$^{o}$C. Two layers formed between Mg and Zr: the solid solution of Zr in Mg and the columnar zone can be seen (Fig. 3.2a). X-ray pattern could not identify the columnar zone as the metals, their oxides, or $MgZr_2$, however, this phase contains ~10 wt% zirconium from microprobe analysis. Fig. 3.2b gives the concentration profile of Zr and Mg, the total weight percent sum well to 100% showing the correct analytical procedure. The solid solubility of Zr in Mg was calculated to be ~ 4 wt% Zr from the microprobe analysis (Fig. 3.2c). However, a more precise definition could not be made due to the excessive surface defects.

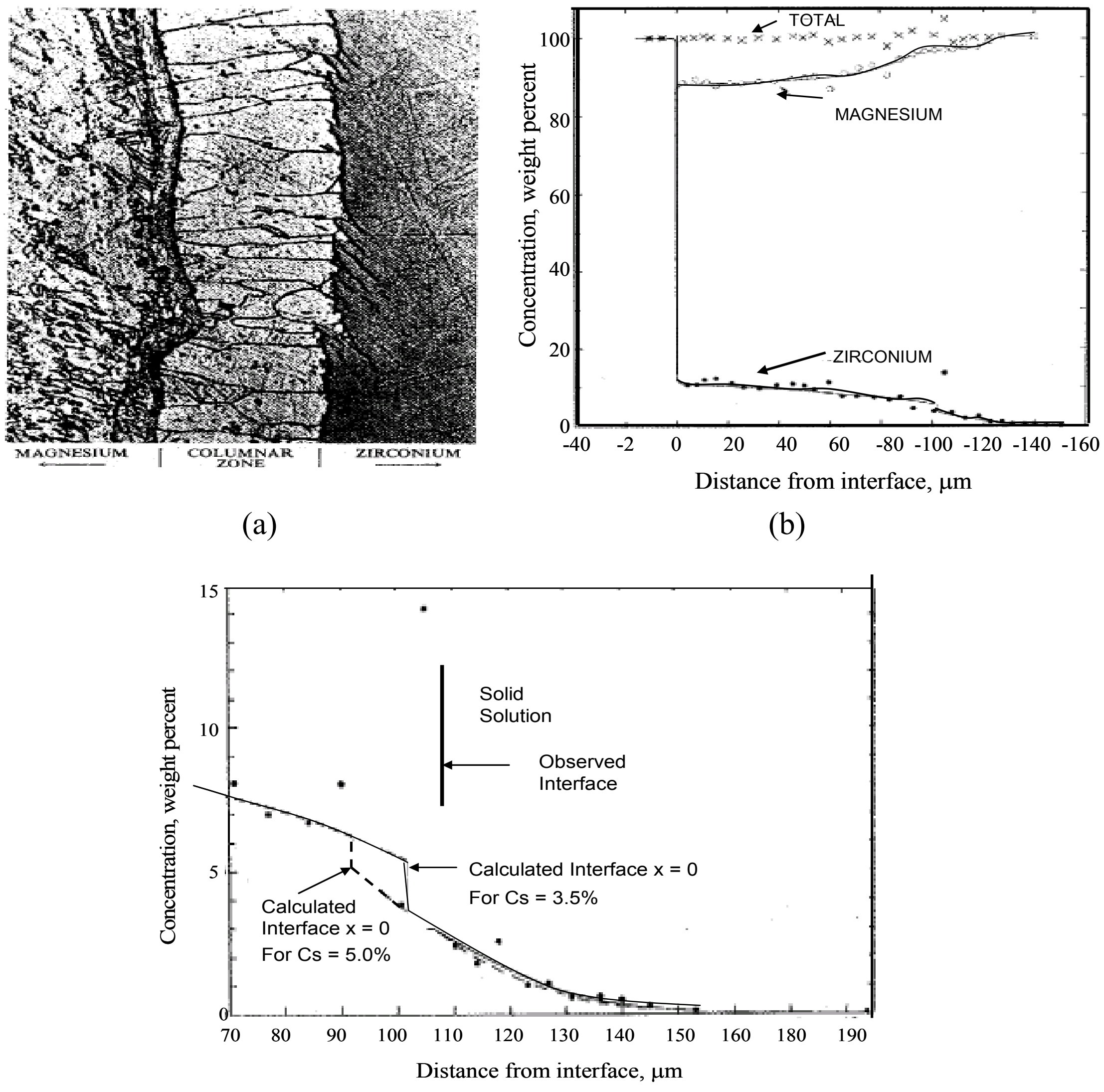

(a) (b)

(c)

*Fig. 3.2(a) Diffusion couple showing the columnar zone, (b) Concentration of zirconium and magnesium across diffusion zone determined by microprobe analysis at 623$^{o}$C. The sum up of weight percentage to 100% confirmed the correction of the results, and (c) Detail of concentration of zirconium in magnesium at 623$^{o}$C [2].*

2. Equilibrium phase identification at different temperatures [5-11]

Diffusion couples are also very useful in characterizing intermetallic compounds and their phase boundaries. The diffusion couple made of a pure metal and a binary eutectic alloy was employed to study the number of binary and ternary intermetallic compounds, and the association between the compounds [5]. Diffusion couples can also be used to study the phase stability and the interdiffusivity at different temperatures [7,8]. For example, Kainuma et al [8] used a diffusion couple of (Ti-55Al)/(Ti-75Al) and annealed at 900-1350°C to study the phase stability and interdiffusivity of γ-TiAl, $Ti_5Al_{11}$, and $TiAl_2$ (Fig. 3.3a). $TiAl_2$ was found having the congruent temperature at 1216°C, and the structure of $Ti_5Al_{11}$ was established as a higher order structure of γ-TiAl (Fig. 3.3c) if compared with the Ti-Al phase diagram (Fig. 3.3b). The critical phase boundary of TiAl/$Ti_5Al_{11}$ was also defined at around 64.5 at% Al at temperature range of 1250-1350°C.

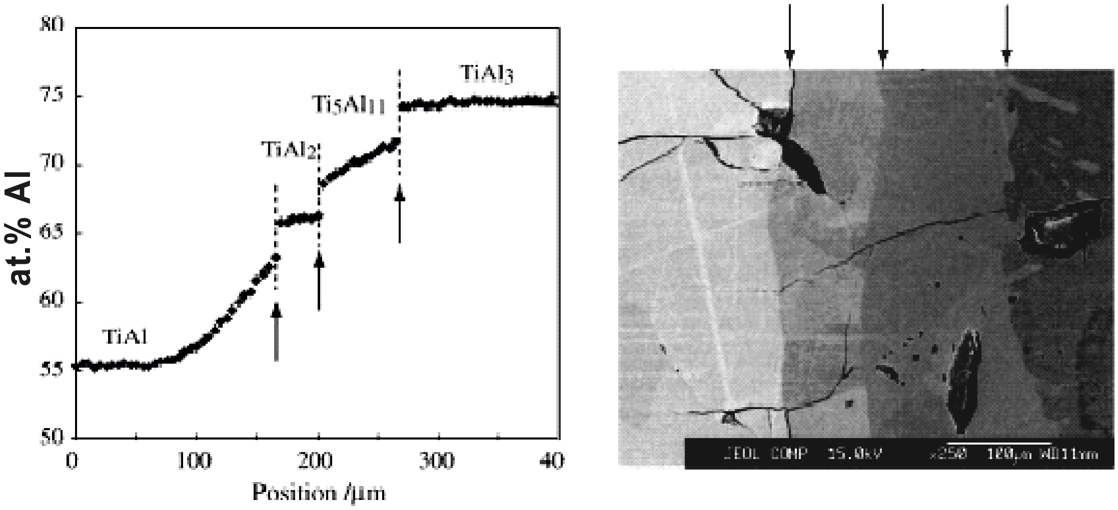

(a)

*Fig. 3.3 (a) Diffusion couple of (Ti-55Al)/(Ti-75Al) and the diffusion zone formed at 1200°C.*

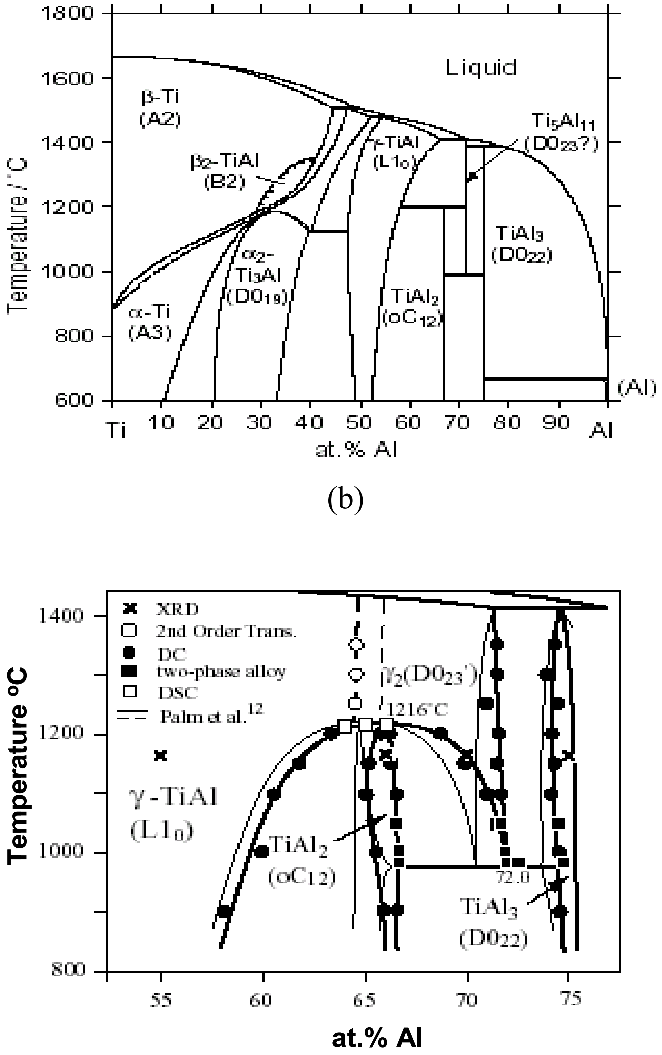

(b)

(c)

*Fig. 3.3 (Continued) (b) the phase diagram of the Ti-Al binary system and (c) The experimental phase diagram plotted in the Al-rich portion [8].*

Diffusion couples are also important in studying coating behavior [12] to identify compounds forming between coating substrate, so that the coating material for best anti-oxidation can be selected. Diffusion couples are most often used for diffusion coefficient study in either pure metal or intermetallic compounds [13].

### 3.2 Thermal Analysis

Thermal analysis is a technique widely used to investigate the thermal behaviour of a system as a function of temperature. As the phase transition always accompanies by the heat evolution, the related temperature can be recorded through the cooling curve or thermal analysis (DTA and DSC), and the enthalpy of the phase transition can be calculated.

### 3.2.1 Cooling Curve Analysis (CCA)

The cooling curve is the instantaneous record of temperature vs. time using thermocouple in direct contact with the melt during solidification. Cooling curves are used to determine phase transitions because any phase change is related to heat evolution, no matter it is physical such as fusion and solidification, or chemical such as reactions. The slope of the cooling curve represents the cooling rate; that means the related phase change can speed up or slow down the solidification process.

In phase diagram studies, the shape of cooling curves varies with phase compositions. For example, in a binary system, when a melt is cooled to the liquidus at two different compositions, E & H, as shown in Fig. 3.4a, the thermal arrest produced in E is the solidification at the eutectic composition [14]. The thermal arrest is horizontal because this is an equilibrium freezing point. The temperature will maintain by the latent heat until the crystallization is complete, then normal cooling is resumed. At composition H, the solidification firstly involves the precipitation of one constitutional element, $\beta$, and then the cooling turns slow due to the heat generated during solidification. When the crystallization reaches the eutectic temperature, the cooling is hampered as what happens at composition E. The crystallization is recorded by the steps on the cooling curve at hypereutectic point compared to the eutectic point E.

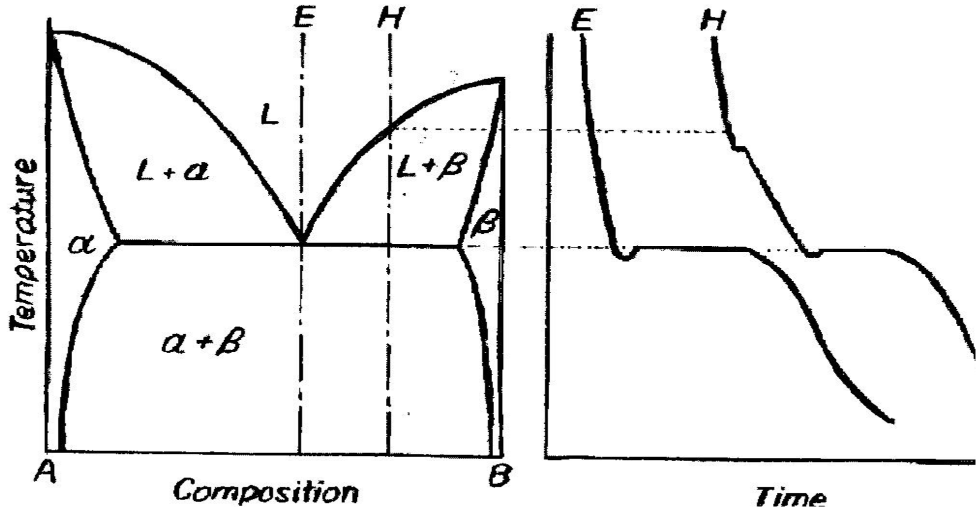

(a)

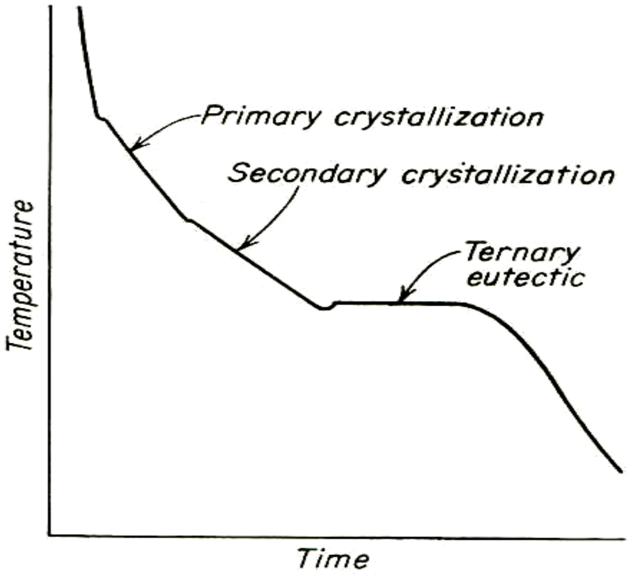

(b)

*Fig. 3.4 Cooling curves in (a) binary and (b) ternary eutectic system [14].*

Cooling curves of ternary and higher order systems are more complex. Fig. 3.4b is an example involving two thermal transitions in a ternary eutectic system [14]. The primary crystallization represents the first solid precipitating upon cooling. The second crystallization gives the information of forming an intermetallic compound until finally the eutectic isothermal arrest appears.

### 3.2.2 Differential Thermal Analysis (DTA)

Unlike the cooling curve analysis, DTA is a technique that involves the heating (or cooling) of a test sample and an inert reference under identical conditions and recording any temperature difference that develops between them [15]. In DTA, both the sample and the reference are in the same furnace and subject to identical heating or cooling conditions (Fig. 3.5).

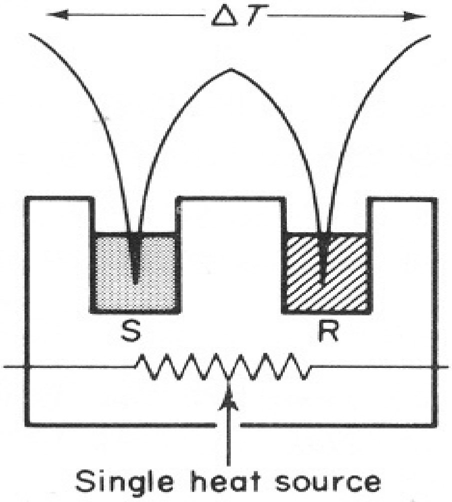

*Fig. 3.5 Schematic diagram of DTA [15]*

Any physical or chemical change occurring from the test sample will cause the temperature rising above or decreasing below that of the reference. Thus the differential temperature is plotted against time or temperature, and an exothermic or endothermic peak is generated. The term "differential" emphasizes the important feature of this technique: two measuring sensors (thermocouples) are used to obtain the temperatures from the sample and reference respectively, and the temperature difference between them is the signal of any change in phase. Due to the identical temperature program, the influence from thermal effects is equal on both sensors. This provides the advantage of high sensitivity to detect phase changes with a narrow freezing range.

### 3.2.3 Differential Scanning Calorimetry (DSC)

There are two types of differential scanning calorimetries depending on their operating principle. These are heat flux and power compensation. The set-up for heat flux DSC is similar to that of DTA, i.e., the sample and the reference are in the same furnace (Fig. 3.6a) [16]. This type of DSC is also called "Quantitative DTA". Instead of the temperature difference being recorded, the heat flux caused by the enthalpy or heat capacity is the signal that indicates the phase transformation. In power compensation DSC, there are still two measuring sensors, one for the sample and one for the reference, but the sample and reference are in separated furnaces (Fig. 3.6b). In this case, whenever a temperature difference occurs between the sample and reference, differential thermal power is supplied to the furnace to eliminate the difference and keep the temperature at the set value. Since it is a record of the energy vs. time/temperature, enthalpy or heat capacity of the sample can be measured.

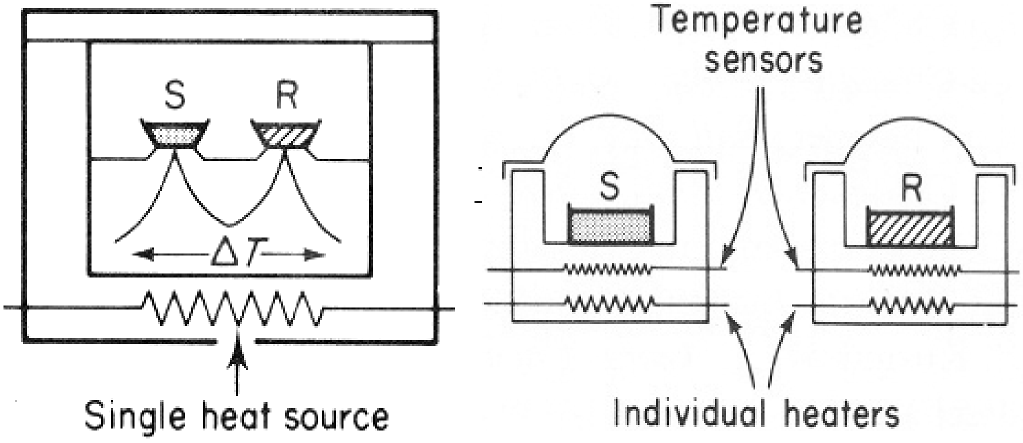

(a) (b)

*Fig. 3.6 Schematic diagram of (a) heat flux DSC, and (b) power compensation DSC [16].*

Both DTA and DSC are similar to cooling curve analysis, but because the sample is in closed and protected environment, it is more apt to controlling the operation parameters (heating/cooling rate, vacuum/inert gas) for different applications. The advantage of DTA/DSC over cooling curve analysis is that in solid-solid phase transition, when the heat evolution or absorption is negligible and difficult to detect by cooling curve technique, these could still be revealed by a DTA/DSC curve. The peak may never be as sharp as the one involving apparent heat evolution, however. A sudden discontinuity at the transition temperature can occur due to the different heat capacities of the two phases.

Another advantage of DTA/DSC is that only a small amount of sample is needed. For phase transition temperature determination, lowering the sample weight and the heating/cooling rate have the same effect as increasing the resolution of the peaks. For qualitative analysis, both DTA and DSC are equally good. However, for quantitative applications, DSC is claimed to give better results at low heating rates. With the improvement of instrument manufacturing, similar measurements can be obtained.

Certain features of the phase diagram, such as the liquidus surface can be determined by DTA/DSC with a series of compositions. In the study of the NaBr-$DyBr_3$ binary system, 27 samples covering the complete composition range were selected [17]. Fig. 3.7a shows the DTA curve at the eutectic composition with only one peak at heating and one at cooling. Fig. 3.7b is the solid solution composition where two peaks occurred corresponding to solidus and liquidus, respectively. Fig. 3.7c is the integrated thermal effects of all the compositions.

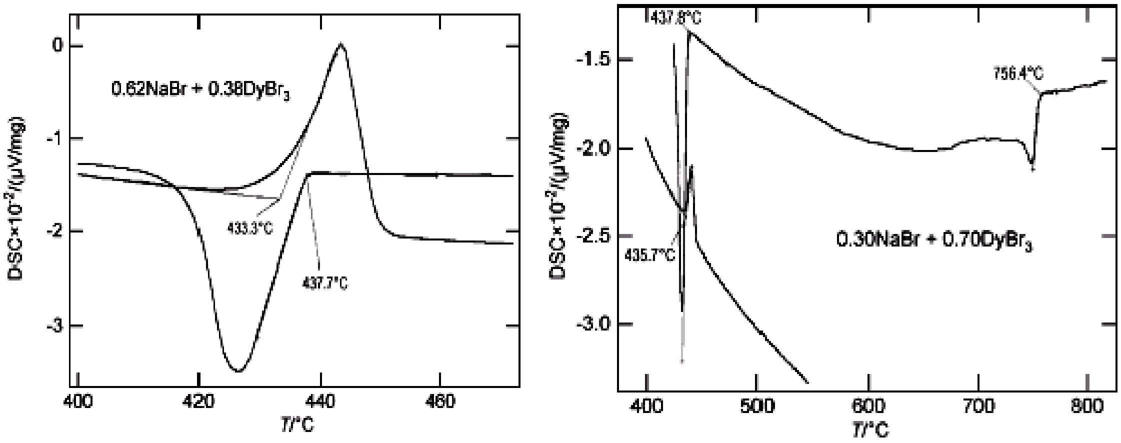

(a) (b)

*Fig. 3.7 DTA curves (a) at the eutectic composition of 0.62NaBr/0.38$DyBr_3$ , (b) Solid solution composition of 0.30NaBr/0.70$DyBr_3$.*

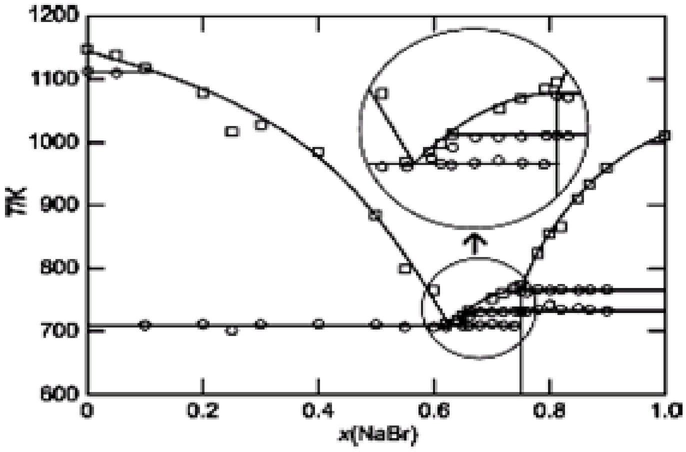

*(c)*

*Fig. 3.7(Continued) (c) DTA curves with integrated thermal effects of all the 27 compositions and the presentation of the phase diagram [17].*

## 3.3 Other Techniques for Phase Diagram Study

### 3.3.1 X-ray Diffraction (XRD)

X-ray diffraction is a very important characterization technique for the information on the crystal structure of materials: crystallite size, lattice parameter, chemical composition, and identification of unknown phase. In phase diagram studies, either the terminal solid solubility, or the solid solution ranges of intermetallic compounds are the important information to construct the phase diagram. As described for the techniques being reviewed above, thermal analysis (DTA/DSC), diffusion couples combined with EPMA and microscopic examination can establish the maximum solid solubility level under certain temperatures. However, X-ray diffraction has its own advantage in phase boundary determination: sensitive, easy to work with, and reliable.

Solid solution is a single phase solid region separated from the two phase solid region by a line called solvus. In the single phase region, the composition change leads to a change in lattice parameter, and the position of the diffraction peaks shifts. In the two phase region, even though the composition of the mixture changes, the composition of each phase remains constant. Therefore, the lattice parameter is a constant, too [14].

As shown in Fig. 3.8a, the lattice parameter increases linearly within the single phase region but remains constant in two phase region. According to the relationship between the composition and the lattice parameter, a series of alloy compositions across both the single and two phase regions can be annealed at temperature $T_1$ to reach equilibrium, and quenched to room temperature. The lattice parameters are calculated and can be plotted against the compositions. Since the inflection point from the Lattice Parameter-Composition graph on Fig. 3.8a is the saturated $\alpha$ phase at temperature $T_1$, the value of lattice parameter is thus the solid solubility of B in A at that temperature.

The similar way for the solid solubility limits at the other temperatures. Actually only one two-phase composition alloy is required (Fig. 3.8b) to be annealed at temperatures below the eutectic, because it always contains the $\alpha$ single phase. Again, the value of lattice parameters at a series of temperatures consists of the solvus line. In order to obtain precise lattice parameter measurements from X-ray diffraction data, sample preparation is probably the most important issue. This includes using powder to eliminate the preferred orientation to the incident X-ray beam, precise sample positioning for accurate peak positions, fine particle size to ensure sufficient number of particles to be analyzed, and optimizing the operating parameters of the instrument. It is also important to align and calibrate the diffractometer periodically to reduce the systematic errors and to ensure the good performance.

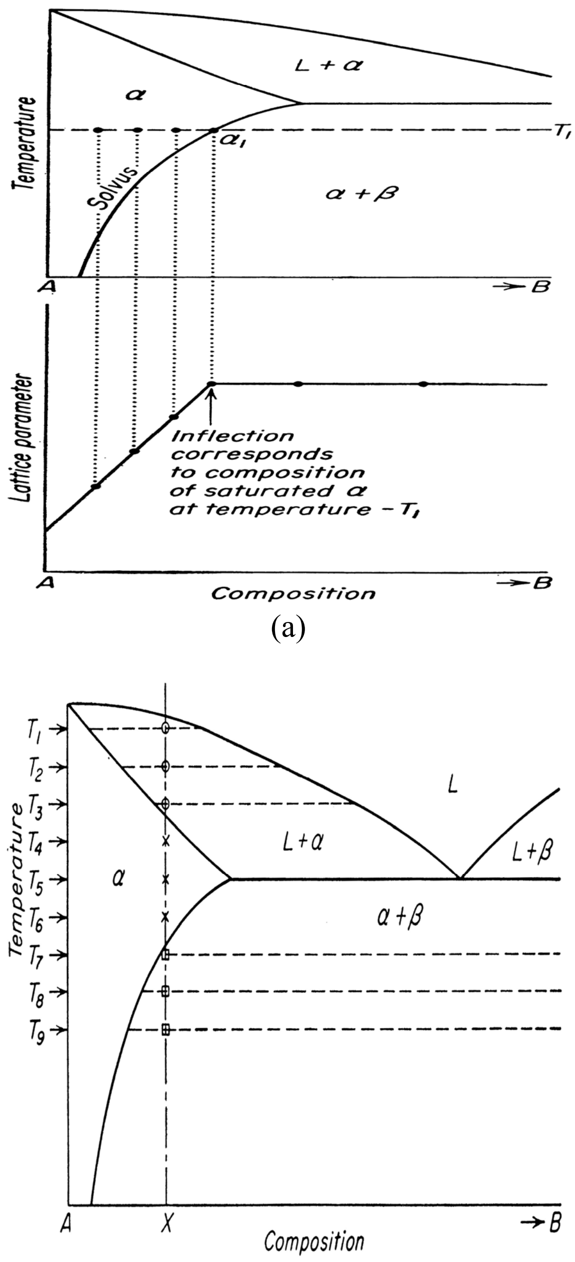

(a)

(b)

*Fig. 3.8 Use of lattice parameter measured by X-ray diffraction to determine the solvus line. (a) A series of single and two phase alloy compositions annealed at one temperature $T_1$, and (b) One two-phase composition annealed at a series of temperatures: $T_7$, $T_8$, $T_9$ [14].*

The indexing and analyzing of the peaks can be performed by several software programs, among which Rietveld method was developed to extract the maximum amount of information from a diffraction pattern and has been provided progress in the refinement of lattice parameter calculations of complex structures [18]. By putting the structure complexity (unit cell size, symmetry), data quality (peak resolution) and other information (bond length, chemical composition) into consideration, the use of Rietveld refinement can benefit the lattice parameters measurement related to very small solid solubility ranges.

### 3.3.2 Electrical Resistivity Method

Electrical resistivity measurement is adapted to locate the solid solution boundaries and univariant isothermal reactions. Like the lattice parameter, electrical resistivity changes with alloy composition in single phase solid solutions, but is never a constant in two phase regions [14]. Instead, the measured resistivity is determined by the rule of the mixtures of the two phases.

In practice, the resistivity of a series of alloys is measured either at the temperature of investigation, or after quenching from equilibrium heat treatment at that temperature. The resistivity can be plotted as a function of composition at a fixed temperature as shown in Fig. 3.9a, or as a function of temperature at fixed composition shown in Fig. 3.9b [14]. Like the lattice parameter, the inflection points in the curve are the limits of solid solution range. The resistivity-temperature curve is similar to the cooling curve, where the arrest corresponds to the eutectic transformation.

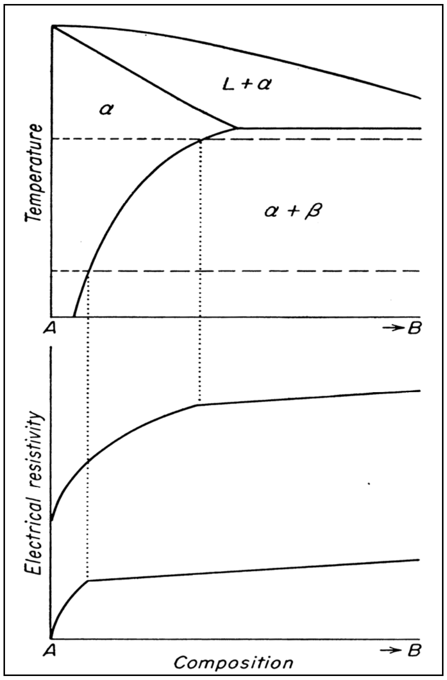

(a)

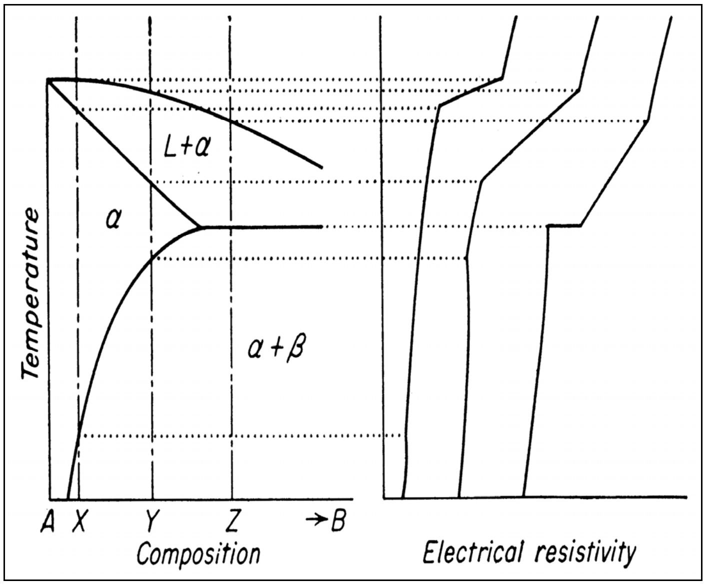

(b)

*Fig. 3.9 The measured electrical resistivity (a) as a function of composition, to determine the solvus line, (b) as a function of temperature, to determine the solvus, solidus, and eutectic line [14].*

## 3.4 References

1. K. Nonaka, T. Sakazawa, and H. Nakajima, “Reaction Diffusion in Mg-Cu System”, Materials Transactions, JIM, Vol. 36, No. 12, p.p. 1463-1466, 1995
2. D. M. Poole, P. M. Martin, and E. N. Hodkin, “Electron-Probe Microanalysis of Magnesium/Zirconium Diffusion Couples”, Journal of the Institute of Metals, 93(5), p.168,1964.
3. C. P. Heijwegen and G. D. Rieck, “Determination of the Phase Diagram of the Mo-Co System Using Diffusion Couples”, Journal of the Less-Common Metals, Vol. 34, p.p. 309-314, 1974.
4. T. Yamane, Y. Minamino, T. Sato, E. Itaya, Y. Miyamoto and M. Koizumi, “Solid Solubility Changes in Aluminum Base Binary Alloys Under High Pressure Measured By Diffusion Couple”, Defect and Diffusion Forum, Vols. 66-69, p.p. 1269-1274, 1989.
5. S. P. Gupta, “Intermetallic Compounds in Diffusion Couples of Ti with an Al-Si Eutectic Alloy”, Materials Characterization, Vol. 49, p.p. 321-330, 2003.
6. C. Q. Xia, F. H. Zeng and Y. Gu, “Al-rich Part Phase Relation in Al-Mg-Sc System at 430$^{o}$C”, Trans. Nonferrous Met. Soc. China, 13(5), p.p. 1124-1127, 2003.
7. K. Ishikawa, I. Ohnuma, R. Kainuma, K. Aoki, and K. Ishida, “Phase Equilibria and Stability of Heusler-type Aluminides in the NiAl-$Ni_2AlTi$-$Ni_2AlY$ (Y: V, Cr or Mn) System”, Journal of Alloys and Compounds, Vol. 367, p.p. 2-9, 2004.
8. R. Kainuma, J. Sato, I. Ohnuma, and K. Ishida, “Phase Stability and Interdiffusivity of the $L1_0$-based Ordered Phases in Al-rich Portion of the Ti-Al Binary System”, Intermetallics, Vol. 13, p.p. 784-791, 2005.

9. K. M. Kerimov, S. F. Dunaev and E. M. Sljusarenko, "Investigation of the Structure of Ternary Phases in Al-Mg-Ti, Al-Mg-V and Al-Mg-Cr Systems", Journal of the Less-Common Metals, Vol. 133, p.p. 297-302, 1987.
10. P. C. Tortorici and M. A. Dayananda, "Interdiffusion of Cerium in Fe-base Alloys with Ni or Cr", Journal of Nuclear Materials, Vol. 204, p.p. 165-172, 1993.
11. D. L. Martin, J. G. Smeggil, W. Hatfield and R. Bolon, "Eutectoid Decomposition of $Co_5Ce$", IEEE Transactions on Magnetics, Vol. May-11, No.5, 1975.
12. J. H. Buddery, M. E. Clark, R. J. Pearce and J. J. Stobbs, "The Development and Properties of An Oxidation-Resistant Coating for Uranium, Journal of Nuclear Materials", North-Holland Publishing Co., Amsterdam, 13(2), p.p. 169-181, 1964.
13. T. Fujita, Z. Horita, and T. G. Langdon, "Using Grain Boundary Engineering to Evaluate the Diffusion Characteristics in Ultrafine-grained Al-Mg and Al-Zn Alloys", Materials Science and Engineering, A371, p.p. 241-250, 2004.
14. F. N. Rhines, Phase Diagram in Metallurgy: Their Development and Application, McGraw-Hill Book Co. Inc, 1956
15. M. I. Pope, and M. D. Judd, Differential Thermal Analysis: A Guide to the Technique and its Applications, Heyden & Son Ltd., 1977
16. P. J. Haines (editor), Principles of thermal analysis and calorimetry, Cambridge: Royal Society of Chemistry, 2002
17. D. Kobertz, M. Miller, U. Niemann, L. Singheiser and K. Hilpert, "Study of theNaBr-$DyBr_3$ phase diagram by differential thermal analysis", Thermochimica Acta, Vol. 430, p.p. 73-77, 2005.
18. Course Notes, Quebec Workshop on Powder Diffraction and Rietveld Analysis, Trois-Rivieres, Quebec, May 2005

# CHAPTER 4

# OPTIMIZATION OF BINARY PHASE DIAGRAMS

## 4.1 Phase Equilibria Study of Mg-Ce System via Diffusion Couples*

(* This section has been published: X. Zhang, D. Kevorkov, M. Pekguleryuz, "Study of Phase Equilibria in Mg-Ce System via the Diffusion Couple Technique", **Magnesium Technology**, A.Luo, N. Neelameggham, R. Beals, Eds., TMS, 2006, pp. 441-4.)

A solid-liquid diffusion couple method was implemented to investigate the magnesium-cerium binary system. Pure Mg-Ce contact was vacuum-encapsulated in quartz tube and the Mg and Ce inter-diffused at 400°C. All the four single-phase zones corresponding to the Mg-Ce phase diagram were observed. The solid solubility ranges of the phases at magnesium-rich side were investigated by means of SEM line-scan. The phase identification was carried out by electron probe microanalysis (EPMA), and SEM. In order to investigate the composition range of the intermetallic compounds and clarify data in existing phase diagrams, alloys containing target phases were prepared, cast and annealed at a temperature range of 300-550°C. The room temperature and elevated-temperature (quenched) microstructures of these alloys were observed and the compositional variation of the intermetallic $Mg_{12}Ce$ was observed via EDS/SEM.

### 4.1.1 Introduction

Magnesium alloys containing rare earth alloying additions have attracted considerable interest from the transport industry due to the demand for high strength, light-weight materials at room and elevated temperatures. In most commercial magnesium alloys, rare earth metals are added as mischmetal or didymium, where mischmetal is a natural mixture of 50% cerium with the reminder being mainly lanthanum and neodymium. The influence of individual rare earth metals on the properties of magnesium has been demonstrated in several studies [1,2]. This may be explained by the different solubilities of rare earth elements in Mg, as well as the compounds formed in each Mg-rare earth metal system [3]. Certain binary magnesium-rare earth phase diagrams are still incomplete. For example, in the Mg-Ce binary system, the phase stability of the intermetallic compounds is still under question (Figure 1). Obviously, the composition ranges of these intermetallic compounds as well as their stoichiometry are important in alloy design.

Mg-Ce phase diagram (Fig. 4.1) exhibits six intermetallic compounds that are formed from liquid by peritectic reactions, except for $Mg_3Ce$ that melts congruently. When Vogel studied the system, $Mg_9Ce$ was postulated due to the similarity between magnesium-cerium and the magnesium-lanthanum diagram [4], until Wood and Cramer showed that three compounds formed peritectically ($Mg_{12}Ce$, $Mg_{17}Ce_2$, $Mg_{8.25}Ce$) in this composition region instead [5]. $Mg_{17}Ce_2$ has been repeatedly studied. Analysis of lattice parameters demonstrated that the compound could be Mg enriched and not the stoichiometric composition of $Mg_{17}Ce_2$ [6]. Hence, it was described by the formula $Mg_{10.3}Ce$. Still, the solid solution range of the compounds $Mg_{12}Ce$ and $Mg_3Ce$ are not determined exactly, and plotted in dotted lines on the phase diagram.

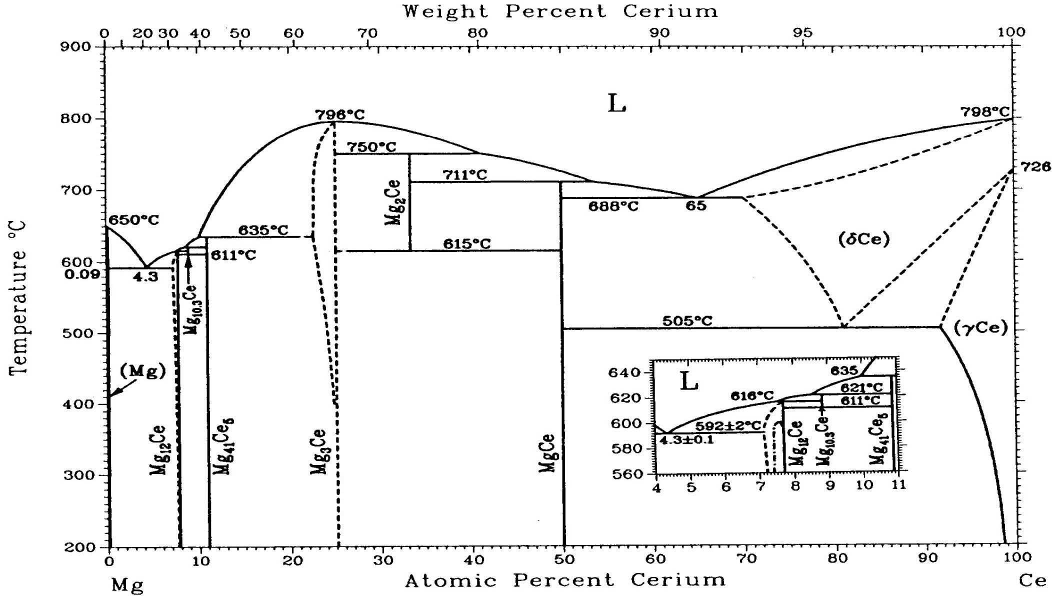

*Fig. 4.1 Mg-Ce phase diagram [3]*

Diffusion couples, which are based on the assumption of local equilibrium in the diffusion layer, are valuable tools in the study of multi-component phase diagrams. If the experiment is carried out for a sufficiently long time at a given temperature, steady state conditions can be achieved, and all the equilibrium phases are expected to appear. The objective of this paper is to study the stoichiometry of the $Mg_{12}Ce$ phase formed in the diffusion couple, and to further investigate its characteristics.

### 4.1.2 Experimental details

*Diffusion Couple*

A solid-liquid diffusion method was employed to make the Mg-Ce diffusion couple. A rectangular piece of cerium was polished with 320-grit SiC paper under paraffin oil, and then cleaned with acetone to ensure an oxide free surface. The melt was then taken from the furnace and cerium was submerged into it immediately. Due to the higher thermal expansion coefficient of magnesium ($26.0\times10^{-6}$ $K^{-1}$) compared to that of cerium ($8.0\times10^{-6}$ $K^{-1}$), an intimate contact between magnesium and cerium formed during solidification. The sample was then sectioned and encapsulated in a vacuum quartz tube as shown in Fig. 4.2. A titanium sponge getter was used in case any gas evaporation occurred at high temperature. The quartz tube was placed in a mechanical convection furnace, heat treated at 400°C for 14 days, and then quenched in cold air.

*Fig. 4.2 Quartz tube encapsulation of the diffusion couples*

Alloy preparation

High purity starting materials were used to prepare the Mg-Ce hypereutectic alloy: Mg ingot (99.96%) was supplied by Timminco, and Ce (99.7%) bulk was supplied by Hefa. Magnesium was sectioned into small pieces using a band saw, and cerium was cut with hacksaw under paraffin oil. Cerium sections were stored in paraffin oil to prevent oxidation. Pure magnesium was melted under a protective atmosphere of $SF_6$, cerium piece was cleaned with acetone to remove the oil and immediately immersed into the molten magnesium and dissolved at 700°C.

After melting, the alloy was poured into three copper moulds. Chemical compositions were analyzed by ICP (Table 4.1). Sections removed from the coupons were wrapped with tantalum foil, encapsulated in vacuum quartz tubes, and annealed for 50hrs at 530°C, 120hrs at 450°C, and 170hrs at 300°C. Specimens were quenched in liquid nitrogen at the end of annealing.

Table 4.1 Chemistry of the synthesized alloy

| Ce | Fe | Si | Ni | Zr | Mg |
|---|---|---|---|---|---|
| 24.942 | 0.0389 | 0.0015 | 0.0002 | 0.0013 | balance |

Material characterization

Samples from the diffusion couple and the synthetic alloy were subjected to microstructural observation, phase identification and electron probe microanalysis (EPMA). The samples were polished by conventional metallographic technique using diamond paste with oil-based extender. For the microstructural observation, two types of SEM were used: a JEOL840 equipped with EDS for qualitative phase analysis, and a JXA8900L equipped with WDS for quantitative analysis.

### 4.1.3 Results and discussion

Mg-Ce diffusion couple

Fig. 4.3 shows the different zones formed in the diffusion couple at 400°C. Five regions are visible from the pure Mg on the left to pure Ce on the right. The thickness of the layers varies from 200µm to 5µm owing to the different diffusion coefficients of magnesium and cerium atoms.

EPMA indicated the layers to be: eutectic, $Mg_{12}Ce$, $Mg_{41}Ce_5$, $Mg_3Ce$, and MgCe. The formation of the eutectic zone is due to the solid-liquid method of making the diffusion couple. When the cerium was immersed in molten magnesium, some of it dissolved, and the eutectic formed on its surface. The columnar $Mg_{12}Ce$ may have formed from the eutectic instead of from the pure magnesium, making the shape different from the other three planar layers.

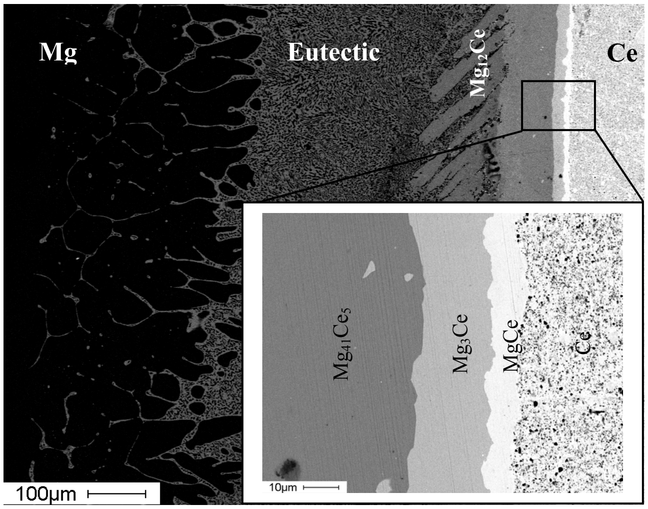

*Fig. 4.3 Diffusion layers formed between Mg and Ce at 400°C*

Table 4.2 EPMA measurement for the four interdiffusion layers

| | Mg (at%) | Ce (at%) | Mg/Ce ratio(stdev) |
|---|---|---|---|
| $Mg_{12}Ce$ | 90.10 | 8.36 | 10.78(0.18) |
| $Mg_{41}Ce_5$ | 87.56 | 11.39 | 7.69(0.05) |
| $Mg_3Ce$ | 73.24 | 24.68 | 2.97(0.03) |
| MgCe | 46.57 | 48.88 | 0.95(0.01) |

The zones were quantitatively analyzed by EPMA (Table 4.2). Although the measured Mg/Ce ratio for all the four phases is lower than the nominated values in the phase diagram, the compositional variation shown as the standard deviation (stdev) is large for $Mg_{12}Ce$ relative to the other three compounds. The earlier study from Johnson et al [7] showed similar results when analyzing a composition of $Mg_{12}Ce$ in a hypereutectic alloy to be $Mg_{11.59\text{-}11.71}Ce$, somewhat richer in Ce as compared with stoichiometry of the compound. This phase seems to exist over a compositional range.

In order to study the solid solution range of the phase $Mg_{12}Ce$, SEM line scans were obtained, and the results are shown in Fig. 4.4. Although the composition on each scan spot vibrates in both Mg and Ce spectra, the tendency to increase in cerium and decrease in magnesium can be observed. Essentially, in a given stoichiometric compound, the composition should be constant within the field; the increase of cerium or decrease of magnesium demonstrates a change in composition from point to point.

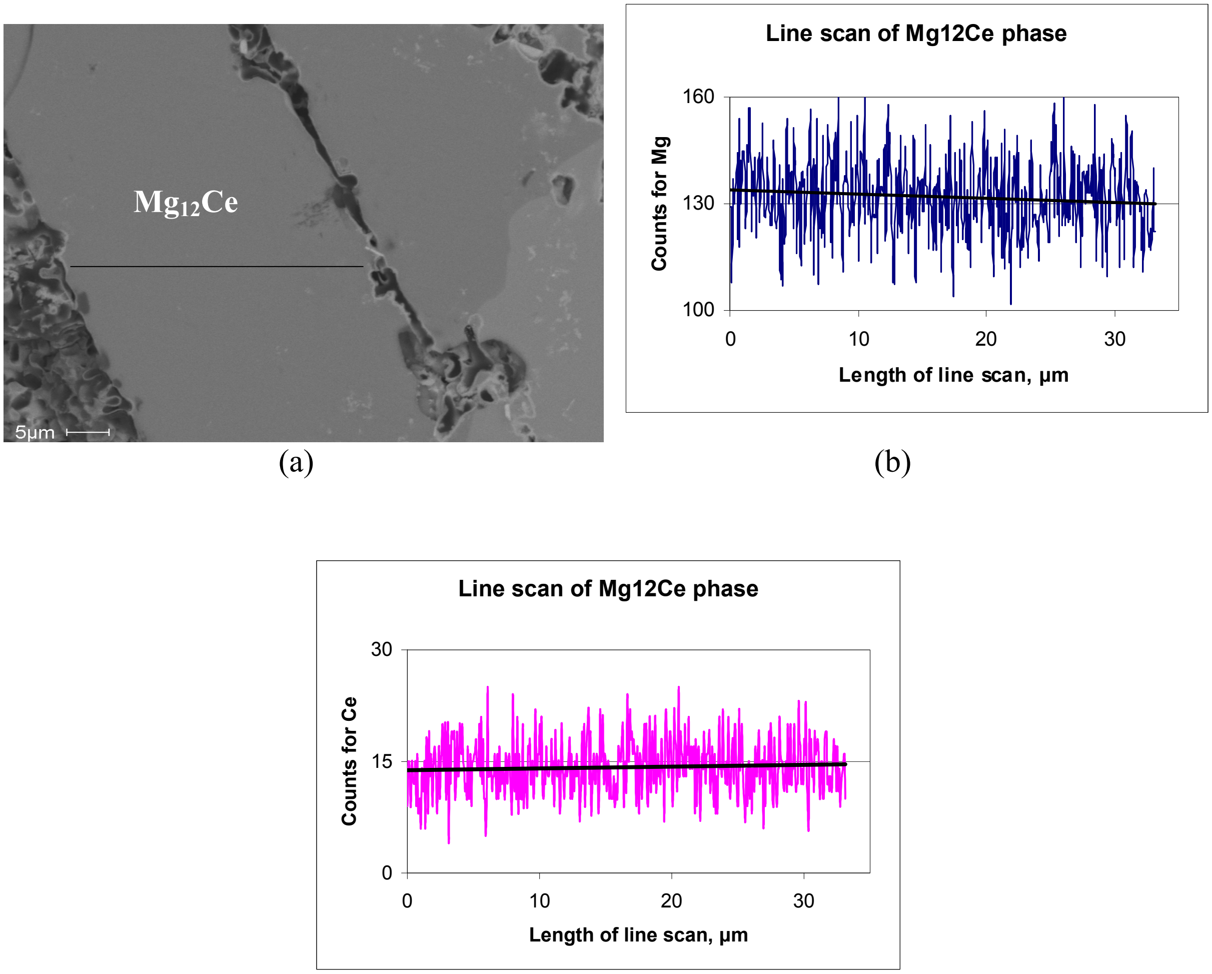

(a) (b)

(c)

*Fig. 4.4 The length of the line scan of the* $Mg_{12}Ce$ *phase(a), and compositional variations of Mg(b) and Ce(c).*

Synthetic Mg-Ce alloy

The phase boundaries of a compound may change with the temperature. In order to study the $Mg_{12}Ce$ at elevated temperature, an alloy containing 5.4 at% (i.e. 24.9 wt%) Ce was cast and annealed; its microstructure is shown in Fig. 4.5. The $Mg_{12}Ce$ crystals not only grew as temperature increased, but also the $Mg_{12}Ce$ in eutectic phase grew and joined together, which shows that the decrease of the eutectic with the increase of temperature.

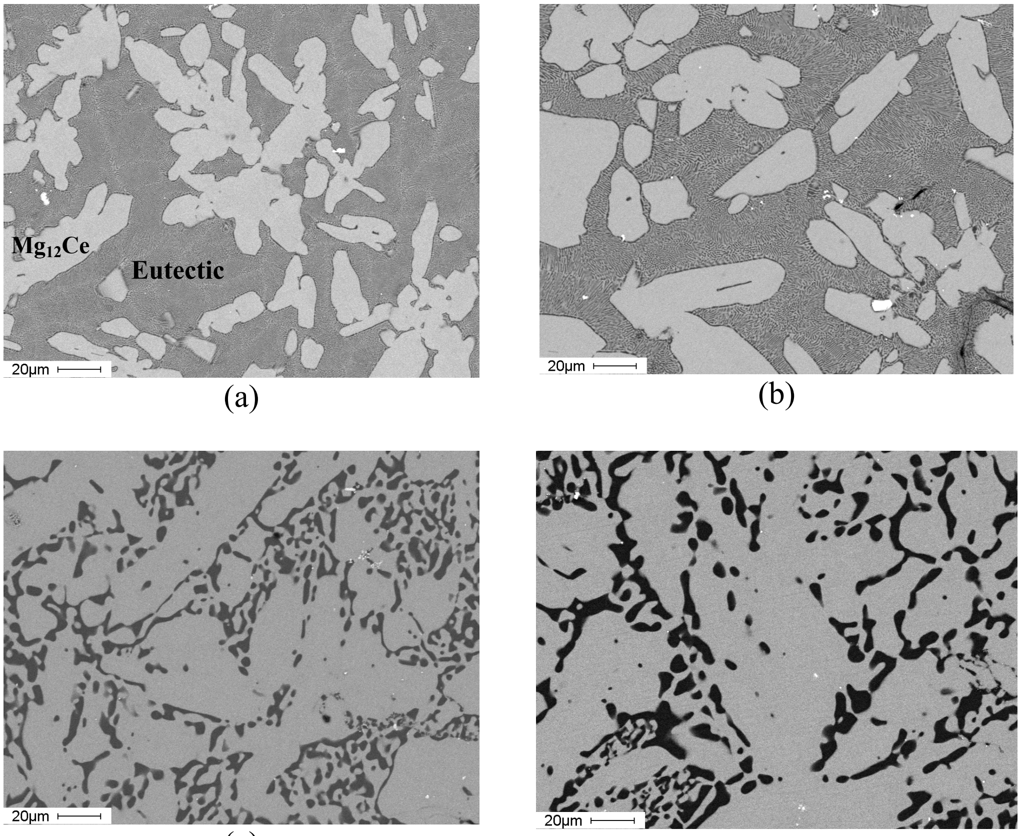

(a) (b)

(c) (d)

*Fig. 4.5 Mg-Ce alloy at (a) as cast, (b), (c), and (d) annealed at 300, 450 and 530$^oC$.*

The quantitative analysis of the $Mg_{12}Ce$ phase quenched from elevated temperatures demonstrates that the cerium concentration slightly decreases when the temperature increases from room temperature to 530°C (Fig. 4.6a). However, this change is only 0.2 at% and within the error limit. The Mg/Ce ratio also increases by 0.25 with the increase in temperature, illustrating a trend of increasing Mg atoms in the $Mg_{12}Ce$ structure at elevated temperatures (Fig. 4.6b). The standard deviation of Mg/Ce ratio at 530°C is higher than that at room temperature, which indicates the larger compositional variation.

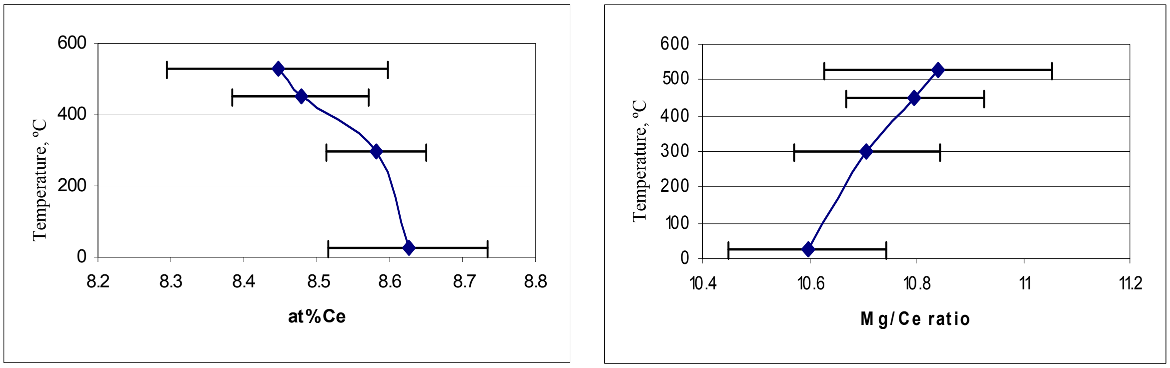

(a) (b)

*Fig. 4.6 (a) The decrease of cerium concentration in $Mg_{12}Ce$ with the increase in the temperature, and (b) the ratio of Mg/Ce increases slightly with the increase in temperature.*

Wood and co-workers proposed two structures to explain the complexity of this Mg-rich region. One is “normal $Mg_{12}Ce$” with the $Mn_{12}Th$ crystal structure produced during the eutectic reaction, the other is “ordered $Mg_{12}Ce$” containing long range order produced above the eutectic temperature [7]. The order-disorder reaction is composition sensitive, and therefore implies a certain solubility of Mg in $Mg_{12}Ce$ [5].

### 4.1.4 Conclusions

A study on the $Mg_{12}Ce$ phase in the Mg-Ce phase diagram has been conducted by comparing the compositions from diffusion couple and the synthetic alloy. The EPMA quantitative investigation, SEM line scans, and phase boundary change at elevated temperatures indicate a slight compositional variation, although in some cases this change is within the error limit. Future work will involve lattice parameter determination to further understand the crystal structure of $Mg_{12}Ce$ over a temperature range.

### 4.1.5 References

1. K. H. J. Buschow, “Magnetic properties of rare earth-magnesium compounds ($RMg_3$),” *J. Less-common Met.,* 44 (1976), 301
2. R. Ferro, S. Delfino, G. Borzone, A. Saccone, and G. Cacciamani, “Contribution to the evaluation of rare earth alloy system,” *J. Phase Equilibria,* 14(3) (1993)
3. T. B. Massalski, Chief Editor, *Binary Alloy Phase Diagrams, 2nd ed.* (Materials Park, Ohio: ASM International, 1990)
4. G. V. Raynor, *The Physical Metalurgy of Mangesium and its Alloys*, (Pergamon press Ltd., 1959)
5. D. H. Wood and E. M. Cramer, “Phase relations in the magnesium-rich portion of the cerium-magnesium system,” *J. Less-common Met.,* 9 (1965) 321-337
6. L. L. Rokhlin, *Magnesium Alloys Containing Rare Earth Metals: Structure and Properties,* (Taylor & Francis, 2003)
7. Q. C. Johnson, G. S. Smith, D. H. Wood and E. M. Cramer, “A New Structure in the Magnesium-Rich Region of the Cerium–Magnesium System,” *Nature,* 201( 1964) 600

## 4.2 Stoichiometry Study on the Binary Compounds at Mg-rich Corner of Mg-Ce System*

(*This section has been published: X. Zhang, D. Kevorkov, M. Pekguleryuz, "Stoichiometry Study on the Binary Compounds in the Mg-Ce System-Part I", J. Alloys Compounds, 475 (2009) 361-367)

The stoichiometry of two intermetallic compounds, $Mg_{12}Ce$ and $Mg_{41}Ce_5$, in the Mg-Ce binary system has been studied by means of SEM/Energy Dispersive Spectrometry (EDS), Electron-probe Microanalysis (EPMA) and X-ray diffraction (XRD) of synthesized and annealed alloys. On the Mg rich side of the present phase diagram study, the compositional range of $Mg_{12}Ce$ has been determined to be $Mg_{(11.17-10.81)}Ce$ at ambient temperature, and $Mg_{(11.31-10.75)}Ce$ at 530°C. $Mg_{41}Ce_5$, on the other hand, has been confirmed as a line compound, but with composition 11.3at% Ce, rather than 10.9at% Ce, as shown in existing phase diagrams. A modified version of the Mg-rich side of the Mg-Ce phase diagram is proposed, which includes two intermetallic compounds $Mg_{11}Ce$ and $Mg_{39}Ce_5$.

### 4.2.1 Introduction

Mg-Ce based alloys are known for their creep resistance, which is due, for the most part, to the existence of Ce-containing intermetallics in the microstructure [1,2]. The potential effect of these intermetallics can be analyzed with respect to their metallurgical/ thermal stability and stoichiometry. Metallurgical instability of an alloy can lead to creep-induced precipitation, which may create matrix strain and eventually lead to strain-induced grain boundary migration [3]; this can promote creep deformation. Non-stoichiometry of an intermetallic second phase is another factor which can lead to metallurgical instability of an alloy. Line (stoichiometric) compounds are desirable since they provide metallurgical stability at elevated temperatures. A fine distribution of a stoichiometric compound is important for microstructural refinement and resistance to creep deformation through grain boundary and dislocation pinning. Hence, non-stoichiometry of an intermetallic compound over a temperature range would govern and adversely affect the mechanical properties and behavior of the Mg-Ce based alloys.

There are two intermetallic phases, designated $Mg_{12}Ce$ and $Mg_3Ce$, in the Mg-Ce binary phase diagram [4] that have undetermined stoichiometry (Fig. 4.7). There are also two stoichiometric phases shown between these two phases, a high temperature phase $Mg_{10.3}Ce$, and $Mg_{41}Ce_5$. The two non-stoichiometric phases are indicated by dotted lines in the phase diagram (Fig. 4.7). $Mg_{12}Ce$ is the first intermediate phase on the Mg-rich side of the Mg-Ce system and is, therefore, an important second phase in magnesium-alloy design. $Mg_3Ce$, on the other hand, has the highest congruent temperature in the binary system, but the composition range is still under question. The study of this compound will be presented elsewhere, as Part II of this paper. The objective of present study is to determine the stoichiometry of $Mg_{12}Ce$ and the composition range if non-stoichiometry is observed. $Mg_{41}Ce_5$ phase is also investigated as part of the study.

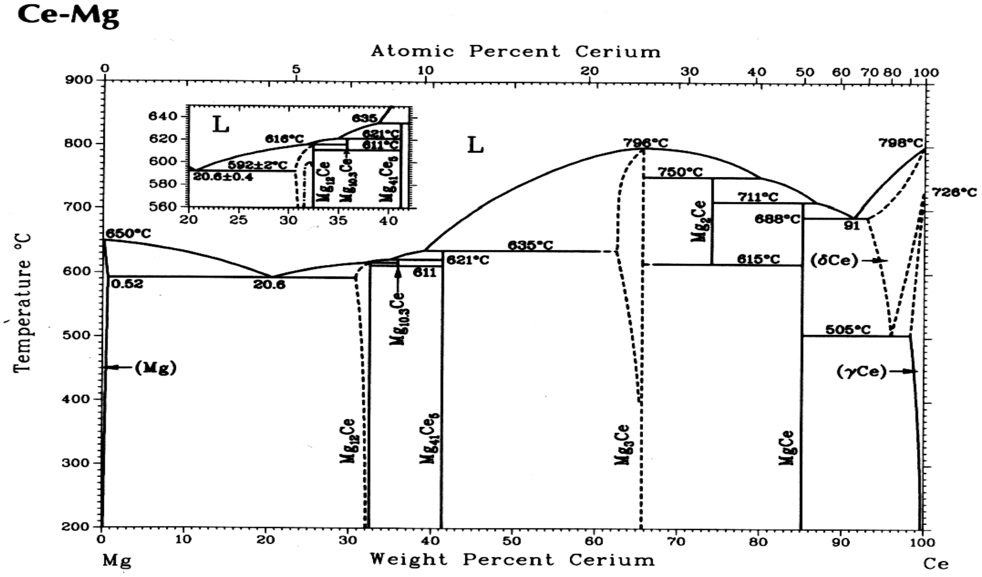

*Fig. 4.7 Mg-Ce phase diagram [4].*

### 4.2.2 Background

The Hume-Rothery rules for primary solid solution consider factors such as the atomic size, electronegativity, valency and crystal structure of solute and host metal. On Investigation of these factors for Mg and Ce (Table 4.3), it is found that only limited solid solution of Ce in Mg is possible due to differences in electronegativity and valency. Thus various intermediate compounds are formed. An attempt can be made to predict the intermetallics that may form between Mg and Ce based on the rules for compound formation. With the atomic radius ratio of $r_{Ce}/r_{Mg}$=1.14, Laves phases, that usually occur when the size differences are intermediate (around 20-30%), are not readily expected in the Mg-Ce system. The most likely scenario is the formation of electron compounds.

Table 4.3 Physical Properties of Mg and Ce

| | **Atomic radius (nm)** | **Electronegativity (Pauling scale)** | **Valency** | **Crystal Structure** |
|---|---|---|---|---|
| **Mg** | 0.160 | 1.31 | 2+ | HCP |
| **Ce** | 0.182 | 1.12 | 2+, 3+, 4+ | FCC |

Electron-to-atom ratio, e/a, is the ratio of the number of valence electrons contributed from the atoms in the stoichiometric formula to the number of atoms in the stoichiometric formula. For example, in the $Mg_{17}Al_{12}$ compound, the number of atoms is 17+12=29. Mg has +2 valency and Al +3, so the total number of valence electrons from these 29 atoms is (17x2) + (12x3)] = 70. Therefore the e/a ratio is 70/29 = 2.4. Hume-Rothery and his co-workers point out that electron-to-atom ratio, e/a, is important in controlling the formation of certain intermediate compound when the atomic size factor is small, i.e less than 18% [5]. For example, e/a = 3/2 gives disordered bcc or ordered CsCl-type structure, e/a = 21/13 gives the complex cubic γ-brass structure type, and e/a = 7/4 gives ε-brass HCP structure [5]. Because Ce can assume various valences (Table 4.3), its metallic radius and valence electrons would change. Furthermore, transition metals are also credited with zero valency because of their incomplete d-band, which makes it difficult to assign an e/a ratio and predict the structure types of Mg-Ce intermediate compounds. As a further complication, electron compounds exhibit different structural forms for the same e/a ratio. BCC phases that are stable at high temperatures may exist as HCP at low temperatures. Also, a high electrochemical factor results in ordered structures up to the melting point [6]. Order-disorder transitions may occur if compositions are at or near compositions that can be expressed by a simple formula such as AB, $A_3B$ or $AB_3$.

Another important structure type is the defect lattice. As the composition deviates from stoichiometry, and as the e/a ratio changes, the lattice incorporates a certain number of vacancies to prevent compound instability by maintaining the e/a ratio per unit cell. These structures would have increased entropy and as a consequence are stable at lower temperatures. Defect structures may result in anomalous decrease in both lattice parameter and in density [5].

## $Mg_{12}Ce$

In the phase diagram of the Mg-Ce binary system [4], a dotted line to the left of $Mg_{12}Ce$, shows a small compositional range, which increases when the temperature increases above ~450°C [4]. Two crystal structures have been previously reported for $Mg_{12}Ce$: a tetragonal structure ($ThMn_{12}$ type) below the eutectic temperature, and an ordered structure above the eutectic [7, 8]. These were determined via X-ray diffraction (XRD). Wood et al. [7] concluded that the transformation between long-range ordered/disordered $Mg_{12}Ce$ was possibly composition sensitive, implying some solid solubility of Mg in the $Mg_{12}Ce$ (Fig. 4.8). This does not fit the common assumption that ordered structures occur at or near AB, $A_3B$ or $AB_3$ compositions. The composition of the compound at room temperature was reported [8] to be $Mg_{11.59}Ce$ or $Mg_{11.71}Ce$, which is close to $Mg_{12}Ce$. However, the change of compositional range with temperature increase was postulated but not measured.

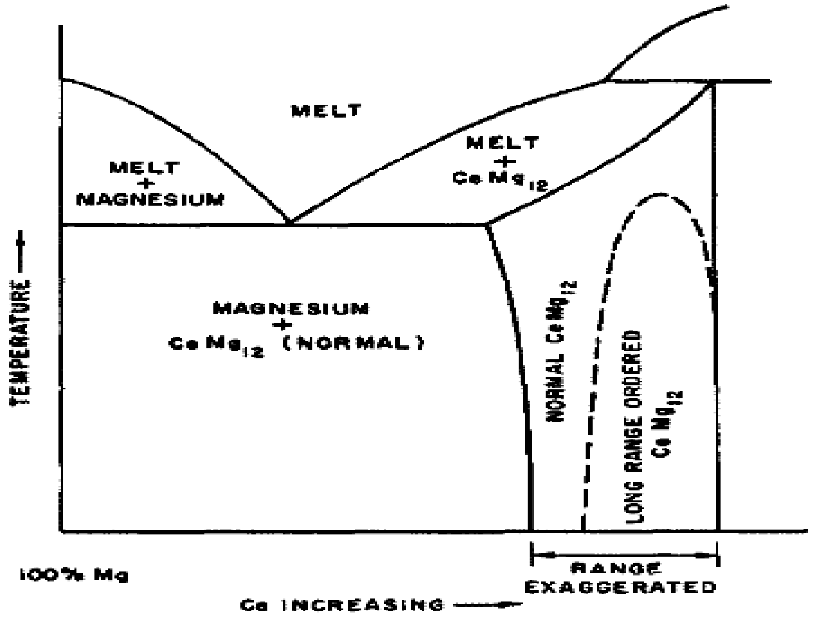

*Fig. 4.8 Suggested $Mg_{12}Ce$ section of the Mg-Ce by Wood et al [7].*

Fig. 4.9 illustrates the unit cell of $Mg_{12}Ce$ with the $ThMn_{12}$ tetragonal (Pearson symbol tI26) structure [9]. There are two (2) cerium and twenty-four (24) magnesium atoms in this unit cell with all the cerium atoms at the *2a* position, and magnesium atoms occupying the *8f*, *8i*, and *8j* positions. The coordination number is 12. $ThMn_{12}$ is a derivative of the $CaCu_5$ structure (Pearson symbol hP6) which is considered to be a topologically close-packed structure. $CeAl_8Mn_4$ is a superstructure to the $ThMn_{12}$ and the ordered substitution may occur from the parent $ThMn_{12}$ to $CeAl_8Mn_4$-type [10]. A multiple-substitution transformation is also possible from the parent $CaCu_5$ structure to the $ThMn_{12}$-type.

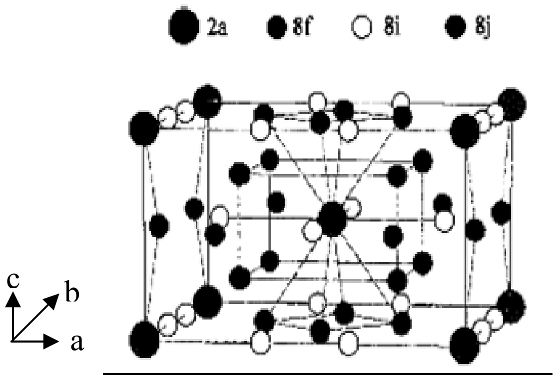

*Fig. 4.9 Unit cell of the* $ThMn_{12}$*-type structure [9].*

### $Mg_{41}Ce_5$ , $Mg_{17}Ce_2$ and $Mg_{10.3}Ce$

The stoichiometry of $Mg_{41}Ce_5$ was tentatively determined to be $Mg_{8.25}Ce$ ($Mg_{33}Ce_4$) by Wood *et al* in their study of the Mg-rich side of the Mg-Ce binary system [7]. It was further determined by Johnson *et al* to be $Mg_{42}Ce_5$ with a tetragonal structure [11]. It is interesting to note that in this structure the atomic positions of both Mg and Ce are the same as $Mg_{41}Ce_5$. Later, the authors identified the compound as $Mg_{41}Ce_5$ via single crystal diffractometry [12]. A structural similarity of $Mg_{42}Ce_5$ to $Mg_{17}Ce_2$ and $Mg_{12}Ce$ was recorded, in that the structures are superlattices of a hypothetical $CeMg_5$ compound with the $CaZn_5$ structure considered by Florio *et al.* [13]. $CeMg_5$ with $CaZn_5$ structure, however, has never been found. The authors also stated that there may be an additional compound in the region of $Mg_3Ce$ - $Mg_8Ce$ [11,12].

Compound $Mg_{17}Ce_2$ was also determined by Wood *et al.* [7] from the eutectoid decomposition to form $Mg_{12}Ce$ and $Mg_{41}Ce_5$ in a narrow temperature range of 621-611$^{o}$C. Three temperatures were used to detect the reaction: 300, 400 and 600$^{o}$C. After holding at 600$^{o}$C for 10min and cooled in air, the partial decomposition of $Mg_{17}Ce_2$ was shown. The composition was subsequently determined to be $Mg_{10.3}Ce$ by Johnson and Smith [11].

### 4.2.3 Experimental Procedure

$Mg_{12}Ce$

The stoichiometry of $Mg_{12}Ce$ was investigated by studying one sample on each side of the compound. XRD and EPMA (electron probe microanalysis) are the two methods used for the study. It is known that both the lattice parameters and the composition vary with temperature as well as with solute concentration in solid solution (single phase) region, whereas in two-phase region, they are constant. As shown in Fig. 4.10, XRD and EPMA are conducted on two samples located on both sides of the compound $Mg_{12}Ce$ at room and elevated temperatures. For a compound with a certain possible compositional range, stoichiometry can be established if lattice parameters of the compound in alloys from both sides of the compound are the same at each isothermal line. Non-stoichiometric compounds would also have a difference in chemical composition at the phase boundaries.

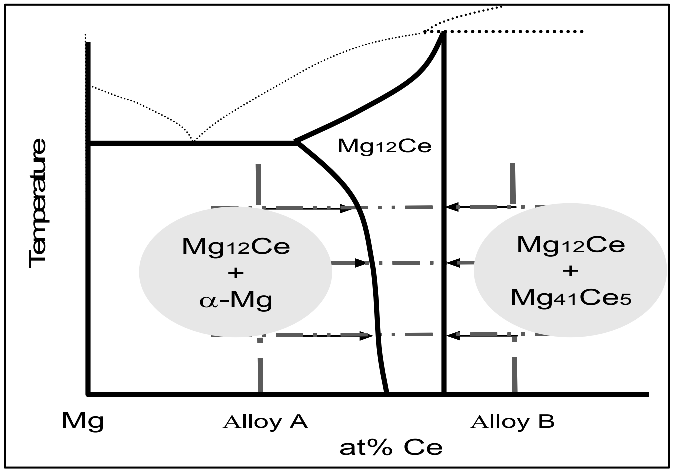

*Fig .4.10 The methodology for establishing stoichiometry of $Mg_{12}Ce$.*

Two alloys were synthesized from high purity Mg and Ce using a Norax induction furnace under $SF_6+CO_2$ protective gas to prevent melt oxidation. The composition of Alloy A was Mg-24.6wt% (5.36 at%) Ce, whilst the composition of

Alloy B was Mg-37.8wt% (9.55 at%) Ce. Alloy A is to the left side of the $Mg_{12}Ce$ stoichiometric composition (~7.69at% Ce); Alloy B is to the right side of the $Mg_{12}Ce$ boundary. The chemical compositions of the two alloys, as analyzed by ICP, are listed in Table 4.4.

Table 4.4 Chemical Compositions of the Synthesized Alloys (in wt%)

| | **Ce** | **Fe** | **Al** | **La** | **Si** | **Zn** | **Ca** |
|---|---|---|---|---|---|---|---|
| **Alloy A** | 24.6 | 0.002 | 0.012 | 0.015 | 0.004 | 0.010 | 0.001 |
| **Alloy B** | 37.8 | 0.060 | 0.002 | 0.003 | 0.005 | 0.006 | 0.008 |

The alloys were annealed at three temperatures: 530, 450 and 300$^{o}$C. The alloy samples were initially filed to produce powders, which were then sealed in quartz tubes, annealed at the chosen temperature for 5-50 hours, and then quenched in liquid nitrogen. The powder samples for room temperature measurements were produced by filing bulk samples. Annealing at 200$^{o}$C was carried out to eliminate filing stresses. XRD (Philips PW 1710 x-ray detector) was conducted on the powder samples. Si powder was added to samples as an internal standard to correct for systematic errors of the instrument. Powder Cell program (developed by Kraus and Nolze from Germany) was used to identify the $Mg_{12}Ce$ peaks of each sample, and then LATCON program (developed by Schwarzenbach and King from Belgium for parameters and standard deviations from 2θ diffraction angles) was used to calculate the lattice parameters, ***a*** and ***c***. Chemical composition of $Mg_{12}Ce$ at each temperature was determined using JEOL 840SEM equipped with energy dispersive spectrometry EDS for qualitative phase analysis. JXA 8900L Electron-Probe Microanalyzer (EPMA) equipped with WDS was used for quantitative analysis.

### 4.2.4 Results and Discussion

Fig. 4.11 are the microstructures of as-cast and heat treated Alloy A and B analyzed with SEM (Figs 4.11a-c) as well as EPMA (Fig. 4.11d). SEM/EDS results indicate that the main constituents in Alloy A are probably $Mg_{12}Ce$ and a eutectic structure. In Alloy B, $Mg_{12}Ce$, $Mg_{41}Ce_5$ and Mg3Ce are present; $Mg_{41}Ce_5$ seems to have formed from a peritectic reaction of $Mg_3Ce + L \rightarrow Mg_{41}Ce_5$.

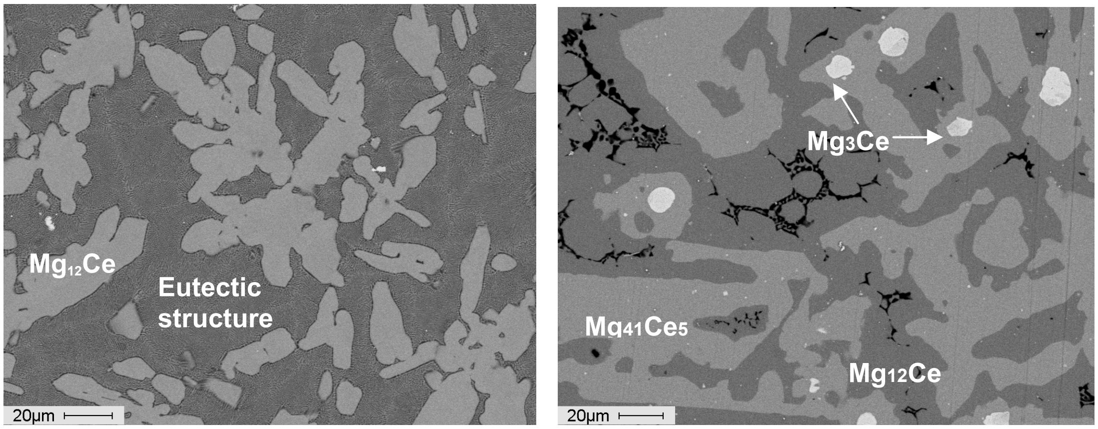

(a) Alloy A, as cast (b) Alloy B, as cast

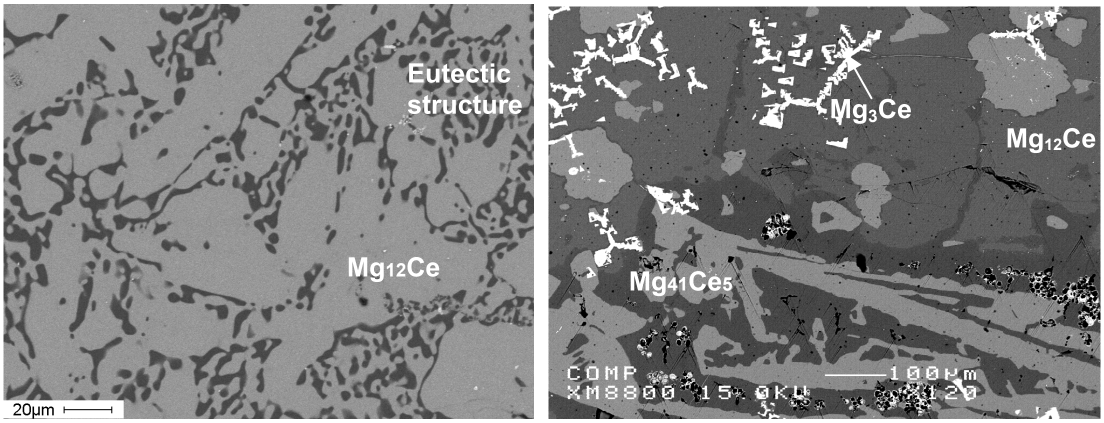

(c) Alloy A, 450 °C, 7days (d) Alloy B, 450 °C, 7days

*Fig. 4.11 Microstructure of Alloy A and B at ambient temperature (a) and (b), and after heat treatment (c) and (d).*

Table 4.5 gives a list of phase boundaries and composition ranges determined in this study. Compared to 7.69at%, the theoretical Ce value of $Mg_{12}Ce$, the measurement in this work shows a value of 8.22at% Ce at the left boundary, and 8.47at% Ce at the right. This phase is therefore postulated to be $Mg_{11}Ce$, with composition range of $Mg_{(11.17-10.81)}Ce$ at room temperature.

### $Mg_{12}Ce$

EPMA results on the chemical compositional analysis of $Mg_{12}Ce$ phase in Alloy A and B are shown in Table 4.5, and plotted in Figure 4.12 as a function of temperature. The values presented in the table are the mean values of 10 measurements. It can be seen that the compositional range increases with temperature from around 0.36 at% Ce at 25°C to 0.56at%Ce at 530°C. Fig. 4.12 shows the phase boundary data from both sides plotted as temperature versus Ce concentration. The right side tends to be a straight line within the error of measurement, and the left side is more open than the right side, which is similar to the existing binary phase diagram (Fig.1). However, this left boundary can be vertical within the experimental error.

Table 4.5 EPMA Results on $Mg_{12}Ce$ Phase in Alloys A & B

| Temperature (°C) | Ce composition in $Mg_{12}Ce$ (at% Ce) | | Composition Range of “$Mg_{12}Ce$” | Change in Composition Range (at% Ce) |
|---|---|---|---|---|
| | in Alloy A | in Alloy B | | |
| 25 | 8.22 (0.07)* | 8.47 (0.06) | $Mg_{(11.17-10.81)}Ce$ | 0.36 |
| 300 | 8.23 (0.10) | 8.50 (0.04) | $Mg_{(11.16-10.76)}Ce$ | 0.40 |
| 450 | 8.21 (0.06) | 8.52 (0.08) | $Mg_{(11.18-10.73)}Ce$ | 0.45 |
| 530 | 8.13 (0.08) | 8.51 (0.06) | $Mg_{(11.31-10.75)}Ce$ | 0.56 |

* Numbers in parentheses are the standard deviations of the measurements.

It is noted that the earlier EPMA study of the $Mg_{12}Ce$ phase in this work (Fig. 4.6) is slightly different from the results shown in Fig. 4.12. The earlier results (Fig.

4.6) used different standards and parameters which were later optimized; therefore, the results in Fig. 4.12 are to be considered more accurate.

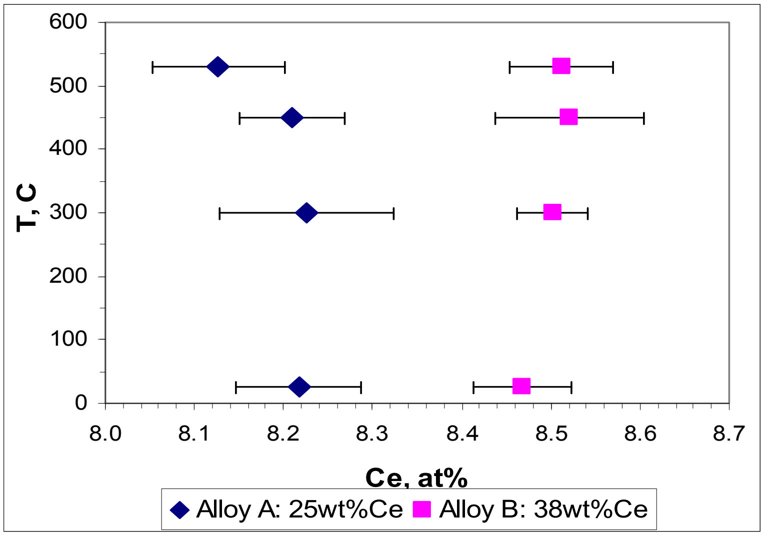

*Fig. 4.12 Phase boundaries established via EPMA.*

The lattice parameters of $Mg_{12}Ce$ calculated using XRD and LATCON are listed in Table 4.6. The differences are mainly observed in the second or third decimal points, except for the unit cell volume change where they are in the first decimal place. The error of the calculation at each temperature is small, which indicates that the accuracy of the calculations is good. Note that the reference ***a*** and ***c*** values from Pearson's handbook [14] are also given.

The general trends of lattice parameter and volume versus temperature are plotted in Fig. 4.13. It can be seen that the ***a***-spacing of the right boundary composition (phase $Mg_{12}Ce$ in alloy Mg-38wt%Ce) increases with temperature, while the ***c***-spacing of the right boundary composition decreases. Both ***a*** and ***c*** of the left boundary composition (phase $Mg_{12}Ce$ in alloy Mg-25wt%Ce) show a general increase with temperature. An increase in volume as temperature increases from 25 to 530$^{o}$C for both boundary compositions is evident; the increase in the left side is larger.

Table 4.6 Lattice Parameters of $Mg_{12}Ce$ at Different Temperatures

| **Sample** | **Temp, $^{o}$C** | **a, (Å)** | **a, (stdv)** | **c, (Å)** | **c, (stdv)** | **c/a** | **Volume, (Å$^3$)** | **V(stdv)** | **Error of fit** |
|---|---|---|---|---|---|---|---|---|---|
| **Alloy A : Mg-25wt%Ce** | 25 | 10.3265 | 0.0014 | 5.9585 | 0.0013 | 0.5770 | 635.388 | 0.179 | 2.42 |
| | 300 | 10.3286 | 0.0011 | 5.9595 | 0.0011 | 0.5770 | 635.752 | 0.137 | 3.32 |
| | 450 | 10.3437 | 0.0013 | 5.9716 | 0.0012 | 0.5773 | 638.827 | 0.156 | 2.36 |
| | 530 | 10.3340 | 0.0014 | 5.9637 | 0.0012 | 0.5771 | 636.873 | 0.164 | 2.39 |
| **Pearson** | | 10.33 | | 5.96 | | 0.5770 | 635.985 | | |
| **Alloy B : Mg-38wt%Ce** | 25 | 10.3185 | 0.0016 | 5.9656 | 0.0015 | 0.5781 | 635.166 | 0.181 | 2.87 |
| | 300 | 10.3191 | 0.0013 | 5.9655 | 0.0015 | 0.5781 | 635.230 | 0.190 | 3.03 |
| | 450 | 10.3255 | 0.0014 | 5.9630 | 0.0011 | 0.5775 | 635.741 | 0.145 | 2.83 |
| | 530 | 10.3308 | 0.0019 | 5.9622 | 0.0014 | 0.5771 | 635.710 | 0.156 | 2.63 |

Table 4.7 The Differences between Terminal Phases Lattice Parameters of $Mg_{12}Ce$ and Unit Cell Volumes at Each Temperature

| Temperature, $^{o}$C | Change in ***a***-parameter, $a_A$-$a_B$, (Å) | Change in ***c***-parameter, $c_A$-$c_B$ (Å) | Change in unit cell volume, $v_A$-$v_B$ (Å$^3$) |
|---|---|---|---|
| 25 | 0.0079 | -0.0071 | 0.222 |
| 300 | 0.0094 | -0.0060 | 0.523 |
| 450 | 0.0182 | 0.0087 | 3.086 |
| 530 | 0.0032 | 0.0015 | 1.163 |

(A) alloy from the left terminal, with 25wt% Ce (B) alloy from the right terminal, with 38wt% Ce

***a, c***, and ***v*** represent lattice parameter ***a*** and ***c***, as well as volume of the unit cell, respectively

Table 4.7 lists the difference of ***a, c*** and volume ***v*** at each temperature. Lattice parameter of phase $Mg_{12}Ce$ shows that at each temperature neither ***a*** or ***c*** at the left boundary is same as that at the right side. Any change of lattice parameters due to thermal expansion can be excluded because the XRD patterns were taken from the quenched powder at room temperature where atom vibrations due to thermal energy are negligible. These changes suggest that the expansion or contraction of the unit cell is most likely caused by the substitution of Mg or Ce.

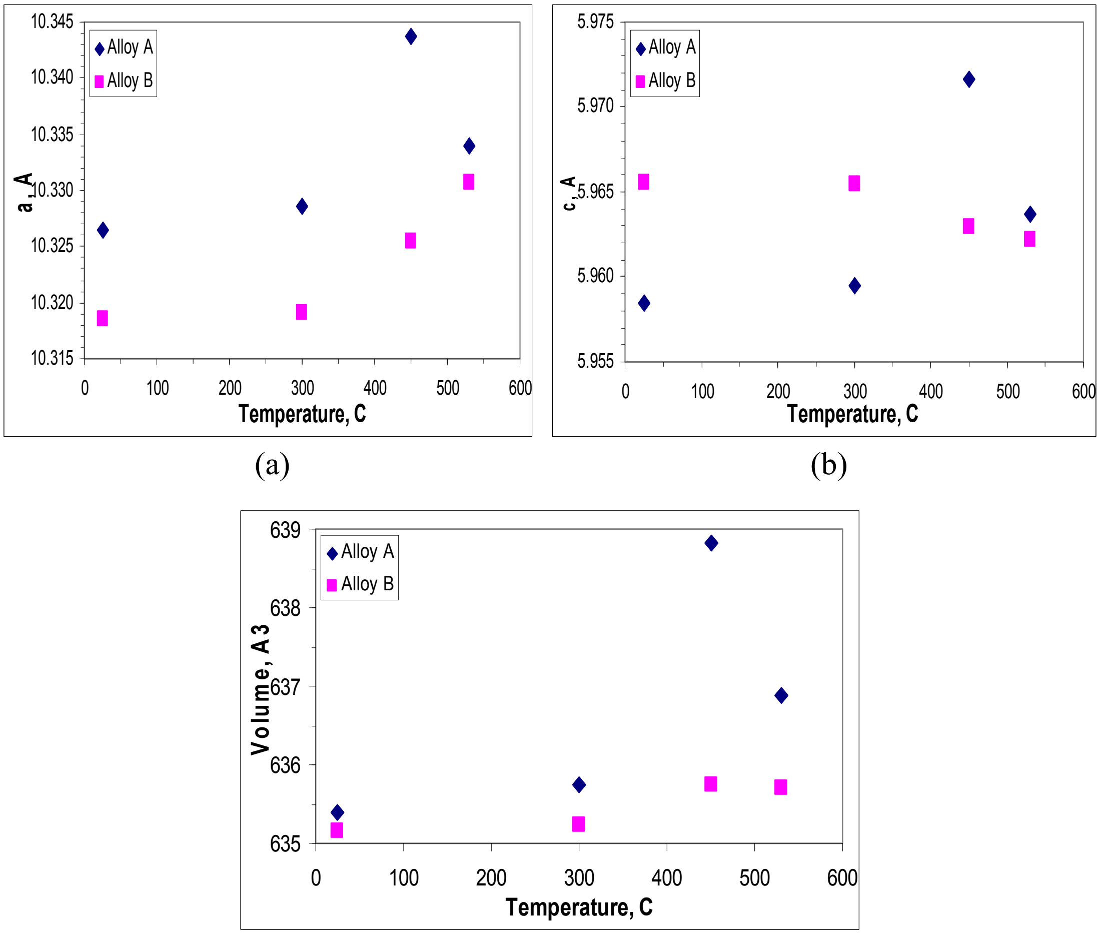

(a) (b)

(c)

*Fig. 4.13 General trends for lattice parameter: (a) a, (b) c and (c) volume v versus temperature.*

It is also clear that the volume measured at the left boundary of the $Mg_{12}Ce$ phase is always larger than that at the right side. This means that the increase in Ce concentration in the $Mg_{12}Ce$ phase causes a contraction of the unit cell. The atomic radius of Ce is higher than that of Mg and substitution of Mg by Ce should cause expansion of the unit cell. A possible explanation of this phenomenon is that in the

$Mg_{12}Ce$ solid solution the occupation of the crystallographic positions assigned for Mg atoms is less then 100%.

The statistical distribution of Mg atoms and vacancies in these positions can explain the observed experimental data. According to the crystal structure the composition of the phase should be $Mg_{12}Ce$ if the crystallographic positions are completely occupied. The experimentally determined composition is $Mg_{(11.17\text{-}10.81)}Ce$. The deficit of Mg can be attributed to the presence of vacancies in the Mg positions. An increase of Ce concentration in the $Mg_{12}Ce$ phase causes a decrease in the unit cell volume at each temperature. The substitution of Mg by vacancies may explain both increase of the Ce concentration and decrease of the unit cell volume. An alternative explanation may be that some Mg sites are substituted by Ce, which would lead to a change in e/a ratio. Electron concentration (e/a) would decrease if zero valency Ce substitutes the Mg sites.  Parallel with this, some Mg sites would be substituted with vacancies to maintain the e/a ratio and maintain compound stability.

The volume at the right side does not change much when temperature increases. Notably, the chemical composition on the same side obtained from EPMA shows small variation (Table 4.5). The phase boundary at right side can therefore be defined as a straight line at 8.5at% Ce. On the contrary, the phase boundary on the left side is open towards the left, and becomes wider at higher temperatures (Fig. 4.12). The maximum compositional range could be reached when the temperature increases until the eutectic. Hence, the compound $Mg_{12}Ce$ should really be renamed as $Mg_{11}Ce$, most probably a defect structure of $Mg_{12}Ce$ (i.e. the $ThMn_{12}$) with vacancies occupying Mg positions. This correlates with Johnson et al [12], who could not state the precise composition of $Mg_{12}Ce$, and who claimed that the formula was inferred from an approximate structure based on single-crystal evidence of previous work [8].

$\underline{Mg_{41}Ce_5}$

Phase $Mg_{41}Ce_5$ has been studied via EPMA in Alloy B. It is noted in Table 4.8 that the Mg/Ce ratio is constant irrespective of whether the sample is as-cast or annealed. This indicates the stoichiometry of this compound. The chemical composition, however, shows a departure from $Mg_{41}Ce_5$ formula. The Mg/Ce ratio is 7.8 rather than 8.2, giving $Mg_{39}Ce_5$ or $Mg_8Ce$ designation. This does not fit any of the stoichiometries postulated thus far for this compound ($Mg_{41}Ce_5$, $Mg_{17}Ce_2$, $Mg_{42}Ce_5$) [7,11,13], however, the existence of an additional compound in the region of $Mg_3Ce$ - $Mg_8Ce$ was suggested by Floria et al. [11,13]. The compound can also be a defect structure of $Mg_{41}Ce_5$ with vacancies occupying Mg positions.

Table 4.8 EPMA Results on $Mg_{41}Ce_5$ Phase in Alloys B at Different Temperatures

| **Sample** | **Mg, at%** | **Ce, at%** | **Mg/Ce** |
|---|---|---|---|
| Ambient | 87.67(0.11)* | 11.37(0.07) | 7.7 |
| 300 °C, 14 days | 87.62(0.09) | 11.23(0.03) | 7.8 |
| 450 °C, 7 days | 87.12(0.13) | 11.34(0.08) | 7.7 |
| 580 °C, 1.5hrs | 87.69(0.27) | 11.28(0.05) | 7.8 |

* Numbers in parentheses are the standard deviations of the measurements.

The eutectoid decomposition from $Mg_{17}Ce_2$ to $Mg_{41}Ce_5$ and $Mg_{12}Ce$ discussed by Wood [7] was not observed in this work. The measured right phase-boundary of $Mg_{12}Ce$ at both room and elevated temperatures, however, which is $Mg_{10.8}Ce$ (Table 4.5), is very close to the composition of $Mg_{10.3}Ce$ shown in the phase diagram, the existence of a separate $Mg_{10.3}Ce$ therefore requires further investigation and would probably be refuted based on the new compositional range of the $Mg_{11}Ce$ compound determined in this study. In fact, Johnson et al. were not certain [12] of the exact composition of the $CeMg_{10.3}$ $Th_2Ni_{17}$-type phase; the formula deduced from a single-crystal structure determination was not considered to accurately reflect the composition of the bulk material.

Both the as-cast and the annealed microstructures of Alloy B contain the $Mg_3Ce$ phase, and both the as-cast and the $450^{o}$C annealed microstructures show the presence of the $Mg_3Ce$ micro-constituent. This phase lies to the right of the $Mg_{41}Ce_5$ phase in the Mg-Ce binary phase diagram (Fig. 4.7). A peritectic reaction $Mg_3Ce$ + Liquid→ $Mg_{41}Ce_5$ is indicated for compositions close to the left of the $Mg_{41}Ce_5$ composition. The presence of this phase may be due to local segregation in the sample.

Suggested Phase Diagram

A suggested new phase diagram in the Mg-$Mg_{41}Ce_5$ section of the Mg-Ce system is presented in Fig. 4.14. $Mg_{12}Ce$ and $Mg_{41}Ce_5$ phases are replaced with $Mg_{11}Ce$ and $Mg_{39}Ce_5$ compounds, respectively. The $Mg_{10.3}Ce$ high temperature phase is removed. $Mg_{11}Ce$ has a narrow composition range, whilst the $Mg_{39}Ce_5$ is a line compound.

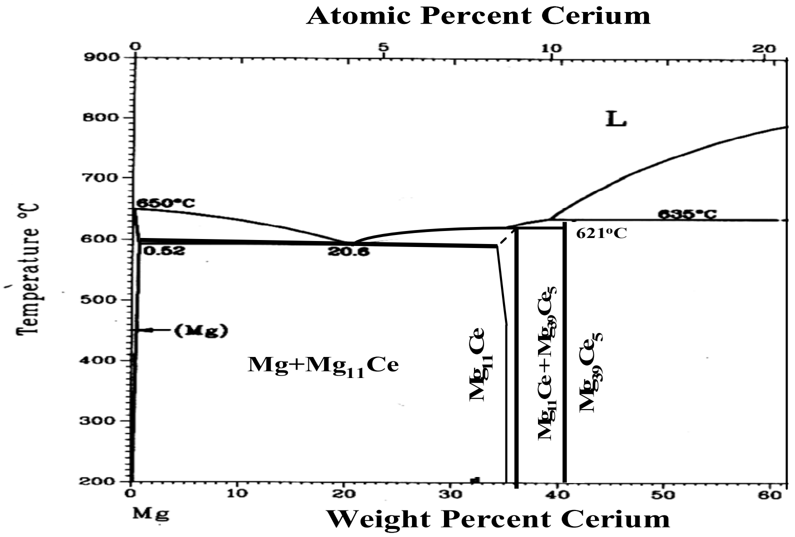

*Fig. 4.14 Suggested Mg side of the Mg-Ce system.*

### 4.2.5 Conclusions

1. The compositional range of phase $Mg_{12}Ce$ has been experimentally measured via EPMA and lattice parameters via XRD of terminal phase boundaries in the range 25- 530°C. The phase has been shifted from the current 7.69at% Ce to the right at 8.5at% Ce. The stoichiometry is re-designated as $Mg_{11}Ce$ with a small compositional range especially at 530°C. It is postulated that the phase is a defect structure of $Mg_{12}Ce$ with vacancies substituting Mg sites.

2. Phase $Mg_{41}Ce_5$ is a line compound which agrees with the previous studies. The position is located at 11.3at% Ce and the compound is designated as $Mg_{39}Ce_5$ rather than $Mg_{41}Ce_5$ at 10.9at% Ce.

3. A new version of the Mg-rich portion Mg-Ce phase diagram is suggested, which includes two intermetallic compounds $Mg_{11}Ce$ and $Mg_{39}Ce_5$. The high temperature phase $Mg_{10.3}Ce$ is excluded from the new phase diagram based on new data and the position and composition range of the $Mg_{11}Ce$ phase.

### 4.2.6 References

1. W. Mercer II, SAE Technical Paper No 900788, Detroit Michigan, Feb. 1990
2. I. J. Polmear, Light Metals: Metallurgy of Light Metals, 3rd ed., Arnold, London 1995
3. B. L. Mordike, K. U. Kainer (Eds.), Magnesium Alloys and their Applications, Werkstoff-Informationsgesellschaft mbH, Hamburger Allee 26, D-60486 Frankfurt, 1998, pp. 277
4. T. B. Massalski, (Chief Editor), Binary Alloy Phase Diagrams, 2nd ed., Materials Park, Ohio: ASM International, 1990

5. R. E. Smallman, and R. J. Bishop, Modern Physical Metallurgy and Materials Engineering, 6th Edition, Butterworth-Heinemann, 1999

6. C. W. Lung and N. H. March, Mechanical Properties of Metals: Atomistic and Fractal Continuum Approaches, World Scientific, 1999

7. D. H. Wood and E. M. Cramer, J. Less-Common Metals, 9 (1965) 321-337

8. Q. C. Johnson, G. S. Smith, D. H. Wood and E. M. Cramer, Nature, 201 (1964) 600

9. M. Zinkevich, N. Mattern, B. Wolf and K. Wetzig, Physica Status Solidi., A178 (2000) 671-679

10. J. H. Westbrook and R. L. Fleischer (Eds.), Crystal Structure of Intermetallic Compounds, John Wiley and Sons, 2000, pp.179

11. Q. Johnson and G. S. Smith, Acta Cryst., 22 (1967) 360-365

12. Q. Johnson and G. S. Smith, Acta Cryst., B26 (1970) 434-435

13. J. V. Florio, N. C. Baenziger and R. E. Rundle, Acta Cryst. 9 (1956) 367-372

14. P. Villars and L.D. Calvert, Pearson's Handbook of Crystallographic Data for Intermetallic Phases, 2nd ed., Materials Park, OH: ASM International, 1991

## 4.3 Stoichiometry Study on the $Mg_3Ce$ in the Mg-Ce System*

(*This section has been published: X. Zhang, D. Kevorkov, M. Pekguleryuz, "Study on the Binary Intermetallic Compounds in the Mg-Ce System", Intermetallics, 17 (2009) 496-503)

Electron-probe microanalysis (EPMA) and x-ray diffraction (XRD) studies conducted on Mg-38wt%Ce and Mg-66wt%Ce alloys demonstrated the existence of two distinct intermetallic phases, $Mg_4Ce$, $Mg_3Ce$, with the compositions $Mg_{3.6\text{-}3.7}Ce$, $Mg_{3.0\text{-}3.2}Ce$, respectively. XRD indicates that $Mg_4Ce$ is likely defect-vacancy structures of $Mg_3Ce$. The $\mu$-$Mg_3C$ phase, with the $Mg_{3.0}$-$_{3..3}Ce$ composition and a possible orthorhombic structure, has also been discovered, which is considered a metastable high-temperature form of the $Mg_3Ce$ phase. Based on these results a version of the phase diagram is suggested for the Mg-Ce system in the composition range of 38-70wt%Ce which correlates well with the solidification microstructures and phases of the two alloys.

### 4.3.1 Introduction and Background

It is known that magnesium-cerium based alloys can exhibit enhanced mechanical and corrosion properties [1]. However, the information on the phase selection and their stability are limited. The Mg-Ce binary system has many intermetallic compounds as shown in the phase diagram of Fig. 4.15a [2]. Recently, Zhang et al [3] studied the stoichiometry of two intermetallic compounds, $Mg_{12}Ce$ and $Mg_{41}Ce_5$, on synthesized and annealed alloys. The compositional range of $Mg_{12}Ce$ was determined to be $Mg_{(11.17–10.81)}Ce$ at room temperature, and $Mg_{(11.31–10.75)}Ce$ at 530°C. $Mg_{41}Ce_5$, was confirmed as a line compound with a composition of Mg-11.3 at% Ce. A modified version of the Mg–Ce phase diagram was proposed for the Mg-rich side, which includes two intermetallic compounds, $Mg_{11}Ce$ and $Mg_{39}Ce_5$ (Fig. 4.15b). In the present paper, solidification structures of two alloys (as-cast and annealed) are studied to investigate the phases with higher Ce compositions. Results related to the $Mg_3Ce$ compound are also reported as part of an ongoing study of the intermetallic phases in the Mg-Ce binary system.

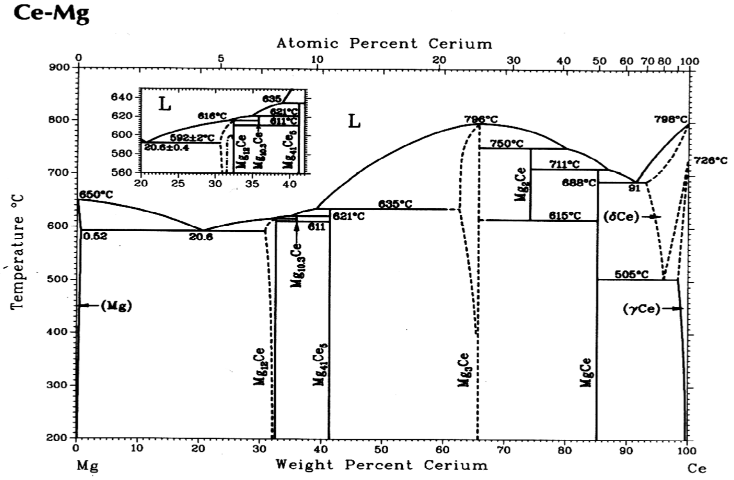

(a)

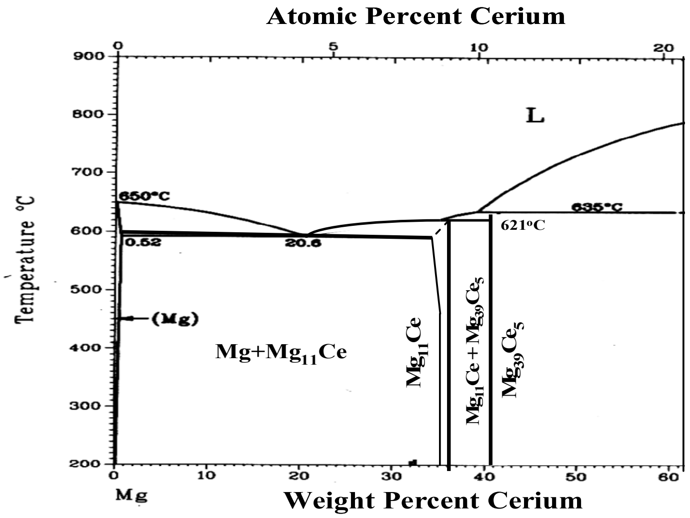

(b)

*Fig. 4.15 (a) Mg-Ce phase diagram [2], and (b) Suggested Mg-Ce phase diagram in the Mg-rich side [3].*

$Mg_3Ce$ is one of the six intermetallic compounds in the current Mg-Ce system. It exhibits the highest congruent melting temperature at 796°C in the phase diagram (Fig. 4.15a) and the most stable structural type: $D0_3$ (Pearson symbol cF16) [4]. $BiF_3$ crystal structure is used to describe its unit cell: four cerium atoms at the 4a position and twelve magnesium atoms at the 4b and 8c positions [5]. The ordered cubic D03 (cF16) crystal unit cell is also described as containing eight BCC-type subcells and as being composed of four interpenetrating FCC lattices (according to the system of Pearson symbols, the D03 lattice is classified as FCC) [6].

The only experimental studies on the $Mg_3Ce$ region of the Mg-Ce system phase were conducted in 1915 [7] and 1947 [8] by Vogel. There were striking differences between the two studies and both may be rather doubtful because the cerium that was used contained 6.5% impurities [9]. The latter work was assumed to be more correct where the $Mg_3Ce$ and a high-temperature Laves phase $Mg_2Ce$ were postulated. This later version is still used as the existing phase diagram [2] of the Mg-Ce system. A similarity was seen between the Mg-La and the Mg-Ce systems studied by Vogel and co-workers [8] and the $Mg_3Ce$ region of the phase diagram seems to have been assessed based on the expected similarity between Mg-Ce and the other Mg-Rare earth systems [9]. In the existing binary-phase diagram (Fig. 1a), a possible composition range at elevated temperature was postulated for $Mg_3Ce$ [2].

Mg and Ce have rather similar atomic radii and, while considered generally 3-valent, Ce may assume any valency between 2-4 (Table 4.9) and can even be credited with a zero valency when alloyed, so it is rather difficult to predict possible structure types between Mg and Ce. It has been claimed by Zintl [10] that when the different atoms of an alloy system are neither too different nor too similar in size, structures tend to form at simple atomic ratios which are similar in atomic arrangement to the ordered structures of FCC or BCC solid solutions. In these structures when the size factors are not too different, the like atoms keep apart so that the lattice strain caused by the solute is uniformly distributed in the lattice giving rise to ordered structures. $Mg_3Ce$ was previously considered to be a variant of the B2-caesium chloride structure (Pearson symbol cP2). In the BCC structure, several ordered arrangements are possible one being the caesium chloride type which gives rise to the MgPr, MgCe, MgLa structures [9]. It is also possible to form Laves phase between Mg-Ce where the atomic radii ratio is 1.14 which is close to the 1.2-1.3 ratio seen in Laves phases [11]. $Mg_2Ce$ is isomorphous with $Mg_2Cu$. A $Mg_4Ce$ phase with unknown composition is also mentioned by Raynor [9].

Table 4.9 Physical Properties of Mg and Ce

| | **Atomic radius (nm)** | **Electronegativity (Pauling scale)** | **Valency** | **Crystal Structure** |
|---|---|---|---|---|
| **Mg** | 0.160 | 1.31 | 2+ | HCP |
| **Ce** | 0.182 | 1.12 | 2+, 3+, 4+ | FCC |

### 4.3.2 Experimental Procedure

Two alloys, Mg-38wt%Ce (Alloy B) and Mg-66wt%Ce (Alloy C), were synthesized from high purity magnesium (impurities ≤0.04 wt%) and cerium (impurities ≤0.3wt%) using Norax Canada induction furnace under argon. Samples were kept in the furnace at 850$^o$C for 30min, and then slowly cooled to room temperature.

The alloys were then annealed at three temperatures, 580, 450 and 300$^o$C. The samples were wrapped with tantalum foil and vacuum-sealed in the quartz tubes, annealed at the above temperatures for 6.5h to 40 days, and then quenched in liquid nitrogen. No magnesium evaporation was seen inside the quartz tubes after annealing.

The high temperature anneals were stopped before any black stains indicating magnesium evaporation would appear.

Microstructure and chemical composition were analyzed with scanning electron microscope (SEM), electron probe microanalysis (EPMA-JXA 8900L). X-ray Diffraction (XRD-Philips PW 1710 x-ray detector) was used on powder samples for phase identification. Si powder was added to samples as an internal standard to correct for systematic errors of the instrument.

### 4.3.3 Results

1. Alloy C

*SEM/EPMA Analysis*

The alloy containing 66wt%Ce (Alloy C) is very close to the $Mg_3Ce$ composition in the phase diagram shown in Fig. 4.15a. The SEM images of the alloy, as-synthesized and after annealing at three temperatures, are shown in Fig. 4.16 and the EPMA analyses of the various phases in the microstructures are given in Table 4.10. The as-synthesized microstructure (Fig 4.16a) exhibits three phases: needle-shaped $Mg_2Ce$, dark gray $Mg_{3.6}Ce$ and the major phase $Mg_3Ce$ (Table 4.10). Mg/Ce ratio is 3.0-3.2 in the major phase. Mg/Ce ratio in the dark gray phase is 3.6-3.7. Both $Mg_{3.6}Ce$ and the $Mg_3Ce$ phase are present at all three annealing temperatures as seen in the SEM images (Figs. 4.16b-d) and the EPMA results (Table 4.10). The microstructures indicate that these two phases are distinct and not compositional variations of a solid-solution phase since they are clearly delineated by a phase boundary even after annealing. The microstructures of Fig. 4.16 also show the existence of the $Mg_2Ce$ phase. This solidification structure of Alloy C (66wt%Ce) cannot be explained by the existing phase diagram (Fig. 4.15a).

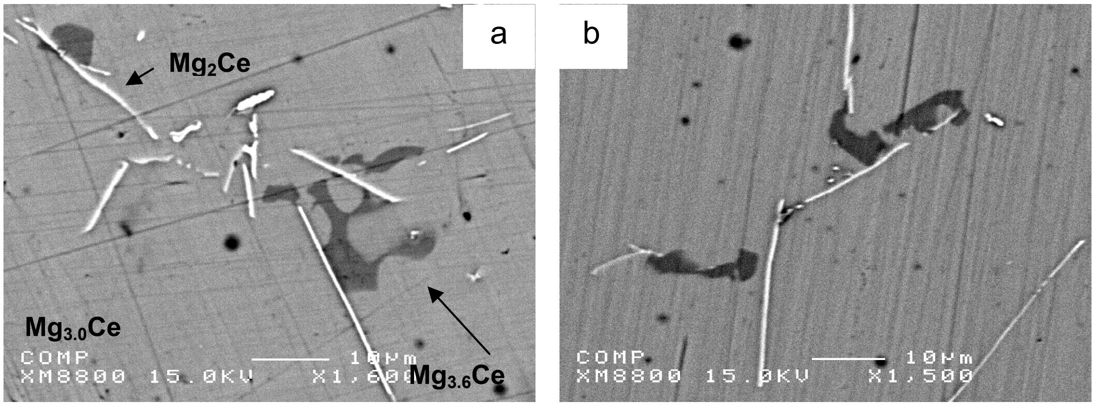

*as synthesized* *300°C, 40 days*

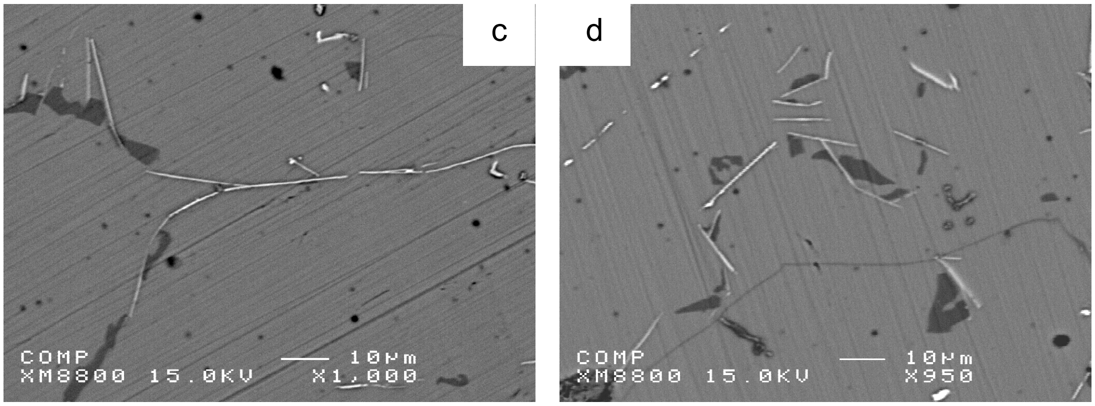

*450°C, 7 days* *580°C, 6.5h*

*Fig. 4.16 Alloy C as-synthesized and annealed at three temperatures.*

Table 4.10 EPMA Results for Alloys B and C

| Phase | Alloy condition | Alloy B | | | | Alloy C | | | |
|---|---|---|---|---|---|---|---|---|---|
| | | O, at% | Mg, at% | Ce, at% | Mg/Ce | O, at% | Mg, at% | Ce, at% | Mg/Ce |
| Mg$_{3.6}$Ce (Mg$_4$Ce) | As cast | 1.27 ±0.12 | 74.87 ±0.27 | 20.71 ±0.12 | 3.61 ±0.03 | 1.61 ±0.22 | 76.81 ±0.25 | 21.09 ±0.11 | 3.64 ± 0.02 |
| | 300°C, 40 days | 1.07 ±0.11 | 74.72 ±0.15 | 21.00 ±0.11 | 3.56 ±0.02 | 1.57 ±0.16 | 76.68 ±0.25 | 21.27 ±0.29 | 3.61 ± 0.06 |
| | 450°C, 7 days | 1.35 ±0.08 | 74.71 ±0.12 | 20.81 ±0.09 | 3.59 ±0.01 | 1.84 ±0.19 | 76.55 ±0.27 | 21.09 ±0.46 | 3.63 ± 0.09 |
| | 580°C, 6.5h | 1.24 ±0.14 | 75.14 ±1.01 | 21.09 ±0.21 | 3.56 ±0.02 | 1.70 ±0.19 | 77.02 ±0.25 | 20.78 ±0.20 | 3.70 ± 0.04 |
| Mg$_{3.2}$Ce (Mg$_3$Ce) | As cast | 1.51 ±0.13 | 75.66 ±0.35 | 22.61 ±0.29 | 3.34 ±0.06 | 1.48 ±0.16 | 73.95 ±0.65 | 24.50 ±0.53 | 3.02 ± 0.09 |
| | 300°C, 40 days | 1.37 ±0.10 | 73.54 ±0.32 | 24.84 ±0.33 | 2.96 ±0.05 | 1.33 ±0.08 | 74.76 ±0.18 | 23.85 ±0.16 | 3.13 ± 0.03 |
| | 450°C, 7 days | | | | n/a | 1.67 ±0.19 | 74.62 ±0.27 | 23.65 ±0.12 | 3.16 ± 0.03 |
| | 580°C, 6.5h | | | | n/a | 1.67 ±0.18 | 74.79 ±0.29 | 23.48 ±0.20 | 3.19 ± 0.04 |

*XRD Analysis*

The XRD results of Alloy C in the two conditions (as-synthesized and annealed at 580°C) do not show any significant difference (Fig. 4.17). There are no unknown peaks in the XRD spectrum. The peak positions correspond to the Mg$_3$Ce phase. All peaks are slightly shifted including the Si peaks. This means that both the Mg$_3$Ce and the Mg$_{3.6}$Ce in Alloy C may have the Mg$_3$Ce structure, however, they cannot be considered to be a composition range of Mg$_3$Ce, because in the Alloy-C microstructure the two phases (Mg$_{3.6}$Ce and Mg$_3$Ce) exist separately. It can be postulated that Mg$_{(3.6-3.7)}$Ce phase is the Mg$_4$Ce phase discussed by Raynor [9].

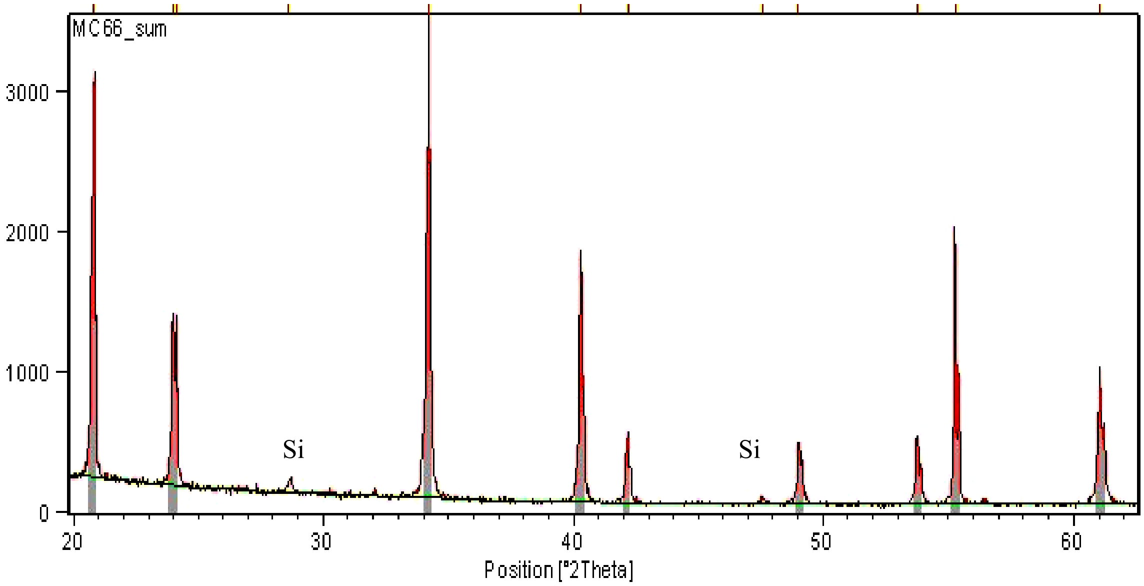

(a)

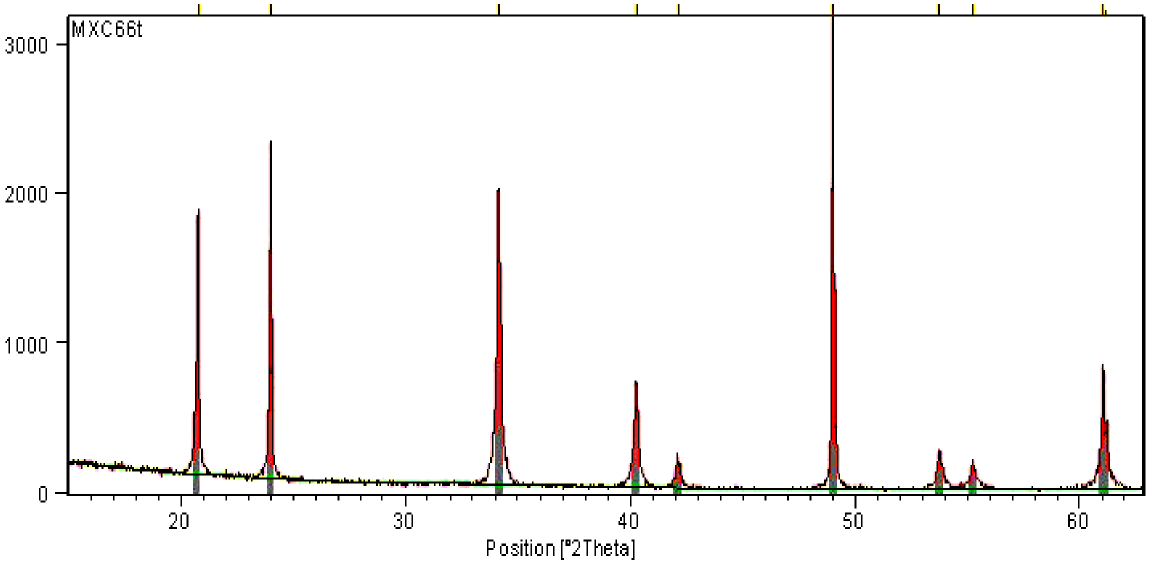

(b)

*Fig. 4.17 XRD of Alloy C: (a) As-synthesized (b) annealed at 580$^{o}$C with the index of $Mg_3Ce$.*

## 2. Alloy B

### *SEM/EPMA Analysis*

The SEM micrographs of Alloy B which has 38wt%Ce are shown in Fig. 4.18 and the EPMA analyses are given in Table 4.10. Four phases are observed in the as-cast condition (Fig 4.18a & b). These are the dark grey Mg, the grey $Mg_{11}Ce$ followed by light grey $Mg_{39}Ce_5$ formed from a peritectic reaction and the primary white $Mg_3Ce$, as determined by EPMA analysis (Table 4.10). Mg-38wt%Ce is very close to the $Mg_{39}Ce_5$ compound and lies on the Mg-rich side. The as-cast (non-equilibrium) structure of the alloy, at first analysis, can be explained by the suggested phase diagram of Zhang et al [3] (Fig. 4.15b). The formation of the primary phase $Mg_3Ce$ is followed by the peritectic reaction $L+Mg_3Ce \rightarrow Mg_{39}Ce_5$ which is then followed by the peritectic reaction $L+ Mg_{39}Ce_5 \rightarrow Mg_{11}Ce$. The existence of Mg is probably due to a solid-state precipitation from $Mg_{11}Ce$ as the alloy cools down.

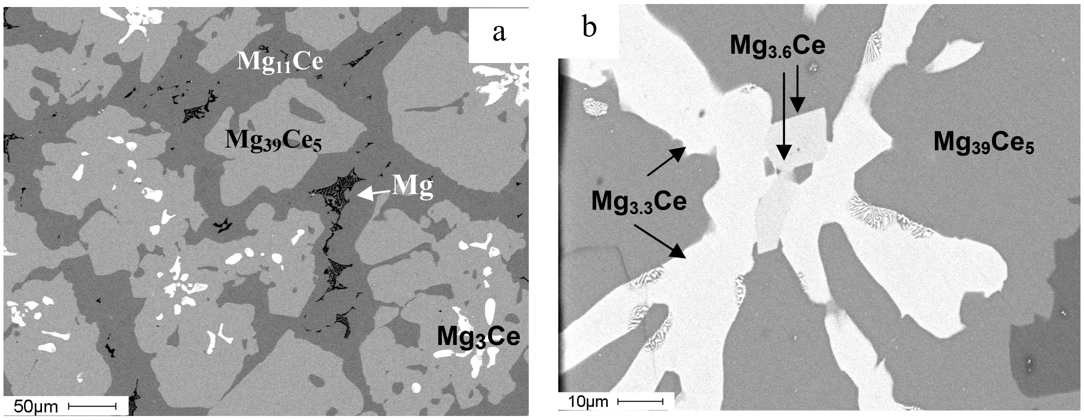

*As synthesized*

*Fig. 4.18 (a)-(b) Alloy B as-synthesized*

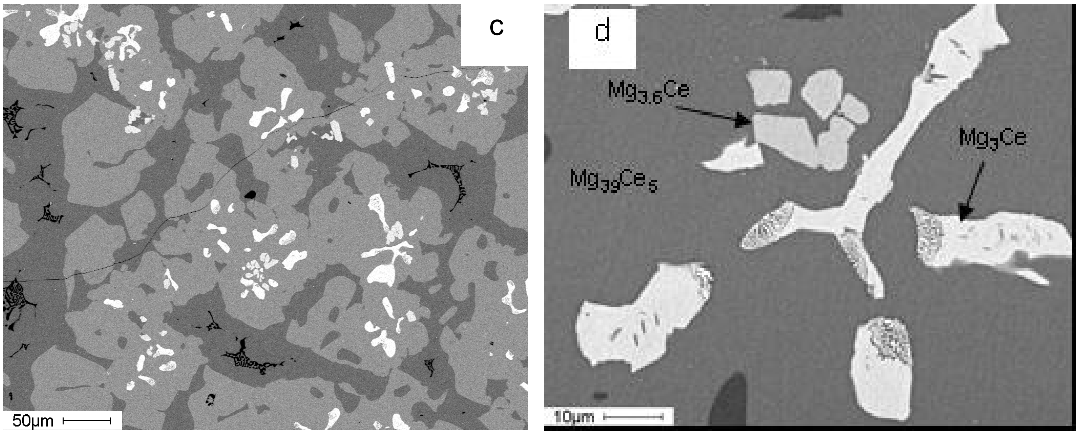

*$300^{o}$C, 40 days, quenched in liquid nitrogen*

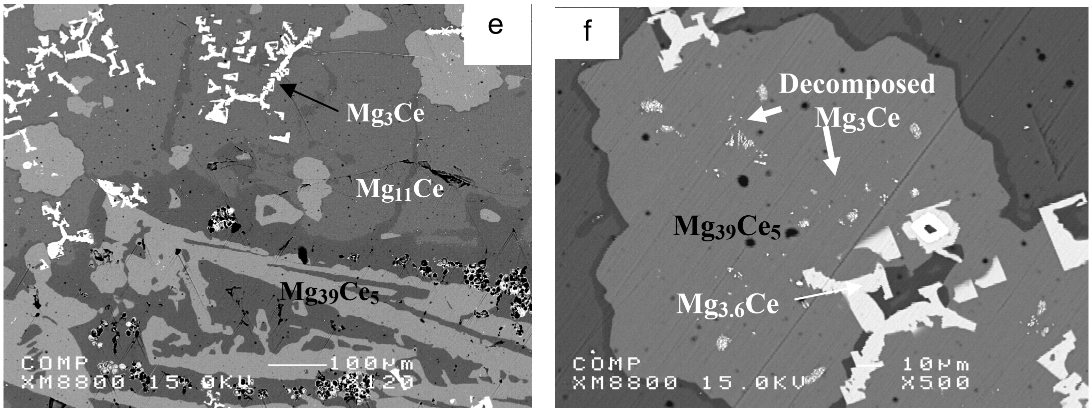

*$450^{o}$C, 7 days, quenched in liquid nitrogen*

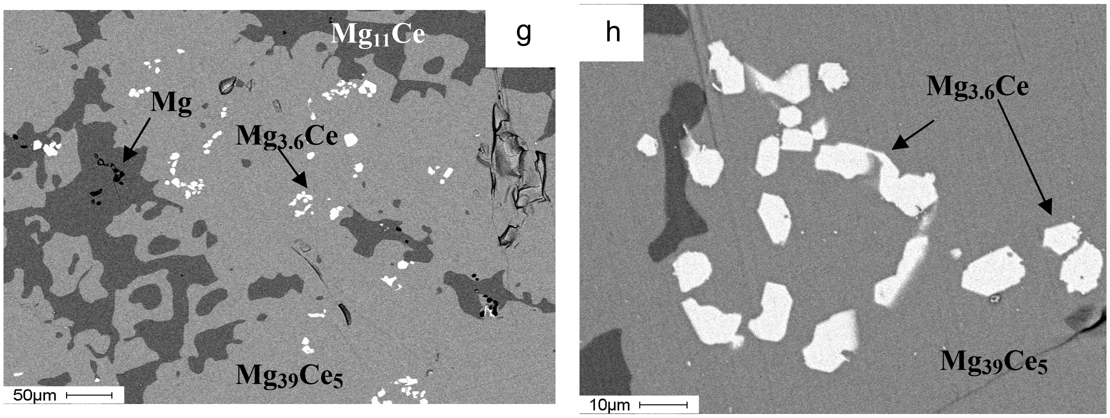

*$580^{o}$C, 6.5h, quenched in liquid nitrogen*

*Fig. 4.18 (Continued) (c)-(d) Alloy B as-synthesized and heat treated at three temperatures.*

Upon close observation of phase $Mg_3Ce$, however, two different morphologies were found (Fig. 4.18b). One is faceted with higher Mg content ($Mg_{3.6}Ce$), and another is in irregular shaped with the $Mg_{3.3}Ce$ composition (Table 4.10). Hence, the existence of an $Mg_4Ce$ compound is also observed in this alloy.

When the sample is annealed at 300$^oC$ for 40 days, the microstructure remains almost the same as the as-synthesized condition (Fig. 4.18c & d). Both morphologies can still be observed, but the $Mg_{3.3}Ce$ phase composition becomes $Mg_3Ce$. When the annealing temperature is increased, the decomposition of the irregular $Mg_3Ce$ at 450$^oC$ (Fig. 4.18e & f) is seen until its complete disappearance at 580$^oC$ (Fig.4.18g & h). However, $Mg_{3.6}Ce$ remains in the structure at all temperatures, without any substantial change (Table 4.10). It should be noted that this structure cannot be explained by the current phase diagram of Fig. 4.15a.

*XRD Analysis*

XRD was conducted on the synthesized and annealed samples. Results from Alloy B in Fig. 4.19a and b show that most of the peaks are identified as $Mg_{12}Ce$, $Mg_{41}Ce_5$, $Mg_3Ce$ corresponding well with the microstructure and as Si which was the internal standard. $Mg_3Ce$ peaks exhibit weak intensity because the amount of this phase is very small. However, it should be noted that there are five peaks in both the as synthesized and annealed samples (Fig. 4.19a and b) that do not belong to any of the four phases ($Mg_{12}Ce$, $Mg_{41}Ce_5$, $Mg_3Ce$, Si). When comparing the five peaks from the samples before and after heat treatment (Fig. 4.19c) it is found that the five peaks disappear when annealed at 580$^oC$. Therefore, these unknown peaks may be associated with the $Mg_{3.0}$-$_{3.3}Ce$, considering the fact that this phase disappears in the microstructure after annealing at 580$^oC$. The $Mg_{3.6}Ce$ phase on the other hand is persists in the structure at all temperatures and the XRD peaks for this phase correspond to the $Mg_3Ce$.

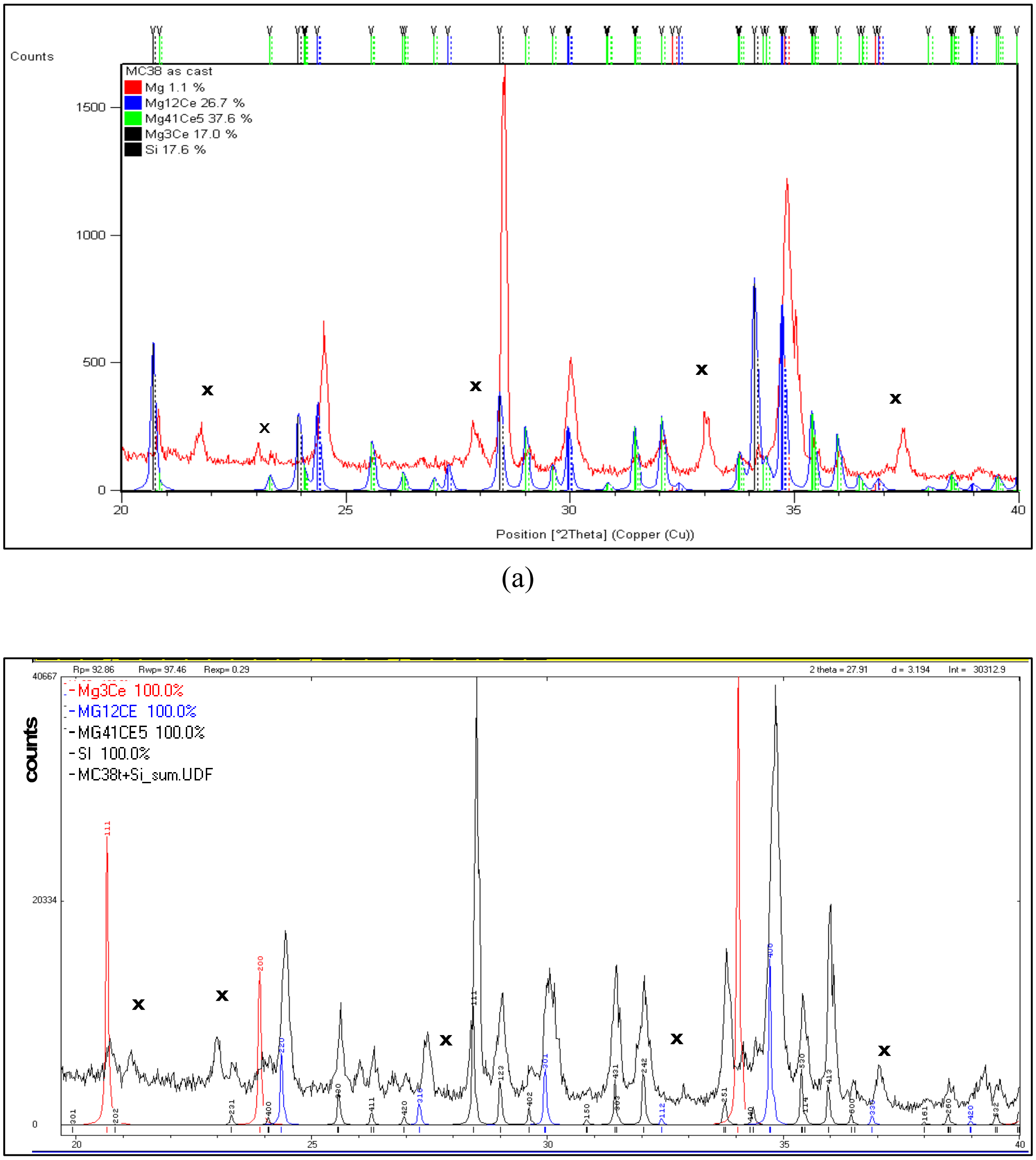

(a)

(b)

*Fig. 4.19 XRD of Alloy B (a) as-synthesized, (b) annealed at 580$^{o}$C with the indices of $Mg_3Ce$, $Mg_{12}Ce$, $Mg_{41}Ce_5$, and Si.*

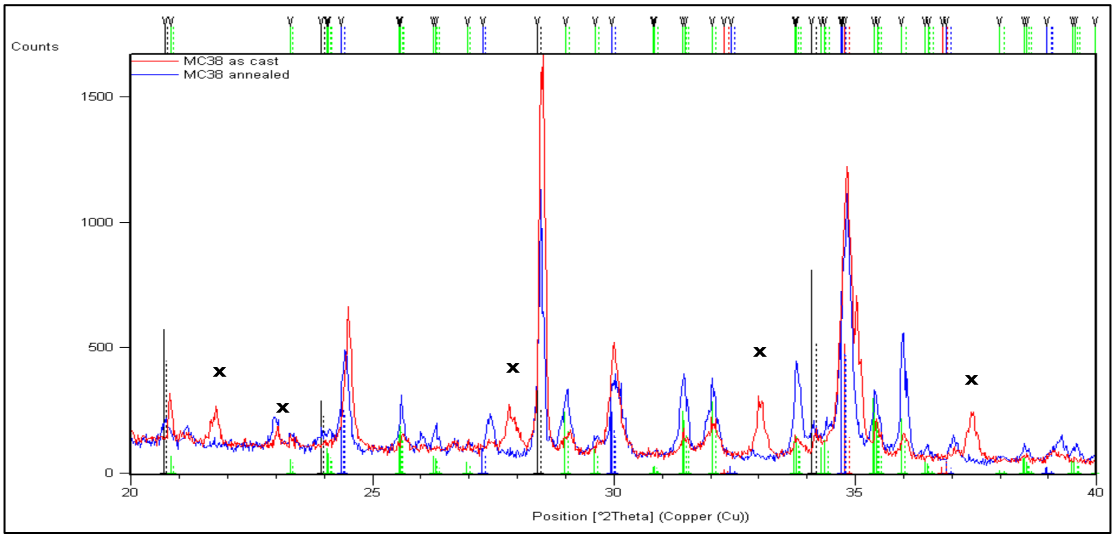

(c)

*Fig. 4.19 (Continued) (c) The comparison of the spectra of the "unknown" phase in (a) and (b). "x" denotes the peaks associated with the unknown compound.*

From the results discussed above, it is inferred that the $Mg_{3.6}Ce$ phase, which was observed in both Alloy C and B, does indeed have the $Mg_3Ce$ structure and is probably a vacancy-defect structure of the ordered $Mg_3Ce$ phase where certain Ce positions are occupied by vacancies. Such a structure may reduce the lattice strain produced by the larger Ce atoms in $Mg_3Ce$ structure and hence be more stable than $Mg_3Ce$ composition. The EPMA results indicate that there was trace level of O in the phase but this level is not specific this phase hence the effect of O in the existence of this phase is not considered significant.

The other phase is a new phase with unknown structure but has the composition of $Mg_{3.0}$-$_{3..3}Ce$. These results indicate that there are two phases with approximately $Mg_3Ce$ composition but different structures. An attempt was made to determine the crystal structure of the unknown phase with the composition of $Mg_{3.0}$-$_{3.3}Ce$, but the low intensity of the peaks and their overlap with the peaks of other phases do not allow one to determine the unique unit cell. Seven peaks which, with high probability, belong to the unknown phase were selected for indexation routine. They are shown in Table 4.11. Five measurements were taken to determine the 2-theta value of each peak. Since the values were very close, the experimental errors appear to be identical. These peaks were indexed using the DICVOL software package. The indexing procedure returned three orthorhombic unit cells that contain all seven peaks. The indexing results are shown in the Table 4.12. The selection of the unique unit cell requires a sample with higher intensity of this phase.

Table 4.11 Seven peaks selected to determine the crystal structure of the unknown phase

| EXPERIMENTAL 2-THETA | EXPERIMENTAL ERROR |
|---|---|
| 21.74 | 0.03 |
| 27.86 | 0.03 |
| 33.04 | 0.03 |
| 37.44 | 0.03 |
| 45.20 | 0.03 |
| 48.68 | 0.03 |
| 52.55 | 0.03 |

Table 4.12 Three possible orthorhombic unit cells generated using DICVOL software

| | ***a*** (Å) | ***b*** (Å) | ***c*** (Å) | Volume(Å$^3$) |
|---|---|---|---|---|
| Orthorhombic #1 | 7.721 (0.006) | 7.446 (0.011) | 6.284 (0.009) | 361.27 |
| Orthorhombic #2 | 8.926 (0.005) | 7.741(0.012) | 5.691 (0.005) | 393.18 |
| Orthorhombic #3 | 9.600 (0.007) | 7.727(0.008) | 2.711 (0.003) | 201.12 |

### 4.3.4 Discussion

$Mg_4Ce$ Phase

The alloy system exhibits two structures associated with the $Mg_3Ce$ crystal structure: $Mg_{3.0\text{-}3.2}Ce$ and $Mg_{3.6\text{-}3.7}Ce$. The latter phase can be designated as the $Mg_4Ce$ phase which is probably a vacancy defect structure of the $Mg_3Ce$ structure [5, 11]. The existence of $Mg_{3.6}Ce$ in both the as-cast and annealed conditions from both Alloy B and Alloy C compositions indicates that this is a distinct and possibly a stable phase. As the Mg composition deviates towards pure Mg, the structure probably takes on vacancies to the Ce positions to maintain the e/a ratio for structural stability. Previous researchers [8,12,13] have postulated the existence of $Mg_4Ce$ phase but no evidence had been found. It should be noted that $Mg_2Ce$ which is a high-temperature phase persists in the microstructure even after annealing below its temperature of stability. Hence, further prolonged annealing of the alloy is required before $Mg_4Ce$ can be claimed with certainty to be a stable phase.

$\mu$-$Mg_3Ce$ Phase

A phase with the $Mg_{3.0}$-$_{3.3}Ce$ composition, but to which an unknown structure could be associated, was also found in Alloy B. EPMA analysis does not indicate any distinct impurity segregation specifically into this phase (Table 4.10). Oxygen was present only in trace amount and at the same level in all phases. The attempt to index the unknown peaks pointed towards a possible orthorhombic structure. This phase is most likely a metastable phase; it exists in the as-solidified structure but disappears when annealed at the three temperatures. D03 (cF16) stable phase transformation into metastable orthorhombic oP16 phase has been observed in $Fe_3Si$ compound, where lattice-strain destabilized cF16 structure distorts into the orthorhombic lattice [14]. Hence, as the $Mg_3Ce$ phase forms as the primary phase, the rapid solidification rate results in the formation of the metastable orthorhombic form of $Mg_3Ce$ rather than the stable D03 $Mg_3Ce$.

Suggested Partial Phase Diagram

A version of the phase diagram is suggested in the composition range from 38-70wt%Ce as shown in Fig. 4.20 which includes the intermetallics $Mg_4Ce$ and $Mg_3Ce$. The μ-$Mg_3Ce$ is not included because of probable metastability. The solidification paths of the two alloys are superimposed on the suggested diagram to see if the microstructures in the as-cast state could be explained by the suggested diagram.

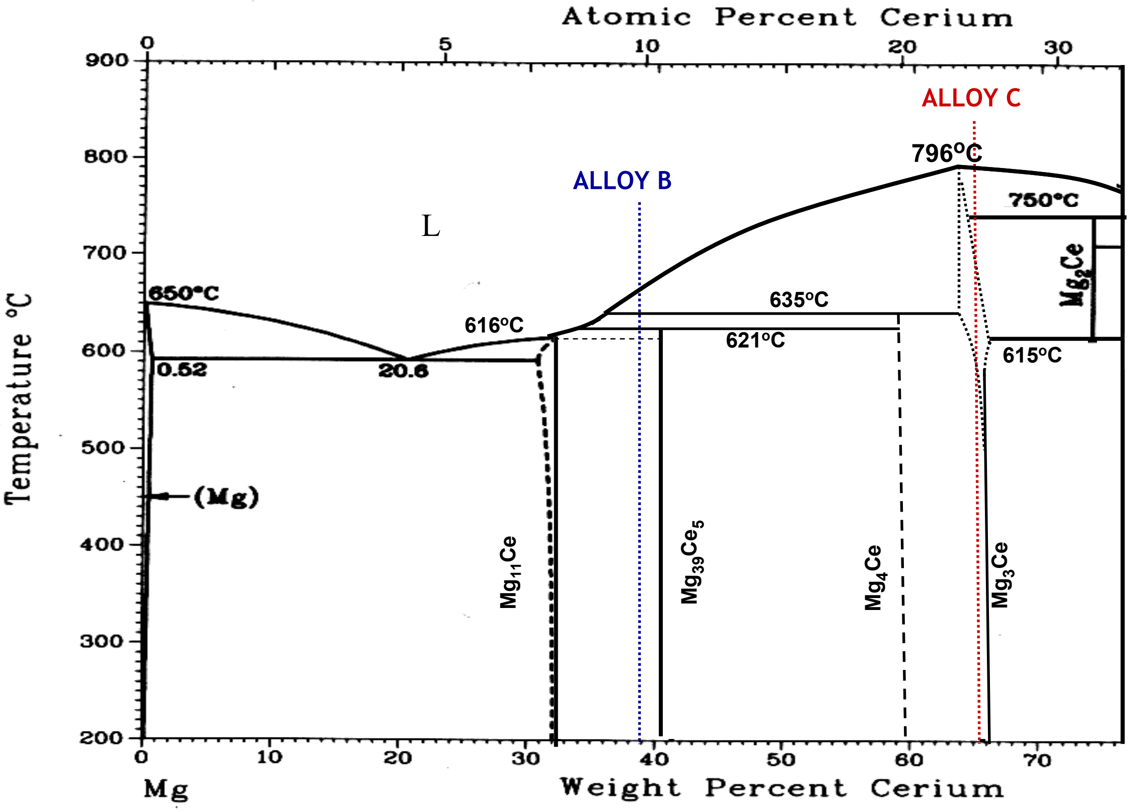

*Fig. 4.20 Suggested version of the Mg-Ce phase diagram in the 38-70wt%Ce range.*

*Alloy B*

The phases seen in the as-cast alloy (Fig. 4.18a & b) are consistent with the suggested phase diagram. The primary phase is the metastable form of $\mu$-$Mg_3Ce$. This is followed by the peritectic formation of $Mg_4Ce$, and then of $Mg_{39}Ce_5$ and then finally of $Mg_{11}Ce$. Mg phase precipitates out from the $Mg_{11}Ce$ as the alloy cools down.

It is noted that the annealing at the three temperatures has not transformed the structures to full equilibrium, because even though the $\mu$-$Mg_3Ce$ has disappeared, $Mg_4Ce$ and $\alpha$-Mg still persist in the microstructure (Fig. 4.18g & h), but their amounts are significantly reduced after the 580$^o$C anneal, approaching equilibrium of the $Mg_{11}Ce + Mg_{39}Ce_5$ as denoted by the suggested phase diagram.

*Alloy C*

This alloy is very close to the $Mg_3Ce$ composition. Solidification starts with the primary $Mg_3Ce$. Then the $Mg_2Ce$ high-temperature phase forms. This is followed by the formation of more $Mg_3Ce$ which transforms to $Mg_4Ce$+$Mg_3Ce$. The annealing times were not sufficiently long to allow for complete equilibrium. However, the as-cast (non-equilibrium) microstructures and phases are consistent and agree well with the suggested phase diagram.

The $Mg_3Ce$ phase is designated as a line compound at temperatures below 580$^o$C since the EPMA analysis gives a narrow composition around $Mg_{3.2}Ce$ when annealed. At the higher temperatures a composition range (from 3.3-3.0) is associated with $Mg_3Ce$. The phase boundaries of the $Mg_3Ce$ phase are consistent with the formation of $Mg_2Ce$ phase in Alloy C.

In the suggested phase diagram, $Mg_4Ce$ is included as a line compound in line with the facetted morphology of the phase in the microstructures. It is noted that the suggested phase diagram with the inclusion of the $Mg_4Ce$ phase may be partially metastable, because full equilibrium was not achieved in both alloy B and C after annealing. The challenge in annealing of these alloys lies in selective evaporation of Mg which would affect phase analysis. In order to avoid selective evaporation, shorter times at higher temperatures or lower temperatures were adopted and annealing was stopped before any black stains occurred on the quartz tubes in which the samples were sealed. Much longer times at low temperatures need to be adopted to attain full equilibrium and to assess any possible metastability of $Mg_4Ce$. Phase transformation temperatures were assigned from the existing phase diagram of Fig.4.15. A summary of the compounds investigated in the present study is given in Table 4.13.

Table 4.13 Mg-Ce compounds in the range 0-33at %Ce*

| Formula | Composition at% Ce | Pearson Symbol/ Prototype | Lattice Parameters, nm | Comments |
|---|---|---|---|---|
| $Mg_{12}Ce$ | ~9.4 | tI26 / $Mn_{12}Th$ | a=1.033 c=0.5964 | Temperature range <616°C |
| $Mg_{11}Ce$ [3] | 8.1-8.5 | tI26 / $Mn_{12}Th$ | Same as $Mg_{12}Ce$ | Zhang et al [3] |
| $Mg_{41}Ce_5$ | ~10.5 | tI92 | a=1.478, c=1.043 | Temperature range <635°C |
| $Mg_{39}Ce_5$ [3] ** | 11.3 | tI92 | Same as $Mg_{41}$Ce5 | Temperature range <621°C Vacancy defect structure of $Mg_{41}Ce_5$. [3] ** |
| $Mg_4Ce$** | 21.7 | cF16 / BiF3 | Same as $Mg_3Ce$ | Temperature range <635°C Vacancy defect structure of $Mg_3Ce$ ** |
| $Mg_3Ce$ | 25.0 | cF16 / BiF3 | a= 0.7428 or a=0.7424 | Temperature range <796°C |
| $Mg_3Ce$** | 24.0-25.0 | cF16 / BiF3 | Same as $Mg_3Ce$ | Temperature range <796°C |
| μ-Mg3Ce** | 23.8-25.0 | Orthorhombic | (see Table 4) ** | Likely metastable ** |
| $Mg_2Ce$ | 33.3 | cF24 / $Cu_2Mg$ | a=0.8733 | Temperature range 615-750°C |

* Data are from [15] except where indicated otherwise. **This study.

### 4.3.5 Conclusions

1. Present study on the binary Mg-Ce alloys demonstrated the existence of two distinct intermetallic phases, $Mg_4Ce$ and $Mg_3Ce$.

2. XRD indicates that $Mg_4Ce$ and $Mg_3Ce$ both have the $Mg_3Ce$ structure; $Mg_4Ce$ may be a defect-vacancy structure of $Mg_3Ce$.

3. EPMA showed that $Mg_4Ce$ has the $Mg_{3.6\text{-}3.7}Ce$ composition.

4. The μ-$Mg_3Ce$, with the $Mg_{3.0}$-$_{3..3}Ce$ composition and possibly an orthorhombic structure, was identified, which is likely a metastable form of $Mg_3Ce$.

5. Based on these results, a version of the phase diagram is suggested for the Mg-Ce system in the composition range of 38-70wt%Ce which correlates well with the as-cast structures of the two alloys studied.

### 4.3.6 References

1. M. O. Pekguleryuz, and A. A. Kaya, Creep Resistant Magnesium Alloys for Powertrain Applications, Adv. Eng. Mat., Vol. 5, No. 12, 2003.

2. T. B. Massalski, Chief Editor, Binary Alloy Phase Diagrams, *2nd ed.,* Materials Park, Ohio: ASM International, 1990.

3. X. Zhang, D. Kevorkov, M. Pekguleryuz, Stoichiometry study on the binary compounds in the Mg–Ce system—Part I, J. Alloys Compd. 475 (2009) 361-367

4. D. W. Zhou, P. Peng, and J. S. Liu, Electronic Structure and Stability of Mg-Ce Intermetallic Compounds from First-Principle Calculations, J. Alloys Compounds, 428 (2007) 316-328.

5. P. Villars and L.D. Calvert, Pearson's Handbook of Crystallographic Data for Intermetallic Phases, 2nd ed., Materials Park, OH: ASM International, 1991.

6. R. A. Varin, Intermetallics: Crystal Structures, Encylopedia of Materials: Science and Technology, Elsevier Science Ltd (2000) p. 2.

7. R. Vogel, Z. Anorg. Chem., (1915), 91, p. 277.

8. R. Vogel and T. Heumann, The systems cerium magnesium and lanthanum-magnesium, Metallforschung 1947 2 1-8.

9. G. V. Raynor, The Physical Metallurgy of Magnesium and its Alloys, Pergamon press, 1959, p. 210-12, 369-71

10. E. Zintl and E. Hesemann, Metals and alloys. XII. Binding type and lattice structure of magnesium compounds. Z. Phys. Chem. (1933) B 21 138-55.

11. F. Laves and H. Witte, Crystal structure of $MgNi_2$ and its relation to the types $MgCu_2$ and $MgZn_2$, Metallwirtschaft (1935) 14 645-9

12. J. V. Florio, N. C. Baenziger and R. E. Rundle, Compounds of Thorium with Transition Metals. II. System with Iron, Cobalt and Nickel, Acta Cryst. (1956), 9, 367

13. Q. Johnson and G. S. Smith, The Crystal Structure of $Ce_5Mg_{42}$, Acta Cryst. (1967) 22, 360.

14. M. Mihalkovic, M. Widom, Ab Initio Calculations of Cohesive Energies of Fe-based glass-Forming Alloys, Phys. Rev., Vol. B 70, 2004, p.1-12.

15. L.L. Rokhlin, Magnesium Alloys Containing Rare-Earth Metals, Structure and Properties, Taylor and Francis, N.Y., 2003.

## 4.4 Study on the Intermetallic Phases in the Mg-Ce System, Part II: Diffusion Couple Investigation*

(*This section will be submitted to Journal of Alloys and Compounds)

Mg-Ce diffusion couple annealed at 400$^{o}$C was investigated via electron probe microanalysis (EPMA), and scanning electron microscopy/energy dispersive spectroscopy (SEM/EDS). The results validated the compositions of the intermetallic phases experimentally determined by Zhang et al [1] on the Mg-rich side of the binary phase diagram and refined the phase diagram suggested by Zhang et al [2] for the composition range of 38-70wt%Ce. A revised equilibrium phase diagram was proposed for the Mg-Ce system up to 50at%Ce.

### 4.4.1 Introduction

Magnesium alloys containing rare earth (RE) elements have attracted considerable interest from the transport industry due to the demand for high strength, light-weight materials at room and elevated temperatures [3-5]. In most commercial magnesium alloys, RE elements are added as mischmetal (Mm) or didymium, where Mm is a natural mixture of 50% cerium with the reminder being mainly lanthanum and neodymium. The different effects of individual RE metals on the properties of Mg has been demonstrated in several studies [6, 7]. This may be explained by the different solubilities of RE elements in Mg, as well as the compounds formed in each Mg-RE metal system [8].

The Mg-Ce phase diagram [8] exhibits six intermetallic compounds that are formed from the liquid by peritectic reactions, except for $Mg_3Ce$ that melts congruently (Fig. 4.21). As discussed by Rokhlin [9], uncertainty exists in the region of the three intermetallics, $Mg_{12}Ce$, $Mg_{10.3}Ce$ and $Mg_{41}Ce_5$. When Vogel studied the system, the $Mg_9Ce$ phase was postulated for this region due to the similarity between magnesium-cerium and the magnesium-lanthanum diagrams [2, 10], until Wood and

Cramer [11] determined three compounds that formed peritectically ($Mg_{12}Ce$, $Mg_{17}Ce_2$, $Mg_{8.25}Ce$) in this composition region.

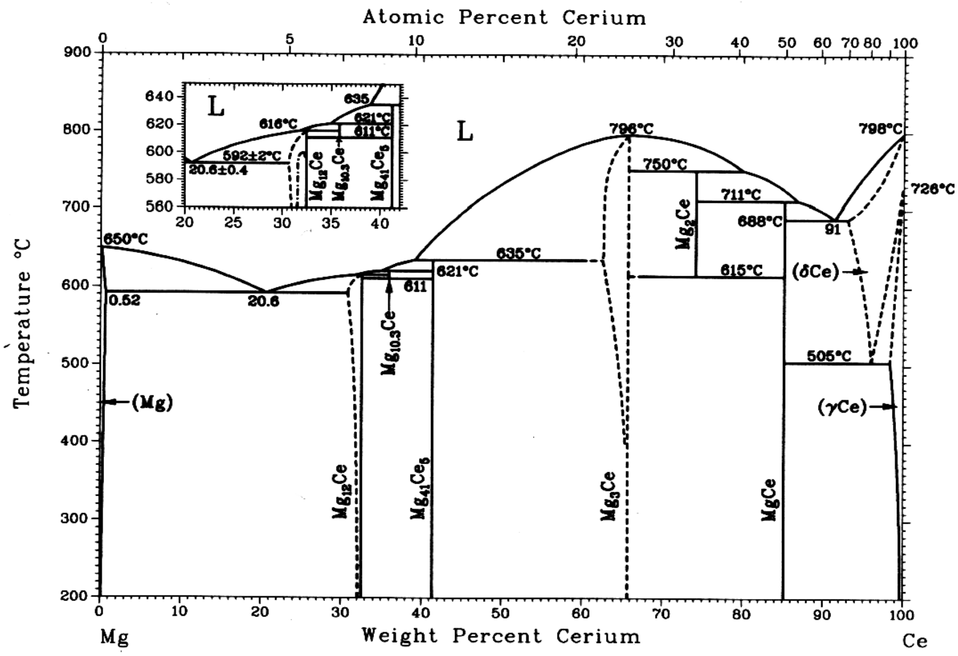

*Fig. 4.21 Mg-Ce phase diagram [8].*

Analysis of lattice parameters of $Mg_{17}Ce_2$ [9] demonstrated that the compound could be Mg-enriched and not have the stoichiometric composition of $Mg_{17}Ce_2$. It was described by the formula $Mg_{10.3}Ce$ which is still not convincing since there was no accompanying metallography or XRD study as discussed by Rokhlin [9], who investigated the $Mg_{12}Ce$ composition range and based on the fact that the $Mg_{12}Ce$ is considerably enriched in Ce (up to $Mg_{9.6}Ce$) concluded that the formula $Mg_{10.3}Ce$ cannot be assigned to the next compound [9, p. 27]. Thermal analysis investigation of this region more recently [12] has revealed thermal arrests for the 9-10at%Ce region in the 610-623$^{o}$C interval, but the authors used the $Mg_{10.3}Ce$ designation without presenting the specific EPMA results for the compound. The present authors determined [1], based on XRD and EPMA analyses, that $Mg_{12}Ce$ was enriched in Ce and re-designated it as $Mg_{11}Ce$ and the $Mg_{10.3}Ce$ compound was also eliminated from the suggested phase diagram [1] until further study.

The compound initially assumed to be $Mg_{8.25}Ce$, was subsequently assigned the formula $Mg_{42}Ce_5$ based on the crystal structure, which was later replaced with $Mg_{41}Ce_5$. The present authors have re-designated the $Mg_{41}Ce_5$ phase as $Mg_{39}Ce_5$ in their previous study [1]. The $Mg_{11}Ce$ and $Mg_{39}Ce_5$ were considered to be vacancy defect structures of $Mg_{12}Ce$ and $Mg_{41}Ce_5$, respectively, where certain Mg sites may be occupied by vacancies to keep the e/a ratio per unit cell and maintain compound stability [13].

The binary compounds $Mg_3Ce$, $Mg_2Ce$ and MgCe are considered to be well established [9]. The compounds that are rich in Ce are currently being investigated for magnetic, electronic, hydrogen storage and oxidation properties. $Mg_3RE$ (RE: Mm, La, Nd) compounds have recently been studied for their promising hydrogen storage properties [14]. The hydride of the high-temperature Laves phase $Mg_2Ce$ was studied by E. Orgaz [15]: $CeM_2H_7$ is closely related to the $Mg_2Ce$ intermetallic and has a distorted C-15 cubic structure with interesting electronic properties with the Fermi level cutting the Ce-f band leading to possible metallic conduction. Oxidation studies on the CeMg intermetallic [16] showed that negligible oxidation is observed at room temperature. The only experimental investigations of the phase diagram conducted in this region until recently have been the 1915 [17] and 1947 [18] studies of Vogel; the results were striking different and both considered rather doubtful because the cerium that was used contained 6.5% impurities. The latter work was assumed to be more correct is still used as the existing phase diagram [8] of the Mg-Ce system. The $Mg_3Ce$ region of the phase diagram seems to have been assessed largely based on the expected similarity of the Mg-Ce system to the Mg-La system [10]. A possible composition range at elevated temperature was postulated for $Mg_3Ce$ which needs further study. Additionally, a $Mg_4Ce$ phase with unknown composition is also mentioned by Raynor [10].

The composition range in the 38-70wt% has been recently studied by Zhang et al [2] via EPMA and XRD on Mg-38wt%Ce and Mg-66wt%Ce alloys. A metastable $\mu$-$Mg_3Ce$ phase, with the $Mg_{3.0}$-$_{3.3}Ce$ composition and a possible orthorhombic structure was discovered. The $Mg_4Ce$ phase with the $Mg_{3.6\text{-}3.7}Ce$ which was considered to be the vacancy defect structure of $Mg_3Ce$ was also observed. Based on the possible metastability of this phase, it was shown with a dotted line in the suggested phase diagram [2].

In order to validate the suggested phase diagrams of [1&2], a diffusion couple investigation has been carried out. This paper reports on the results of the diffusion couple and proposes a revised Mg-Ce phase diagram up to 50at%Ce.

### 4.4.2 Experimental Procedure

*Preparation of the Diffusion Couple*

A solid-liquid contact method was employed to make the Mg-Ce diffusion couple. High purity starting materials were used (Table 4.14): Mg ingot (99.96%) was supplied by Timminco Metals, Haley, Ontario, Canada, and Ce (99.7%) bulk was supplied by (Hefa Rare Earths Canada Co. Ltd., Richmond, BC, Canada). Analysis by Inductively coupled plasma (ICP) at Genitest Labs (Montreal) gave ~0.37wt% impurities in cerium and 0.02wt% impurities in magnesium. Fast Neutron Activation Analysis (FNAA) at Texas A&M University was used to detect the oxygen content more precisely especially during manipulation in the lab: oxygen levels determined in pure cerium samples that have been exposed to cutting and handling for 30 minutes were measured to be ~0.7wt%. This was mainly due to the formation of an oxide scale on the surface.

Table 4.14 Impurities in Cerium (ppm)*

| ***Impurities in Ce*** | | | | | | | | | | | | | | | |
|---|---|---|---|---|---|---|---|---|---|---|---|---|---|---|---|
| **Rare Earth Elements** | **La** | **Pr** | **Nd** | **Sm** | **Eu** | **Gd** | **Tb** | **Dy** | **Ho** | **Er** | **Tm** | **Lu** | **Y** | **Ce** | **Total impurities** |
| | 320 | 150 | 430 | 10 | 2 | 5 | 2 | 5 | 1 | 1 | 1 | 1 | 10 | **Bal** | |
| **Others** | **Si** | **Fe** | **C** | **Ni** | **Al** | **Mg** | **O*** | **Ca** | **Ta** | **Mo** | **Mn** | **W** | **N** | **-** | 3738 ppm |
| | 180 | 1050 | 450 | 50 | 420 | 50 | 115 | 50 | 50 | 210 | 25 | 100 | 50 | - | |

| ***Impurities in Mg*** | | | | | | | | | | | | | |
|---|---|---|---|---|---|---|---|---|---|---|---|---|---|
| **Si** | **Fe** | **Zn** | **Ni** | **Al** | **Cu** | **Mn** | **Ca** | **O*** | **Pb** | **Sn** | **Cd** | **Mg** | **Total Impurities** |
| 30 | 22 | 40 | 3 | 40 | 2 | 21 | 10 | - | 10 | 10 | 10 | **Bal.** | 198 ppm |

* re-verified via FNA

A rectangular piece of cerium was polished with 320-grit SiC paper under paraffin oil, and then cleaned with acetone to ensure an oxide free surface. Pure magnesium was melted under a protective atmosphere of $CO_2$+0.5%$SF_6$. The melt was then taken from the furnace under a cover gas of $CO_2$+0.5%$SF_6$ and cerium was immediately submerged into the molten magnesium. Due to the higher thermal expansion coefficient of magnesium ($26.0\times10^{-6}$ $K^{-1}$) compared to that of cerium ($8.0\times10^{-6}$ $K^{-1}$), an intimate contact between magnesium and cerium formed during solidification. The sample was then sectioned and encapsulated in a vacuum quartz tube shown in Fig. 4.22. A titanium sponge getter was used in case any gas evaporation occurred at high temperature. The quartz tube was placed in a Blue-M mechanical convection furnace, heat treated at 400°C for 14 days, and then quenched in cold air which shattered the quartz tube and rapidly cooled the diffusion couple.

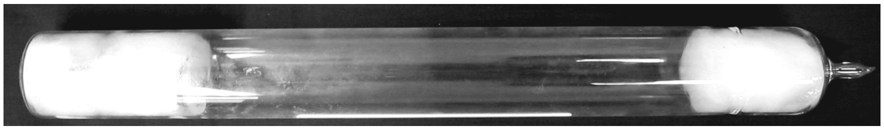

*Fig. 4.22 The Mg-Ce diffusion couple encapsulated in quartz tube.*

*Material Characterization*

The diffusion couple was polished by conventional metallographic technique using diamond paste with oil-based extender and studied via JEOL840 scanning electron microscopy/energy dispersive spectroscopy (SEM/EDS). Phase identification was further carried out via electron probe microanalysis (EPMA) using a JXA8900L equipped with wavelength-dispersive spectroscopy (WDS) for quantitative analysis.

### 4.4.3 Results and Discussion

SEM image (Fig. 4.23) shows the different zones formed in the diffusion couple at 400$^o$C. Five regions are visible from the pure Mg on the left to pure Ce on the right. The thickness of the layers varies from 200µm to 5µm owing to the different diffusion coefficients of Mg and Ce atoms.

EPMA indicated that four intermetallic zones formed: $Mg_{11}Ce$, $Mg_{39}Ce_5$, $Mg_3Ce$, and MgCe. The formation of the eutectic $Mg_{11}Ce$+Mg zone on the right is due to the solid-liquid method of making the diffusion couple: when the cerium was immersed in molten magnesium, some Ce dissolved, and the eutectic formed on its surface. The columnar $Mg_{11}Ce$ may have formed from the eutectic instead of from the pure Mg, making the shape different from the other three planar layers.

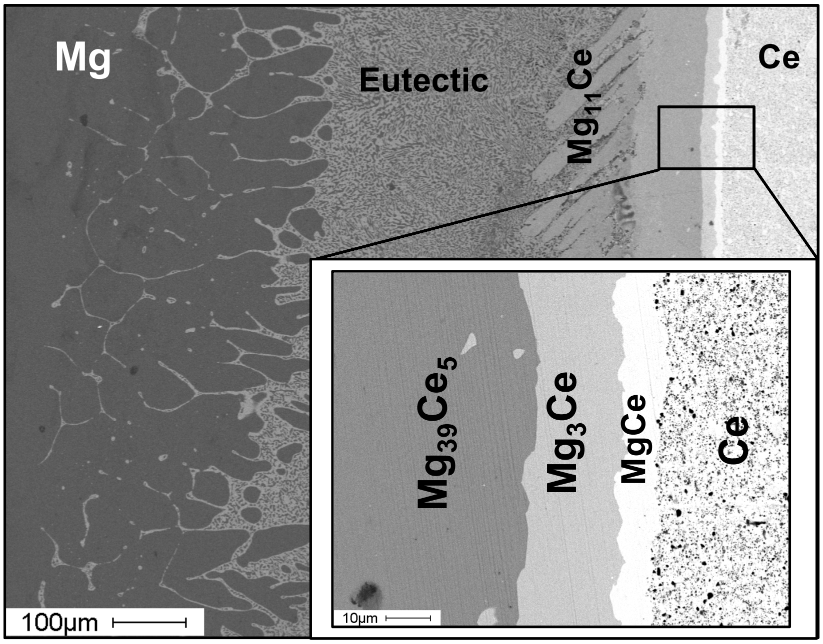

*Fig. 4.23 Diffusion layers formed between Mg and Ce at 400°C.*

The zones were quantitatively analyzed by EPMA (Table 4.15). The Mg/Ce ratio confirms the re-designation of $Mg_{12}Ce$ and $Mg_{41}Ce_5$ as $Mg_{11}Ce$ and $Mg_{39}Ce_5$, respectively [1, 2]. EPMA indicated an oxygen level of 1-3at% (increasing towards the Ce side). This does not correlate with the deviation of the measured Mg/Ce ratio of the intermetallics from the theoretical formulae, which is the highest for $Mg_{11}Ce$ and the lowest for $Mg_3Ce$.

Table 4.15 EPMA Results of the Interdiffusion Zones in the Mg-Ce Diffusion Couple

| | Mg (at%) | Ce (at%) | Mg/Ce Ratio (std. dev) | Mg/Ce theoretical |
|---|---|---|---|---|
| $Mg_{11}Ce$ | 90.10 | 8.36 | 10.78 (0.18) | 12 |
| $Mg_{39}Ce_5$ | 87.56 | 11.39 | 7.69 (0.05) | 8.2 |
| $Mg_3Ce$ | 73.24 | 24.68 | 2.97 (0.03) | 3 |
| MgCe | 46.57 | 48.88 | 0.95 (0.01) | 1 |

In order to study the solid solution range of the $Mg_{11}Ce$ at 400$^oC$, SEM line scans were obtained (Fig. 4.24). Although the Mg and Ce counts fluctuate, the tendency for an increase in cerium and decrease in magnesium can be noted confirming the results obtained previously by Zhang et al [1]. All other phases, $Mg_{39}Ce_5$, $Mg_3Ce$ and MgCe exhibit near constant Mg/Ce ratio in the interdiffusion zones indicating that these compounds are stoichiometric. The diffusion couple study at 400$^oC$ also shows that the $Mg_4Ce$ phase discovered in the previous study [2] is metastable since it does not form the equilibrium conditions at this temperature. This study allows the authors to propose a revised binary phase diagram for the Mg-Ce system up to 50at%Ce (Fig. 4.25). The revised version differs from the existing phase diagram mainly in the Mg-rich side. The $Mg_{11}Ce$ and $Mg_{39}Ce_5$ replace $Mg_{12}Ce$ and $Mg_{41}Ce_5$ as stable and possibly vacancy defect structures. The $Mg_{10.3}Ce$ phase is removed because of the difficulty in the previous studies related to understanding this high temperature phase, first as $Mg_{17}Ce_2$ then as a Mg-enriched and non-stoichiometric $Mg_{10.3}Ce$ phase. In fact, Johnson et al [19] were not certain of the exact composition of the $Mg_{10.3}Ce$ ($Th_2Ni_{17}$-type) phase; the formula deduced from a single-crystal structure determination was not considered to accurately reflect the composition of the bulk material. Further study is needed to clarify this region of the phase diagram at high temperature. The boundaries of the $Mg_3Ce$ phase above 530$^oC$ are shown as dotted lines in Fig. 4.25 based on [2].

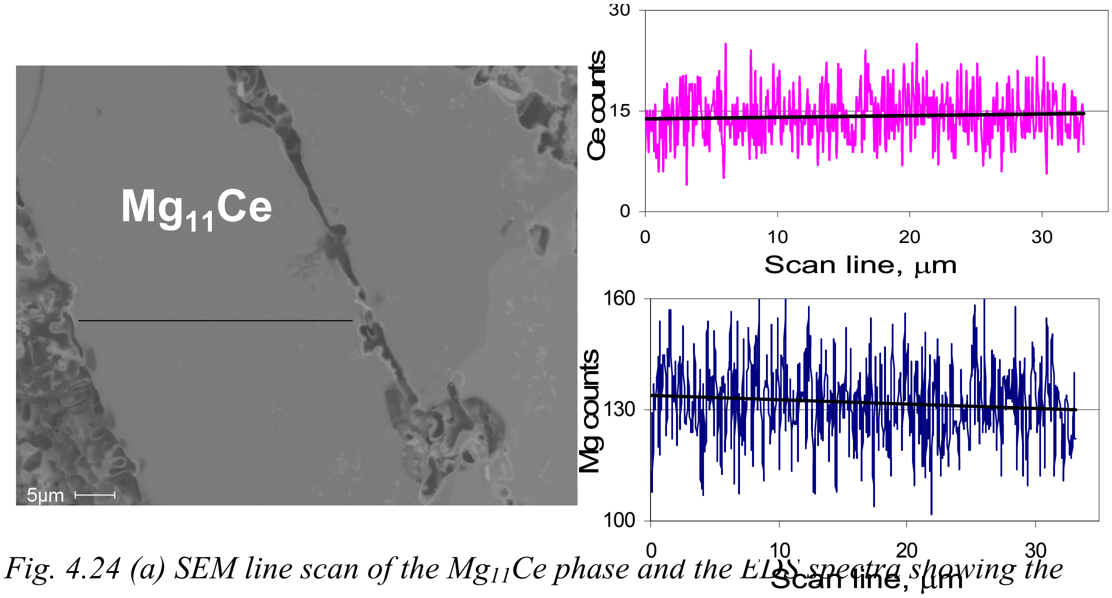

*Fig. 4.24 (a) SEM line scan of the* $Mg_{11}Ce$ *phase and the EDS spectra showing the compositional variation in (b) Ce and (c) Mg.*

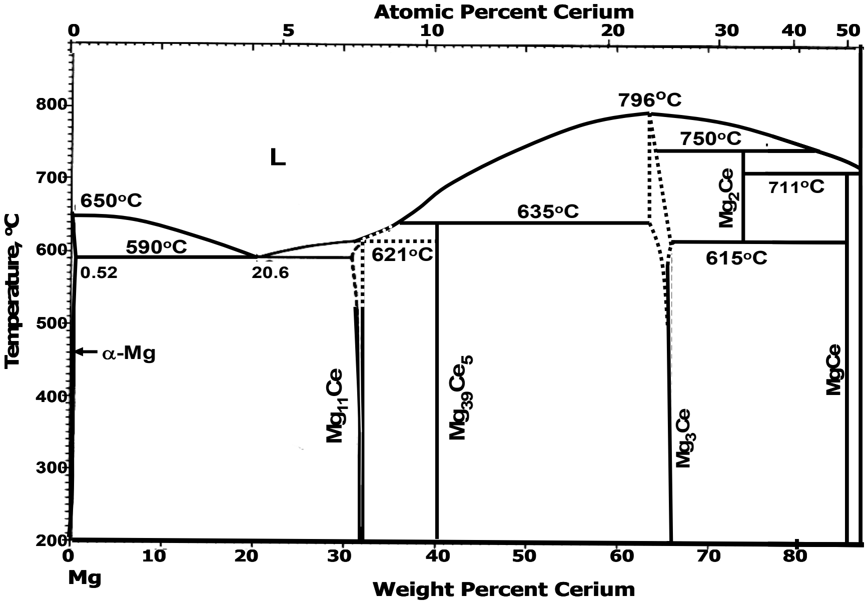

*Fig. 4.25 Revised Mg-Ce phase diagram up to 50at%Ce.*

Table 4.16 gives a summary of the stable and metastable phases in Mg-Ce system. The occurrence of the stable $Mg_{11}Ce$ as a possible vacancy defect structure is interesting for Mg alloy development; such a structure would likely form solid solution phases with other elements influencing the thermal/microstructural stability of a Mg-Ce based alloy. The existence of a metastable $Mg_4Ce$ phase with the $Mg_3Ce$ structure, which persists after long term annealing [2], is important for hydrogen storage research. The metastable $\mu$–$Mg_3Ce$ phase [2] can be explained as the phase transformation of the lattice-strained D03 (cF16) stable $Mg_3Ce$ phase into metastable orthorhombic oP16 phase. Such transformation has been observed in the D03 (cF16) $Fe_3Si$ compound [19]. Future work on the system needs to be conducted (i) to address the controversy around the high temperature $Mg_{10.3}Ce$ ($Mg_{17}Ce_2$) phase as well as (ii) in the high temperature region between 20-30at% Ce to confirm the phase boundaries of $Mg_3Ce$ above 400°C.

Table 4.16 Mg-Ce Compounds in the 0-50at % Cerium Range [9, 1, 2]

| Formula | Composition at%Ce | Pearson Symbol/ Prototype | Lattice Parameters, nm | Comments |
|---|---|---|---|---|
| *Stable phases* | | | | |
| $Mg_{11}Ce$ [1]* | 8.1-8.5* | tI26 / $Mn_{12}Th$ | a= 1.033, c=0.5964 | Zhang et al [1] |
| $Mg_{39}Ce_5$ [2]* | 11.3-11.4* | tI92 | a= 1.454, c=1.028<br>a=1.478, c=1.043 | Temperature range <621°C<br>Vacancy defect structure of $Mg_{41}Ce_5$ [2] |
| $Mg_3Ce$ [9] | 25.0 | cF16 / BiF3 | a= 0.7428 or a=0.7424 | Temperature range <796°C |
| $Mg_3Ce$ [9, 2]* | 24.0-25.0* | cF16 / BiF3 | Same as $Mg_3Ce$ | Temperature range <796°C |
| $Mg_2Ce$ [9] | 33.3 | cF24 / $Cu_2Mg$ | a=0.8733 | Temperature range 615-750°C |
| MgCe* | 48.9* | cP2 / CsCl | a=0.3898, a=0.3912 | Temperature range < 715°C |
| *Metastable phases* | | | | |

| | | | | |
|---|---|---|---|---|
| $Mg_{3.6}Ce$ [2] | 21.7* | cF16 / BiF3 | Same as $Mg_3Ce$ | Temperature range<br>$<635^{o}$C<br>Vacancy defect structure of $Mg_3Ce$.<br>*Metastable** |
| $\mu$-$Mg_3Ce$ [2] | 23.8-25.0* | Orthorhombic [2] | [Ref. 2] | *Metastable* |
| *To be confirmed* | | | | |
| $Mg_{17}Ce_2$ ? | ~10.3 | hP38 / $Ni_{17}Th_2$ | [Ref. 9] | [Ref. 9] |

*This study.

### 4.4.4 References

1. X. Zhang, D. Kevorkov, M. Pekguleryuz, “Stoichiometry Study on the Binary Compounds in the Mg-Ce System-Part I”, J. Alloys Compounds, vol. 475, issues 1&2, 2009, pp. 361-367.
2. X. Zhang, D. Kevorkov, M. Pekguleryuz, “Study on the Binary Intermetallic Compounds in the Mg-Ce System,” Intermetallics, vol. 17, no. 7, 2009, pp. 496-503.
3. M.O. Pekguleryuz, A.A. Kaya, “Creep Resistant Magnesium Alloys for Powertrain Applications," Adv. Eng. Mater., DGM, vol.5, No.12, 2003, pp. 866-878.
4. A. Luo, M.O. Pekguleryuz, "Cast Magnesium Alloys for Elevated Temperature Applications - A Review," J. Mater. Sci., vol. 29, 1994, pp. 313-319.
5. A. Luo, J. Int. Mat. Rev, vol. 49 no.1, 2004, pp.13-30.
6. K. H. J. Buschow, “Magnetic Properties of Rare Earth-Magnesium Compounds ($RMg_3$),” J. Less-common Met., 44 (1976), 301
7. R. Ferro, S. Delfino, G. Borzone, A. Saccone, and G. Cacciamani, “Contribution to the Evaluation of Rare Earth Alloy System,” J. Phase Equilibria, 14(3) (1993)
8. T. B. Massalski, Chief Editor, Binary Alloy Phase Diagrams, 2nd ed. (Materials Park, Ohio: ASM International, 1990)

9. L. L. Rokhlin, Magnesium Alloys Containing Rare Earth Metals: Structure and Properties, (Taylor & Francis, 2003)
10. G. V. Raynor, The Physical Metalurgy of Magnesium and its Alloys, (Pergamon press Ltd., 1959)
11. D. H. Wood and E. M. Cramer, “Phase relations in the magnesium-rich portion of the cerium-magnesium system,” J. Less-common Met., 9 (1965) 321-337.
12. A. Saccone, D. Macciò, S. Delfino, F. Hayes, R. Ferro, J.Therm. Analys. Calor. vol. 66, no. 1, 2001, pp. 47-57.
13. R. E. Smallman, and R. J. Bishop, Modern Physical Metallurgy and Materials Engineering, 6th Edition, Butterworth-Heinemann, 1999.
14. L.Z. Ouyang, H.W. Dong, C.H. Peng, L.X.Sun, M. Zhu, “A New Type Mg-Based Metal Hydride with Promising Hydrogen Storage Properties,” Int. J. Hydrogen Energy, vol 32, 2007, pp. 3929-3035.
15. E. Orgaz, “The Electronic Structure of the Laves Phase Intermetallics $LnM_2$ (Ln=Y, La-Lu, M=Mg, Al) and $LaMg_2H_7$ and $CeMg_2H_7$ Hydrides,” J. Alloys Comps., vol. 322, 2001, pp. 45-54.
16. B. Stumpy, Y. Mudryk, A. Russell, D. herman, K. Gschneidner, Jr., “Oxidation Resistance of B2 Rare-Earth-Mg Intermetallic Compounds,” J. Alloys Comps., vol. 460, 2008, pp. 363-367.
17. R. Vogel, Z. Anorg. Chem., vol. 91, 1915, p. 277.
18. R. Vogel and T. Heumann, The systems Ce-Mg and La-Mg, Metallforschung 1947 2 1-8.
19. Q. Johnson and G. S. Smith, Acta Cryst., B26 (1970) 434-435.
20. M. Mihalkovic, M. Widom, Ab Initio Calculations of Cohesive Energies of Fe-based Glass-Forming Alloys, Phys. Rev., Vol. B 70, 2004, p.1-12.

## 4.5 Phase diagram Study on Ce-Mn and Mg-Mn Systems via Diffusion Couples

### 4.5.1 The Preparation of Ce-Mn and Mg-Mn Diffusion Couples

The Ce-Mn diffusion couple was prepared using the solid-solid technique as shown in Fig. 4.26a. A piece of Ce was clamped by two pieces of Mn from both sides. While the integrated cerium and manganese were immersed in molten magnesium, the Ce-Mn couple was held firmly while the molten magnesium solidified (Fig. 4.26b). In the mean time, the Mg-Mn couple formed when molten magnesium covers the surface of manganese.

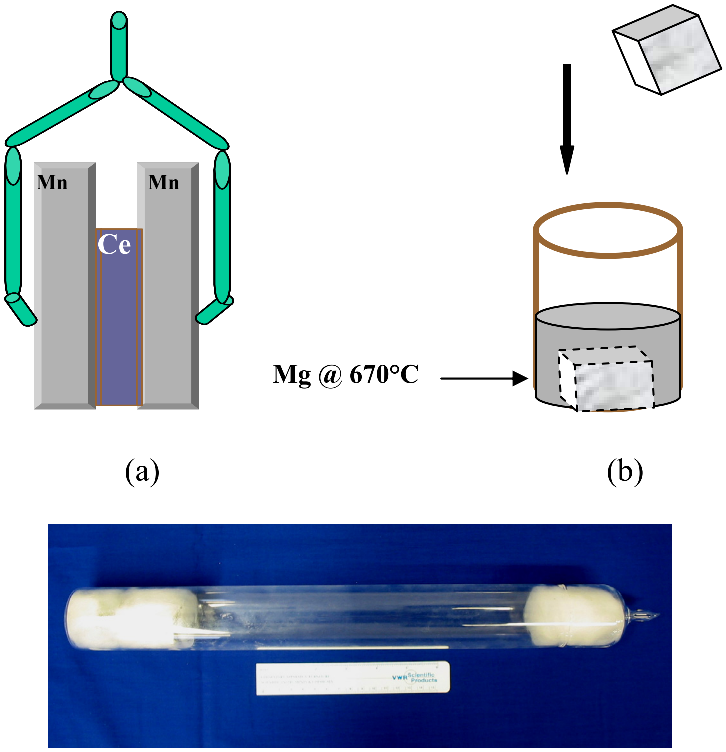

(a) (b)

(c)

*Fig. 4.26 (a) Solid-solid diffusion couple, (b) solid-liquid diffusion couple, and (c) quartz tube encapsulation of the diffusion couples.*

The couples were vacuum encapsulated in quartz tubes (Fig. 4.26c) and annealed at 400°C for 15 days, and then chilled with compressed air. The observation of the diffusion layers and phase identification were conducted via SEM/EPMA.

### 4.5.2 Characterization of the Diffusion Couples

Both the Mg-Mn and the Ce-Mn diffusion couples were successfully prepared using this technique, and the annealing process caused no oxidation of the samples. Fig. 4.27a is the image of Mg-Mn couple showing intimate contact at the interface. Unlike the Mg-Ce couple that formed several interdiffusion layers, the Mg-Mn couple showed no apparent diffusion zones.

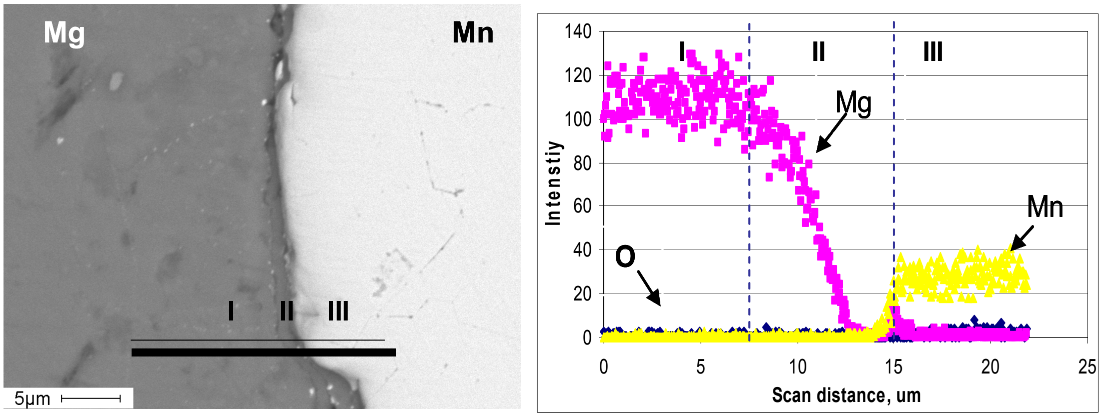

(a) (b)

*Fig. 4.27 Diffusion couple Mg-Mn indicates (a) interface and (b) line scan at the interface.*

However, when a line scan was conducted across the interface (the black line showed in Fig. 4.27a), three regions can be distinguished as shown in Fig. 4.27b. Three scanned lines from top to bottom represent magnesium, manganese and background level oxygen, respectively. Region I and III are pure Mg and Mn. Region II shows a decline of Mg and an increase of Mn. The co-existence of the two elements indicates a solid solution layer(s). It could be the single layer of Mn dissolved in Mg or two solid solutions (zone I indicating Mn dissolved in Mg and zone III related to Mg dissolved in Mn). The quantitative analysis is hard to conduct due to the small scale of the diffusion layer. The sharp variation of both Mg and Mn in region II also proves that no intermetallic phase formed in the binary system.

Fig. 4.28a & b are the images of Ce-Mn diffusion couple. Line scan was conducted at the well-contacted interface (Fig. 4.28a). Unlike the Mg-Mn diffusion couple, there is a clear boundary between pure Ce and Mn (Fig. 4.28b). No mixture of the two elements or any other diffusion layers are observed between Ce and Mn. Even though the analysis is less than 10µm from the interface (in Fig. 4.28c), the distance causing change of both elements cross the interface is less than 5 µm, which is minor to be considered a solid solution.

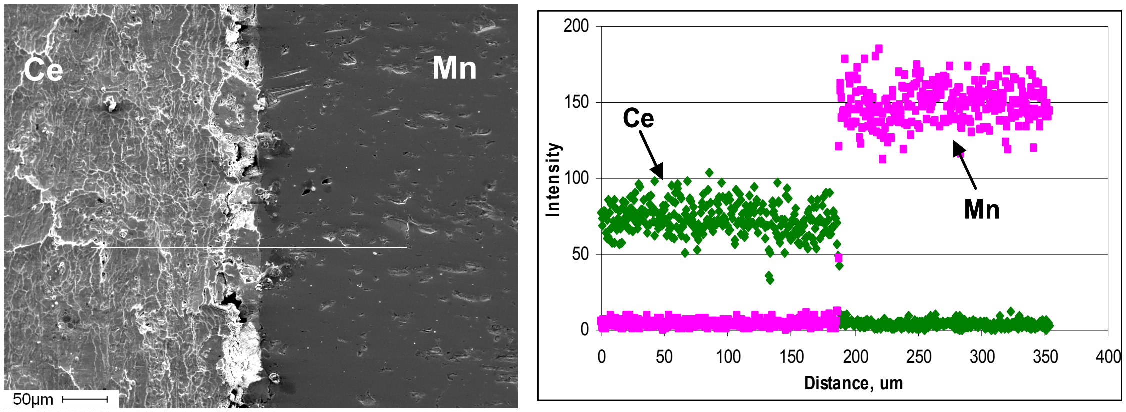

(a) (b)

*Fig. 4.28 Diffusion couple Ce-Mn indicates (a) interface, and (b) line scan at the interface*

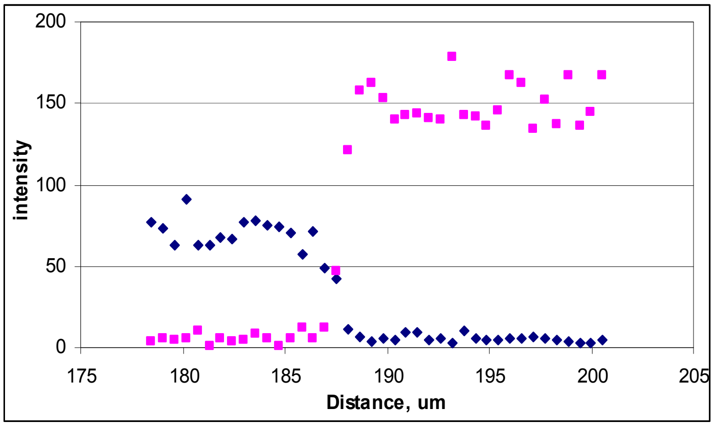

(c)

*Fig. 4.28 (Continued) (c) magnified line scan at interface showing no solid solution.*

## 4.6 Thermodynamic modeling of Ce-Mn binary system

### 4.6.1 Introduction

The Mg-Ce-Mn is an important sytem for the development of wrought alloys with improved formability due to Mn and improved strength due to Ce. The two binary systems, Mg-Mn and Mg-Ce have been assessed and optimized [1,2] However, the thermodynamic study on the Ce-Mn system is limited. As part of the objective of building a thermodynamic database, an attempt was made to model the Ce-Mn system.

### 4.6.2 Literature

The complete phase diagram of the Ce-Mn system was constructed by Iandelli [3] using thermal analyses to acquire phase transformation temperature. All the measurements were under the protection of NaCl + $BaCl_2$ melt. A further investigation was conducted by Mirgalovskaya and Strel'nikova [4] who agreed with the results of Iandelli in general except for the interpretation of the horizontal line at 998 and 1087°C, which shows allotropic transition in Mn with negligible solubilities.

Thamer [5] studied the Ce-rich part of this phase diagram by DTA and XRD. The Ce-Mn solution was assessed based on all the experimental works, but the invariant temperature and composition of Ce-rich side is from Thamer, the Mn side is from Iandelli and Mirgalovskaya and Strel'nikova.

Palenzona and Cirafici [6] summarized that none of the experimental and earlier thermodynamic prediction shows the existence of intermediate phases. The possibility of immiscibility gap was suggested by Palenzona and Cirafici based on the phase diagram of closely related lanthanide-Mn system (La-Mn). However, no experimental evidence is found for the immiscibility gap. Regarding the solid solubility, Iandelli indicated very little or no solubility of Ce in Mn by lattice parameter at room temperature, and Thamer reported less than 1 at% solubility of Mn in Ce at 600$^{o}$C. Nikolaenko et al [7] measured the partial enthalpy of mixing of liquid Ce-Mn alloys at 1600K using an isothermal calorimeter in a very pure Ar atmosphere. An expression was proposed to calculate the integral heats of mixing of this system. These measurements include a complete range of alloy composition from 0 to 1molar fraction of Mn.

### 4.6.3 Thermodynamic Models

The Gibbs energy for a pure element *i*, with certain structure *φ*, referred to the enthalpy of its standard state at 298K and 1 atm is described as function of temperature by Eq.(1) [8]:

$$G_{i}^{0,\varphi}(T) = a + bT + cT\ln(T) + dT^{2} + eT3 + fT^{-1} + gT^{7} + hT^{-9} \qquad \text{Eq.(1)}$$

Where a, b, c…are coefficients and the values are taken from the SGTE database [8].

Gibbs energy for stoichiometric phase can be expressed by:

$$G^{\varphi} = \sum x_i G_i^{0,\varphi} + \Delta G_f \qquad \text{Eq.(2)}$$

Where $\Delta G_f = a + bT + \ldots$represents the Gibbs energy of forming stoichiometric phase. Parameters a and b can be obtained by optimization.

For the disordered solution phase such as liquid or substitutional solid solution, a regular solution model is applied to describe the Gibbs energy:

$$G^{\varphi} = \sum x_i G_i^{0,\varphi} + RT\sum x_i \ln x_i + G^{E,\varphi} \qquad \text{Eq.(3)}$$

Where $x_i G_i^{0,\varphi}$ is the Gibbs energy of a pure constituent at its certain molar fraction, $RTx_i \ln x_i$ is the random mixing of the two constituents, and $G^{E,\varphi}$ is the excess Gibbs energy which accommodates non configurational entropy and the heat of mixing. The excess Gibbs energy is expressed by Redlich-Kister polynomial:

$$G^{E,\varphi} = x_1 x_2 \left(L_0 + L_1(x_1-x_2) + L_2(x_1-x_2)^2 + \ldots\right) \qquad \text{Eq.(4)}$$

Where interaction parameters $L_0$, $L_1$, and $L_2$ are temperature dependent. For the liquid, a two term Redlich-Kister polynomial was used for optimization:

$$G^{E} = x_{Ce} x_{Mn} (A+BT) \qquad \text{Eq.(5)}$$

Where $L_0 = A + BT$. A and B are the parameters to be optimized.

### 4.6.4 Optimization Results

The calculated phase diagram using the present thermodynamic model is plotted in Fig. 4.29 with the experimental data. The result of the optimized parameters are A=13611, B=-3219. The optimization shows good agreement with experimental data. However, in the calculated phase diagram (Fig. 4.29), there is a slight deviation on the Mn side between 68 and 82 at% Mn at 996°C. This might be a sign of immiscibility which has been supported by the shape of Pr-Mn phase diagram [9].

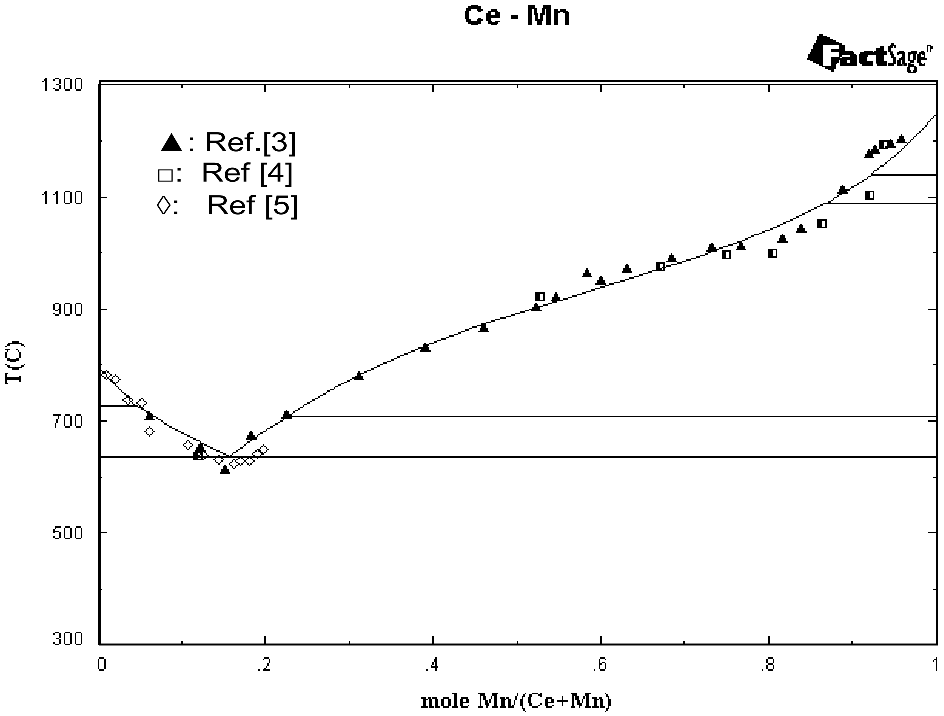

*Fig. 4.29 Calculated phase diagram compared with experimental data from literature.*

There are four allotropic forms of Mn and two for Ce, but no experimental information of solid solubility on both side of the phase diagram exists. Therefore, no solid solubility has been taken into account for the optimization. The horizontal lines above the eutectic temperature only represent the allotropic transitions at certain temperatures.

The reproduction of the enthalpy is not as good as that of the phase diagram (Fig. 4.30). The calculated minimum enthalpy of mixing is at 50at% Ce, however, the experimental data is found around 35at% Ce. This means that the most tendency of ordering of liquid phase is occurring at about 2/1 ratio of Mn/Ce. In the case of R-K polynomial model, the ordering (minimum at enthalpy and entropy) is naturally occurring at 1/1 ratio of Mn/Ce due to the random mixing entropy term, $RT(x_a \ln x_a + x_b \ln x_b)$, will have a maximum at $0.5x_a$ and $0.5x_b$). Therefore, it is hard to use model parameters to move this minimum enthalpy due to the intrinsic weakness of the R-K model.

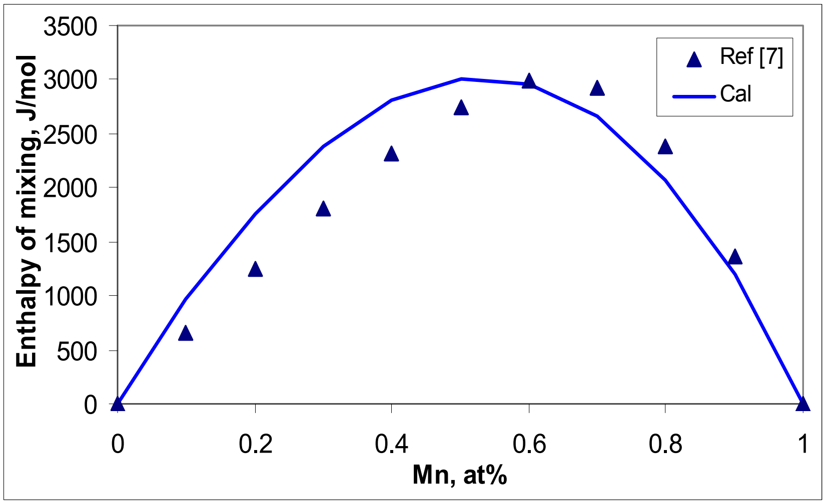

*Fig. 4.30 Calculated enthalpy of mixing at 1600K with experimental data from literature.*

Later the quasi-chemical model was applied by Kang etc [10] where it was easy to move this minimum by changing the coordination number of Mn and Ce (3 and 6 for Mn and Ce coordination numbers). The model naturally predicts a minimum at about 33% of Ce composition. This automatically reproduces the minimum of enthalpy of mixing and phase diagram simultaneously.

### 4.6.5 Conclusions

A set of thermodynamic parameters was obtained by optimization based on the available experimental results. The calculated results are in good agreement with the available experimental data. The experimental measurements on the allotropic forms of Mn, especially their solid solubilities and more experimental thermodynamic properties for this system are required to allow better thermodynamic description of the system.

### 4.6.6 References

1. G. Cacciamani, G. Borzone, and R. Ferro, System Ce-Mg. In Ansara I, Dinsdale AT, Rand MH, editors COST507-thermochemical database for light metal alloys, July 1998. European Commission EUR 18499 EN, p. 137-40
2. J. Tibballs, System Mg-Mn. In Ansara I, Dinsdale AT, Rand MH, editors COST507-thermochemical database for light metal alloys, July 1998. European Commission EUR 18499 EN.
3. A. Iandelli, the Ce-Mn Alloys, Atti. Accad. Naz. Lincei, Rend., 13, 265-268, (1952)
4. M. S. Mirgalovskaya and I. A. Strel'nikova, Investigation in the Mn-Ce System, Trudy Inst. Met. Im. A.A. Baikova, Akad. Nauk SSSR, 135-138 (1957)
5. B. J. Thamer, the System Ce-Mn in the Range of 0-20 Atomic Percent Manganese, J. Less-Common Met., 7, 341-346 (1964)
6. A. Palenzona and S. Cirafici, the Ce-Mn System, Journal of Phase Equilibria, vol. 17, No. 1, 53-56, 1996
7. I.V.Nikolaenko, V.V.Nosova, Heats of Mixing of Manganese with Lanthanum, Cerium, and Praseodymium, RASPLAVY, (1) 76-9, 1993
8. A. T. Dinsdale, SGTE Data for Pure Elements, Calphad, vol. 15, no. 4, 317-425, 1991

9. A. Saccone, S. Delfino, and R. Ferro, Alloying Behavior of Manganese with Basic Metals: Pr-Mn System, J. Less-Common Met., 108, 89-105 (1985)
10. Y.-B. Kang, A.D. Pelton, P. Chartrand, P. Spencer and C.D. Fuerst, Critical Evaluation and Thermodynamic Optimization of the Binary System in the Mg-Ce-Mn-Y System, JPEDAV (2007) 28: 342-354

# CHAPTER 5

# PHASE EQUILIBRIA STUDY ON TERNARY Mg-Mn-Ce SYSTEM

(This paper has been published: X. Zhang, D. Kevorkov, I-H. Jung, M. Pekguleryuz, "Phase Equilibria on the Ternary Mg-Mn-Ce System at Mg-Rich Corner", J. Alloys Compounds, 482 (2009), pp. 420-428)

Three isopleths at the Mg-rich corner of Mg-Mn-Ce ternary system were investigated via thermal analysis, SEM/EPMA and XRD. A ternary eutectic reaction was observed at ~ 1wt% Mn and 23wt% Ce and 592°C. A solid-solution type ternary intermetallic compound, $(Mg,Mn)_{12}Ce$, was observed with 0.5 at% solid solubility of Mn in the tetragonal $Mg_{12}Ce$. With the aid of thermodynamic modeling and experiments, a revised phase diagram for the binary Mg-Ce system and the isopleths of 0.6, 1.8 and 2.5wt% Mn were proposed up to 25wt% Ce.

## 5.1 Introduction

Magnesium-manganese-cerium (Mg-Mn-Ce) system constitutes a promising new alloy base for automotive applications. Manganese is used in magnesium alloys to lower the iron content and improve the corrosion resistance of Mg-Al alloys. It is also known that magnesium alloys containing manganese exhibit good ductility, making it possible to form sheet, extrusions and tubes [1]. The shortcoming of manganese is that it exerts little effect on the tensile properties of either cast or wrought magnesium. Cerium, on the contrary, is known to improve the strength and elevated temperature properties of magnesium alloys. Promising creep performance has been observed in Mg-Mn-Ce alloys in the past and these have been mainly used in the nuclear reactor industry [1]. It can be inferred that magnesium containing both

Mn and Ce has good potential for developing magnesium casting and wrought alloys. However, little information on the ternary Mg-Mn-Ce system has been published. The main objective of this work is to determine the phase diagram of the Mg-Mn-Ce system in the Mg-rich corner (up to 2.5 wt% Mn and 25 wt% Ce). This work is important for both thermodynamic optimization of the ternary phase diagram and the development of potential magnesium wrought alloys with good formability and of casting alloys with improved creep resistance.

## 5.2 Background

Emley [2] reports two Mg-Mn-Ce ternary polythermal sections with maximum 3wt% Mn and Ce at 0.3 and 1.6wt%, respectively. In these two sections, no ternary compounds are observed. A binary $Mg_9Ce$ compound was so designated due to the expected similarity of the Mg-Ce phase diagram to the Mg-La system, which exhibits the $Mg_9La$ compound. This compound was later determined as the $Mg_{12}Ce$ phase. Recently, Zhang et al [3] have re-designated $Mg_{12}Ce$ as $Mg_{11}Ce$ but with the same crystal structure as $Mg_{12}Ce$. (In the present study, $Mg_{12}Ce$ is used to be consistent with a thermodynamic modeling)

A $Mg_{11}CeM$ ternary compound was reported in the study on Ce-Mg-M systems (where M= V, Cr, Mn, Fe, and Co), which was proposed for use in hydrogen storage [4]. Pearson's handbook [5] subsequently compiled one of the ternary compounds of the study as $Mg_{11}MnCe$ with the lattice parameters measured by the Pezat et al [4]. Close examination of this work [4] reveals that $Mg_{11}MnCe$ is only a chemical formula. The author must have intended to substitute one mole of manganese for one mole of magnesium and measure the hydrogen capacity when a chemical reaction occurred. Their study reports other hydrogen storage materials with different transition metals, but the alloys are still a mixture of $Mg_{11}Ce$ and the transition metals (M). It is interesting to note that $Mg_{12}Ce$ is reported as $Mg_{11}Ce$ but a reason is not given. The existence of this ternary compound and the related lattice parameters should be re-examined. Table 5.1 [5] lists the existing binary compounds of the three binary systems, their crystal structure and lattice parameters. All the compounds are from the Mg-Ce system; no intermetallic compounds are reported in the other two systems.

Table 5.1 Summary of the binary compounds and the crystal structure [5]

| Phase | Crystal system | Reaction type | Structure type | Lattice parameters (nm) |
|---|---|---|---|---|
| Mg | Hexagonal | Melting | Mg | a=0.321, c=0.521 |
| $Mg_{12}Ce$ | Tetragonal | Eutectic | $Mn_{12}Th$ | a=1.033 |
| $Mg_{41}Ce_5$ | Tetragonal | Peritectic | $Mg_{41}Ce_5$ | a=1.454, c=1.028 |
| $Mg_3Ce$ | FCC | Congruent | $BiF_3$ | a=0.744 |
| $Mg_2Ce$ | FCC | Peritectic | $Cu_2Mg$ | a=0.873 |
| MgCe | Simple cubic | Peritectic | ClCs | a=0.390 |
| Mn | BCC | Melting | Mn | a=0.891 |
| Ce | FCC | Melting | Cu | a=0.516 |

## 5.3 Experimental Procedure

Alloy Synthesis

All alloys were synthesized from high purity starting materials. Magnesium ingot (99.96wt%) was supplied by Timminco, Ce (99.7wt%) was supplied by Hefa, and manganese flakes were from Johnson Matthey. Three concentrations of Mn were selected at 0.6, 1.8, 2.5 wt%, and Ce varied between 0 and 25wt%. Alloys containing low levels of Mn and Ce alloys were prepared using a Lindberg electrical resistance furnace; otherwise Norax induction furnace was utilized. In both cases, a $SF_6$+$CO_2$ gas mixture was used as protective gas to prevent Mg and Ce oxidation and burning. The melt was stirred several times before cooling in order to homogenize the compositions. Melting and casting temperatures were in the range of 750~900$^{o}$C.

More than twenty (20) alloys were synthesized and sorted in three (3) polythermal sections, namely: Mg-0.6wt%Mn, Mg-1.8wt%Mn and Mg-2.5wt%Mn. In the remainder of the paper, all composition are given in wt% unless otherwise specified. Fig. 5.1 shows the compositions of the alloys in this ternary system. Chemical compositions were analyzed via Inductively Coupled Plasma Atomic Emission Spectroscopy (ICP-AES) at Genitest Inc (Table 5.2).

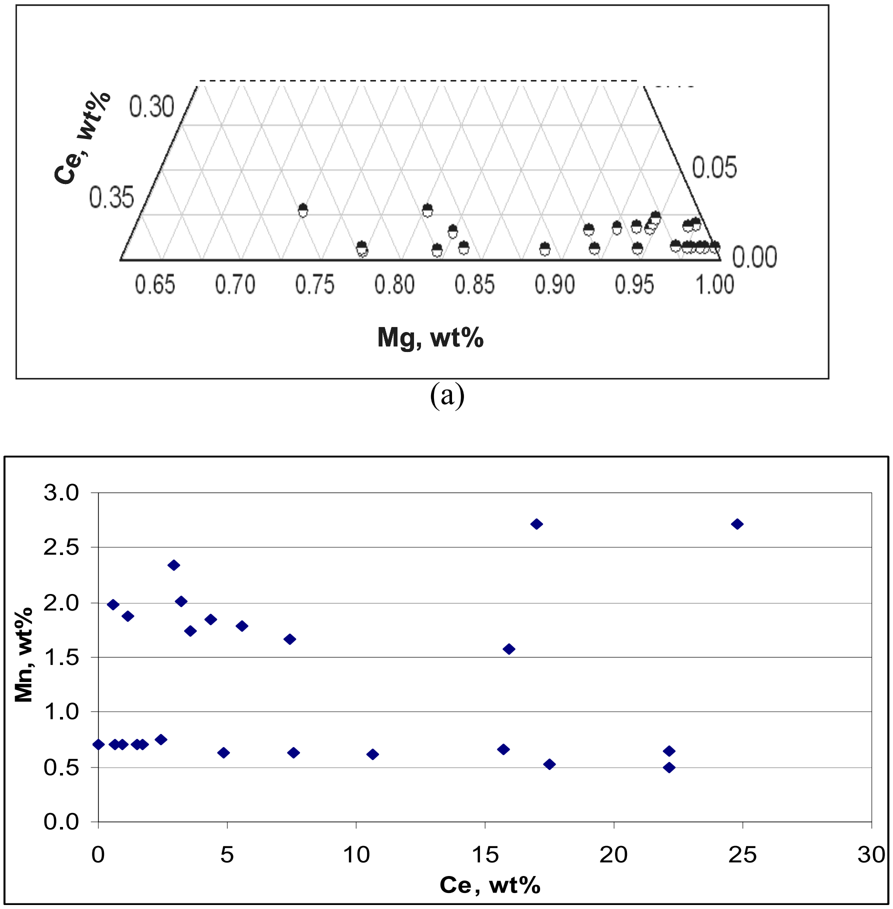

(a)

(b)

*Fig. 5.1(a) Numbers of alloys studied in Mg-Mn-Ce system presented in Mg rich corner, and (b) Numbers of alloys studied in Mg-Mn-Ce system presented in three isopleths.*

Table 5.2 Experimental phase transformation temperatures ($^{o}$C) from CCA and DSC. (Compositions are in weight percent, and parentheses give the standard deviation)

| **Composition (wt%)** | | | | **CCA Thermal Arrests ($^{o}$C)** | | | **DCS Peak ($^{o}$C)** | | |
|---|---|---|---|---|---|---|---|---|---|
| Mg | Mn | Ce | Others total* | 1st | 2nd | avrg 2$^{nd}$ arrest | 1st | 2nd | avrg 2$^{nd}$ arrest |
| *06wt%Mn Isopleth* | | | | | | | | | |
| 99.30 | 0.70 | 0.00 | | 651.6 | | | | | |
| 98.67 | 0.70 | 0.63 | 0.13* | 650.7 | 589.4 | | | | |
| 98.36 | 070 | 0.94 | 0.13* | 649.4 | 589.9 | | 648.7 | 589.2 | |
| 97.79 | 0.71 | 1.50 | 0.03 | 649.8 | 591.3 | | 648.9 | 590.7 | |
| 97.56 | 0.71 | 1.73 | 0.22* | 648.3 | 590.4 | | 647.1 | 590.1 | |
| 96.80 | 0.75 | 2.45 | 0.02 | 647.3 | 591.6 | | 648.9 | 591.4 | 590.4 (1.0) |
| 94.48 | 0.63 | 4.89 | - | 638.6 | 591.0 | | | | |
| 91.82 | 0.63 | 7.55 | - | 633.6 | 591.3 | | | | |
| 88.72 | 0.61 | 10.67 | - | 626.3 | 592.0 | | | | |
| 81.99 | 0.52 | 17.49 | 0.37* | 603.4 | 593.3 | | | | |
| 77.34 | 0.50 | 22.16 | 0.79* | 596.9 | 593.1 | | | | |
| 83.60 | 0.66 | 15.74 | 0.06 | 615.0 | 595.0 | | | | |
| 77.21 | 0.65 | 22.14 | 0.07 | | 593.5 | 591.8 (1.6) | | | |
| *1.8wt%Mn Isopleth* | | | | | | | | | |
| 97.01 | 1.88 | 1.11 | 0.04 | 646.7 | 587.1 | | | | |
| 94.75 | 2.01 | 3.24 | 1.76* | 642.1 | 591.9 | | 642.7 | 590.1 | |
| 94.70 | 1.74 | 3.56 | 0.02 | 641.9 | 590.6 | | | | |
| 93.89 | 1.78 | 4.33 | - | 641.2 | 592.0 | | | | |
| 92.74 | 1.67 | 5.59 | - | 636.9 | 591.1 | | 639.3 | 592.1 | |
| 90.76 | 1.84 | 7.40 | - | 631.2 | 591.8 | | 635.4 | 591.3 | 591.2(1.0) |
| 82.46 | 1.58 | 15.96 | 0.03 | 603.2 | 593.3 | 591.1 (2.0) | | | |
| *2.5wt%Mn Isopleth* | | | | | | | | | |
| 94.75 | 2.34 | 2.91 | 0.07 | 644.3 | 590.5 | | | | |
| 90.03 | 2.58 | 7.39 | 0.08 | 633.0 | 592.0 | | | | |
| 80.32 | 2.71 | 16.97 | 0.22* | 608.5 | 593.0 | | | | |
| 72.51 | 2.71 | 24.78 | 0.09 | 613.9 | 591.6 | 591.8 (1.0) | | | |

* Mostly Fe

Thermal Analysis

Two types of thermal analyses, namely, cooling curve analysis (CCA) and differential scanning calorimetry (DSC), were used to determine the liquidus and the solid phase transformation temperatures. CCA was conducted by inserting a thermocouple, connected to a data acquisition system, into the melt (150-250 g) to monitor the temperature of the alloy as it cools and solidifies. The cooling curve was acquired via a computer-based data acquisition system (Squirrel Data Logger Grant2020) and was presented as temperature versus time. The cooling rate was 9°C/min. DSC was conducted on selected alloys at the controlled cooling rate, 0.5°C/min, in order to cross check the phase transformation temperatures obtained from CCA. Setaram Setsys Evolution$^{TM}$ was used for DSC analysis. Fig. 5.2 presents typical CCA and DSC curves on one alloy showing that two measurements are within 2°C.

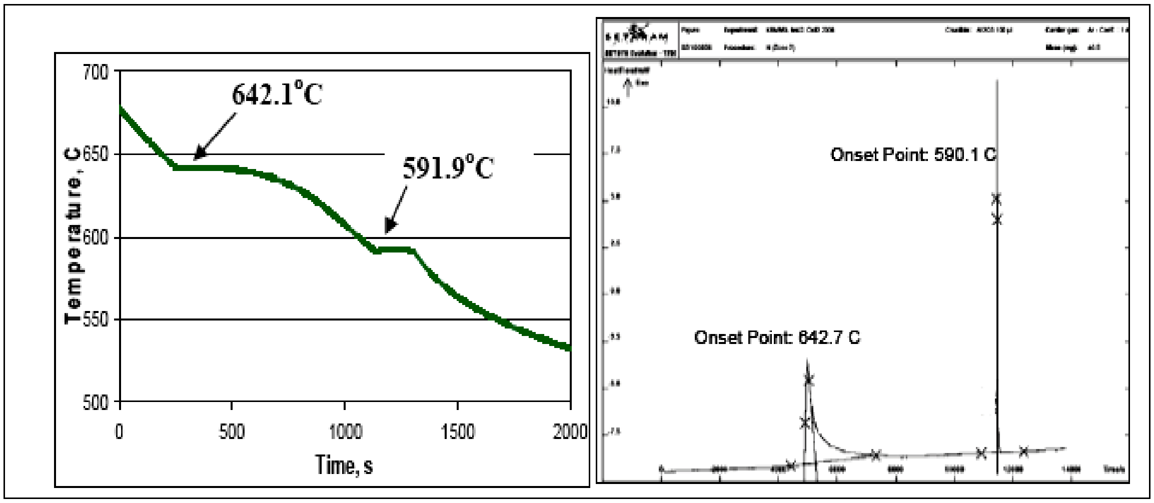

*Fig. 5.2 Thermal analysis of alloy Mg-2.0Mn-3.2Ce from: (a) CCA, and (b) DSC.*

Quench tests

Selected samples from the two isopleths were subjected to heating/quenching tests for phase analysis of the various phase fields. The schematic drawing of the quench-setup is shown in Fig. 5.3.

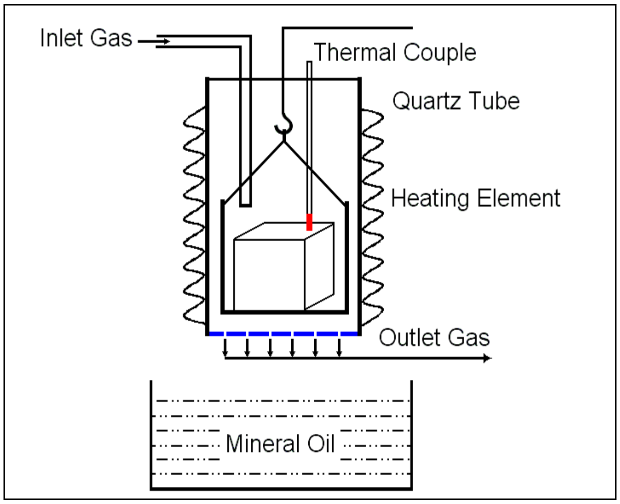

*Fig. 5.3 Experimental set-up for quenching tests.*

The heating temperatures varied with the composition of the alloys. Mineral oil was chosen as the quenching medium to allow for good interface contact between the sample and the cooling medium and for fast heat dissipation (compared to liquid nitrogen), so that very rapid cooling rate could be reached (when compared to CCA). The quenching furnace was also designed to facilitate the tests: a small distance between the heating zone and the quenching container was designed to minimize the time it took for the sample reach the coolant. A thermocouple was inserted in the sample holder to monitor the actual sample temperature before quenching. $SF_6$+$CO_2$ mixture was used as protective gas. When holding at the intended temperature was completed, the hook was shaken to release and immediately drop the sample into the oil.

Microstructure and Phase Identification

All the samples were polished with diamond paste in alcohol to avoid reaction with water. The microstructure was observed via scanning electron microscope (SEM-JEOL 840), and quantitative analysis of the phase composition was conducted with electron probe microanalysis (EPMA-JXA 8900L). X-Ray diffraction (XRD) was carried out for binary/ternary phase identification. The diffractometer, Philips APD 1700, used filtered CuKα radiation, at an accelerating voltage of 40kV and a beam current of 20mA. The measurement was set to a step $0.05^{\circ}$ of $2\theta$ and 3 seconds exposure time at the point. The diffraction pattern was analyzed using XPert Quantify/HighScore. Si was used as an internal standard to correct the systematic errors of the instrument.

## 5.4 Results and Discussion

Thermal Analysis

In all three isopleths, all alloys showed two thermal arrests during solidification in the CCA curves. Two peaks were also revealed in DSC, which corresponded to the two thermal arrests in the CCA. Fig. 5.2 is a typical example for Mg-2.0Mn-3.2Ce alloy. Table 5.2 is the list of the analyses obtained from CCA and DSC for all the alloys tested. DSC measurement on selected samples agrees with the results of CCA. The data indicate that in all the alloys tested, the temperature of the 1st thermal arrest decreases with increasing Ce, until around 22% Ce-0.6% Mn and 17% Ce-2.5% Mn, after which the liquidus temperature increases again. This indicates that a ternary invariant point is close to these compositions and temperature. The binary Mg-Ce system exhibits a eutectic at the 592±2°C and the 2nd thermal arrest of the ternary alloy is very close to this binary eutectic temperature determined in this study.

Microstructure and Phase Identification

Microstructures of the thermal analysis samples which were cooled slowly down to room temperature - as described in the experimental procedure – were investigated via SEM to identify the phases formed at the thermal arrests. Fig. 5.4 shows the microstructures of the alloys at 0.6wt%Mn with varying Ce levels. In alloy Mg-0.71Mn-1.73Ce (Fig. 5.4a) which has low Mn and Ce content, Mg solid solution is surrounded by a Mg-Ce intermetallic in coupled or divorced eutectic morphology. There are also small phases embedded in the primary Mg phase. These are mainly Mn or Mg-Ce intermetallic particles as analyzed via SEM/EDS. With increasing Ce, in the Mg-0.63Mn-7.55Ce and Mg-0.52Mn-17.49Ce alloys (Fig. 5.4b and c), the amount of eutectic phase increases and then it decreases in the Mg-0.50Mn-22.16Ce alloy (Fig. 5.4d). The primary Mg, pure Mn and the Mg-Ce intermetallic phase are in equilibrium in the structure. Fig. 5.5 shows the XRD results of alloy Mg-0.63Mn-7.55Ce and Mg-1.8Mn-5.6Ce. The phases that were detected are Mg, $Mg_{12}Ce$, Mn and Si (internal standard).

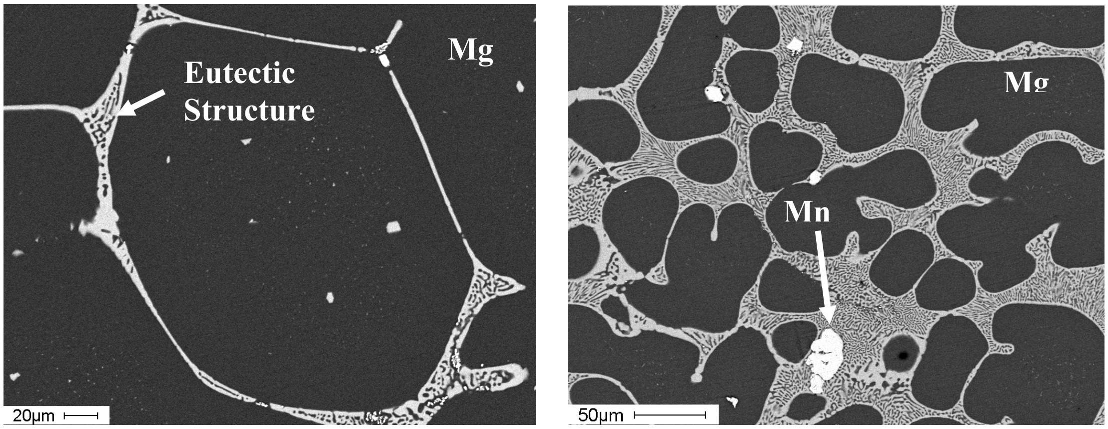

(a) (b)

*Fig. 5.4 As-cast microstructure of alloys at isopleth 0.6%Mn with (a) 1.73%, (b) 7.55% Ce.*

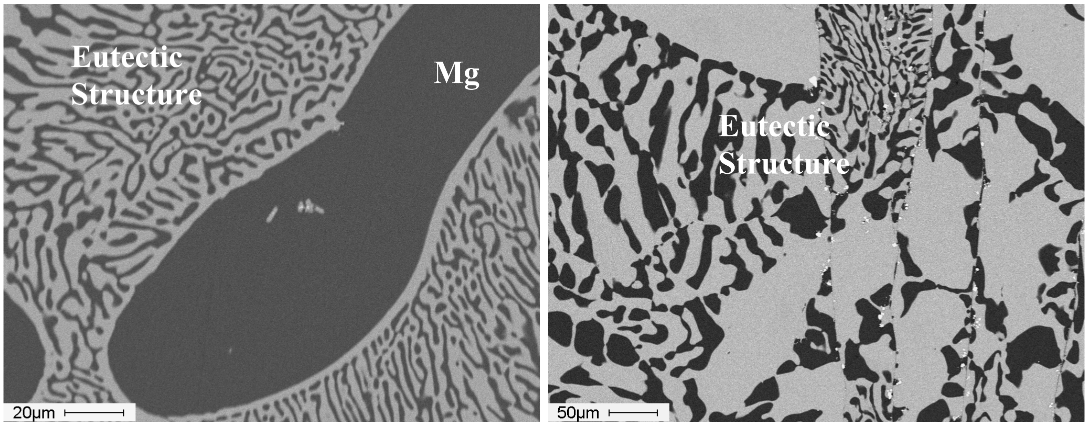

(c) (d)

*Fig. 5.4 (Continued) As-cast microstructure of alloys at isopleth 0.6%Mn with (c) 17.49% and (d) 22.16% Ce.*

Thermodynamic Calculations

Phase diagrams of the binary Mg-Ce and ternary Mg-Mn-Ce alloys were calculated using the FactSage$^{TM}$ [6] thermochemical software with recent thermodynamic modeling parameters for the Mg-Mn-Ce system [7, 8]. All available thermodynamic, phase diagram and phase equilibrium data for solid and liquid phases were critically evaluated and optimized in the thermodynamic modeling. However, slight disagreement between the modeling results and present experimental data especially for the eutectic temperature for $L \rightarrow \alpha\text{-Mg} + Mg_{12}Ce$ was observed. It is noted that the present experimental data were not available when the thermodynamic modeling had been performed. In order to refine the thermodynamic calculations, the Gibbs energy of $Mg_{12}Ce$ was slightly modified (See Appendix I). All the other model parameters were kept as same as the results of Kang et al [7, 8].

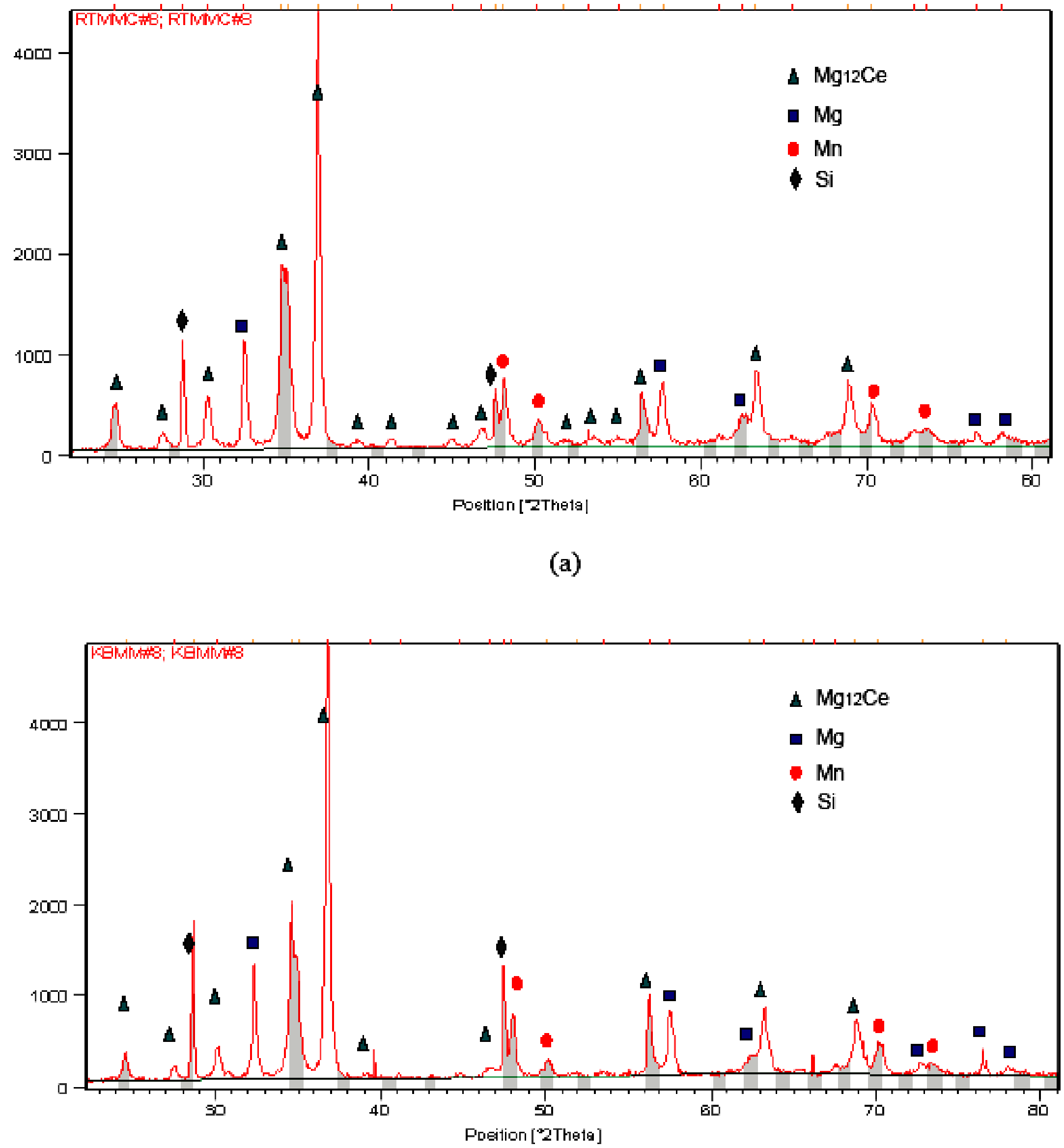

(a)

(b)

*Fig. 5.5 XRD analysis on alloys (a) Mg-0.6Mn-7.55Ce and (b) Mg-1.8Mn-5.6Ce.*

Fig. 5.6 presents the calculated phase diagram of the Mg-Ce system. The dotted lines show the phase diagram calculated using the recent model parameters of Kang et al. [7] and solid lines show the phase diagram calculated in the present study, using the modified Gibbs energy of $Mg_{12}Ce$ solid phase. The major difference is the eutectic temperature for L → α-Mg + $Mg_{12}Ce$, which had not been well measured previously. The experimentally determined eutectic temperature in this study was $592^{o}C \pm 2$, which is well reproduced in the present thermodynamic calculations.

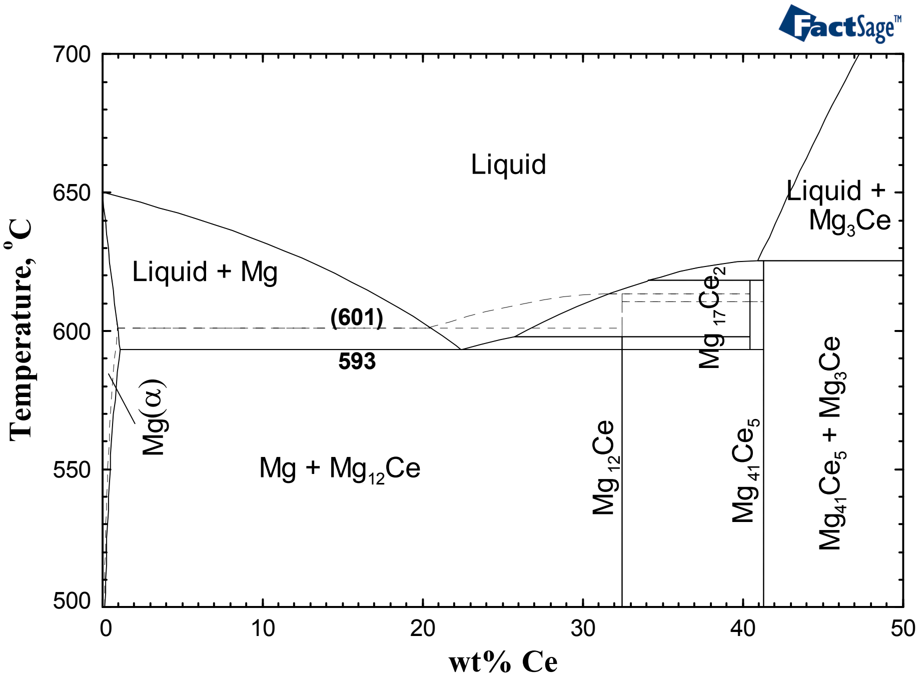

*Fig. 5.6 Calculated Mg-Ce binary phase diagram. Dotted lines are original assessment of Kang et al [7] and solid lines are from calculation in the present study.*

Liquidus Projection of Mg-Mn-Ce System.

The calculated liquidus projection of the ternary Mg-Mn-Ce system is given in Fig. 5.7. As can be seen in Fig. 5.7a, there is liquid miscibility gap in-the Mg-Mn system and it extends up to about 0.2 mole fraction of Ce. The primary α-Mg region is very small, while the primary Mn polymorphs are quite wide. The liquidus surface close to Mg-rich corner is presented in Fig. 5.7b. Two ternary invariant reactions are calculated; eutectic reaction of L → α-Mg + $Mg_{12}Ce$ + Mn at 591°C and peritectic reaction of L + $Mg_{17}Ce_2$ → $Mg_{12}Ce$ + Mn at 595°C. According to this diagram, the primary solid phases for experimental alloys containing 0.6% Mn are α-Mg below 22%Ce and $Mg_{12}Ce$ or $Mg_{17}Ce_2$ above 22% Ce. The primary solid phase for 1.8 and 2.5%Mn alloys is Mn.

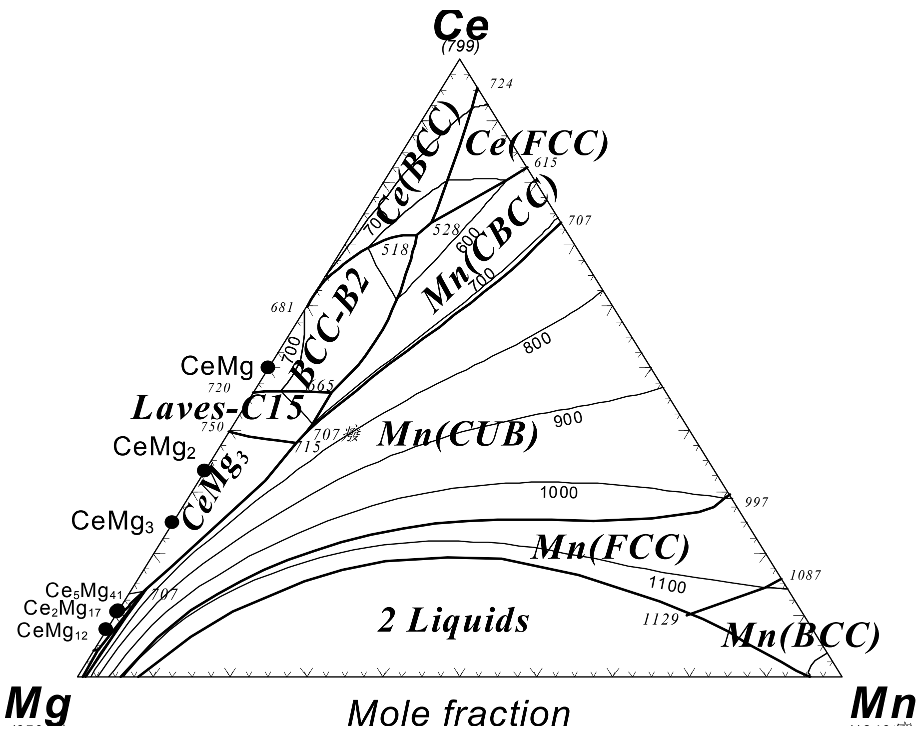

(a)

*Fig. 5.7 (a) Overview of Calculated liquidus projection of ternary Mg-Mn-Ce system in the present study*

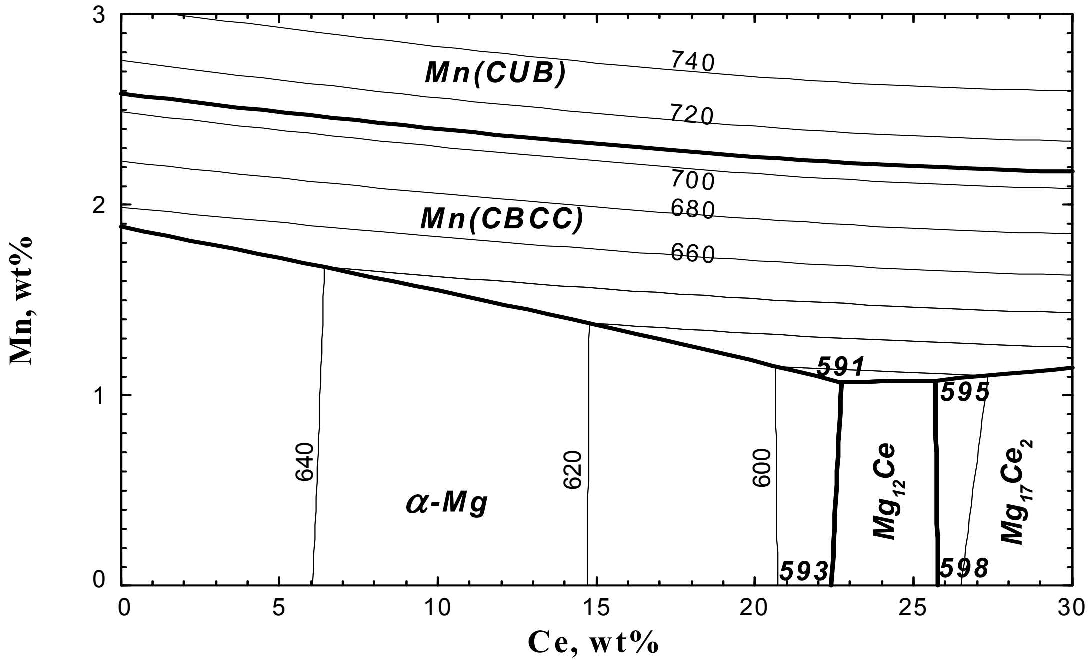

(b)

*Fig. 5.7(Continued) (b) magnified view in Mg rich corner. (Temperature in $^{o}$C)*

Since there are only two thermal arrests in the cooling curves (Table 5.2) and the first thermal arrest can be related to the crystallization of α-Mg, the second arrest could be a eutectic. The presence of both Mn and the Mg-Ce intermetallic in the microstructures (Fig. 5.4b) denotes that the second thermal arrest is related to a ternary eutectic reaction during the solidification.

It has to be noted that the 1$^{st}$ thermal arrest temperature for alloys containing 1.8 and 2.5wt%Mn in Table 5.2 must be liquidus temperature in the L + Mn region. However, it was missed in the present experiment. For example, the liquidus of alloy Mg-2.7Mn-16.9Ce is 739$^{o}$C from FactSage calculation while the first arrest in CCA is 608.5$^{o}$C. This may due to the fact the small amount heat release involved in the precipitation of the Mn primary phase makes it difficult to be experimentally detected. According to the calculations, 0.013g/K of Mn is continuously precipitated from the liquid phase. This precipitation is too small to give the noticeable difference in CCA measurement. On the other hand, the precipitation of α-Mg phase from the liquid at 612°C (608.5°C experimentally measured) can produce exothermic heat of about 0.5kJ for 100 gram alloy by 1 degree K. Thus, the precipitation temperature of Mg phase is easily detected while the formation of Mn was missed in the cooling curve analysis of this study.

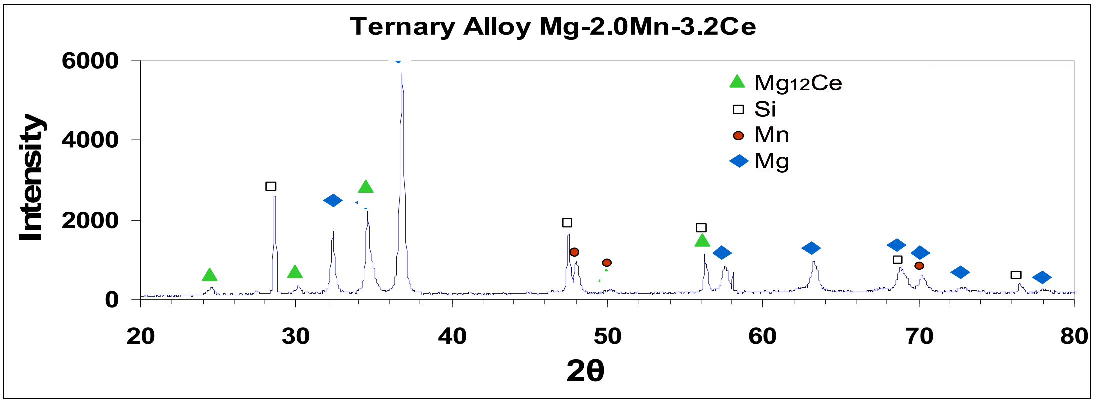

*Fig. 5.8 XRD results for ternary alloy Mg-2.0Mn-3.2Ce revealing the presence of intermetallic compound,* $Mg_{12}Ce$*.*

Fig. 5.8 shows the XRD spectrum for the sample containing 2.0% Mn. Only Mg, Mn, $Mg_{12}Ce$ and Si (internal standard) are detected and there are no unknown peaks. This may mean that either (i) there is no ternary intermetallic compound, or (ii) there is a ternary compound which has the same crystal structure as the binary $Mg_{12}Ce$. Further EPMA results for selected alloys, Mg-0.63Mn-7.55Ce, Mg-0.52Mn-17.49Ce and Mg-0.50Mn-22.16Ce, suggest that about 0.7~0.8 at% Mn can be dissolved to $Mg_{12}Ce$ phase (see Table 5.3). This is in line with the recent results of Zhang et al [3] who re-designated the $Mg_{12}Ce$ as $Mg_{11}Ce$ but with the same crystal structure as $Mg_{12}Ce$, possibly with vacancies occupying the Mg sites. In ternary Mg-Mn-Ce alloys, it can be postulated that the Mn atoms occupy the vacancy/Mg sites of

$Mg_{11}Ce$. In the present thermodynamic calculation, however, this $Mg_{11}Ce$ solid with limited solubility of Mn is treated as $Mg_{12}Ce$ solid compound.

Table 5.3 EPMA results of Mn concentration in $Mg_{12}Ce$ in different alloys

| Alloy Composition* | Mg, at % | Ce, at% | Mn, at% |
|---|---|---|---|
| Mg-0.63-7.55Ce | 91.23 | 7.94 | 0.82 |
| Mg-0.52Mn-17.49Ce | 91.20 | 8.15 | 0.65 |
| Mg-0.50Mn-22.16Ce | 90.77 | 8.41 | 0.82 |

* in weight%

Isopleths

A preliminary isopleth at 0.6%Mn is drawn (Fig. 5.9a) based on thermal analyses results. Thermodynamic calculation for this isopleth is shown in Fig. 5.9b. In Fig. 5.9b, the experimental data are superimposed to compare with the calculation. Fig. 5.10a and b show the calculated isopleths at 1.8 and 2.5%Mn with the superimposed experimental data.

It can be seen that the experimental results correspond well with the thermodynamic prediction in all three isopleths: the liquidus temperatures from the experiment are very close to the calculated phase boundaries, and the eutectic reaction temperature is only a few degrees lower than the calculated value. However, it is also found that some calculations could not be detected by experiment, such as the solid transition line in the 0.6%Mn isopleth and the liquidus line in the 1.8%Mn isopleth. The reason for this is most probably due to the fact that small amount of Mn is continuously precipitated with decreasing temperature through the field. Thus, the latent heat for Mn precipitation from solid and liquid state is too small to be detected by thermal analysis as explained above.

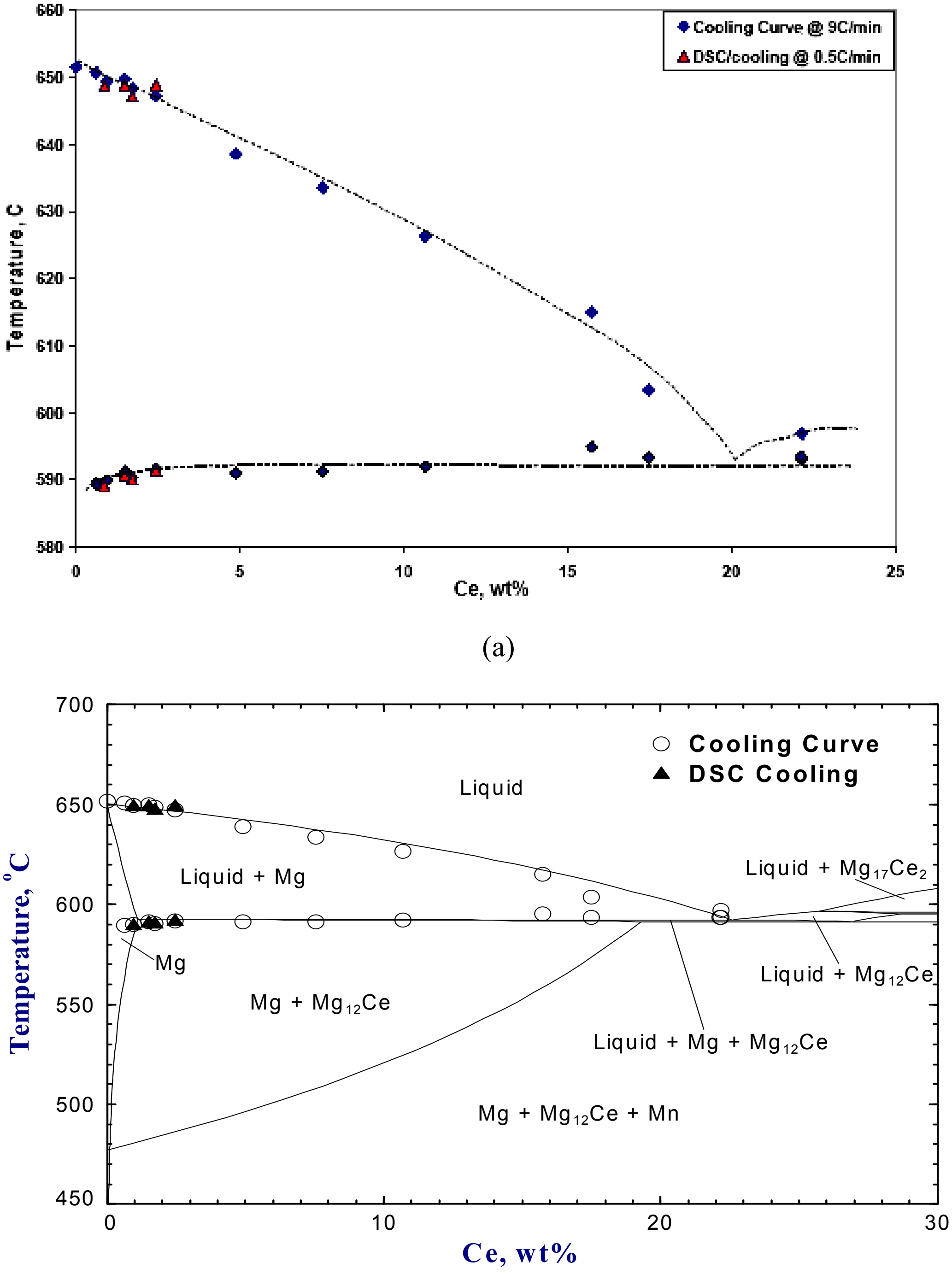

*Fig. 5.9(a) Partial preliminary phase diagram drawn from experimental data of 0.6% Mn isopleths, and (b) calculated isopleths of 0.6% Mn with experimental data.*

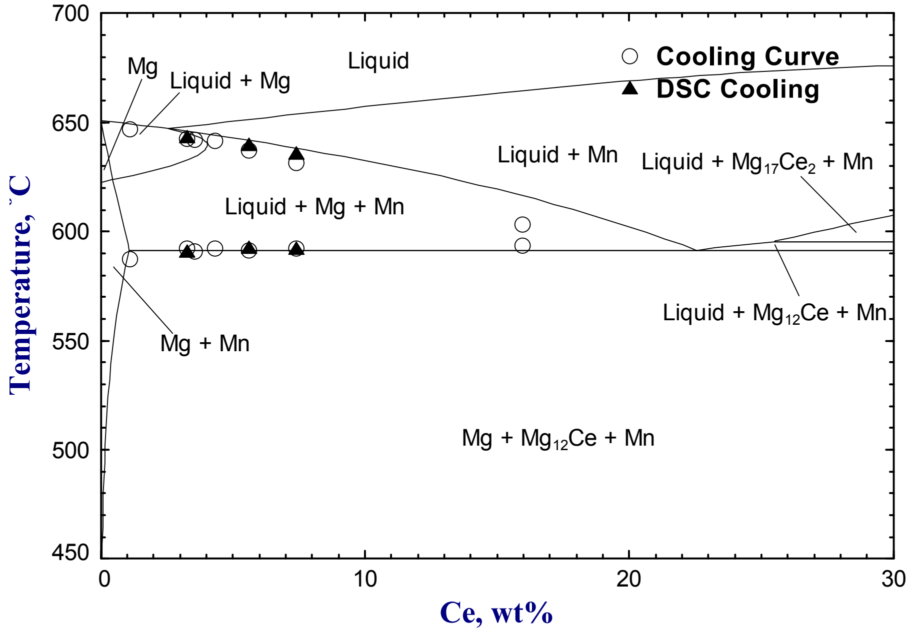

(a)

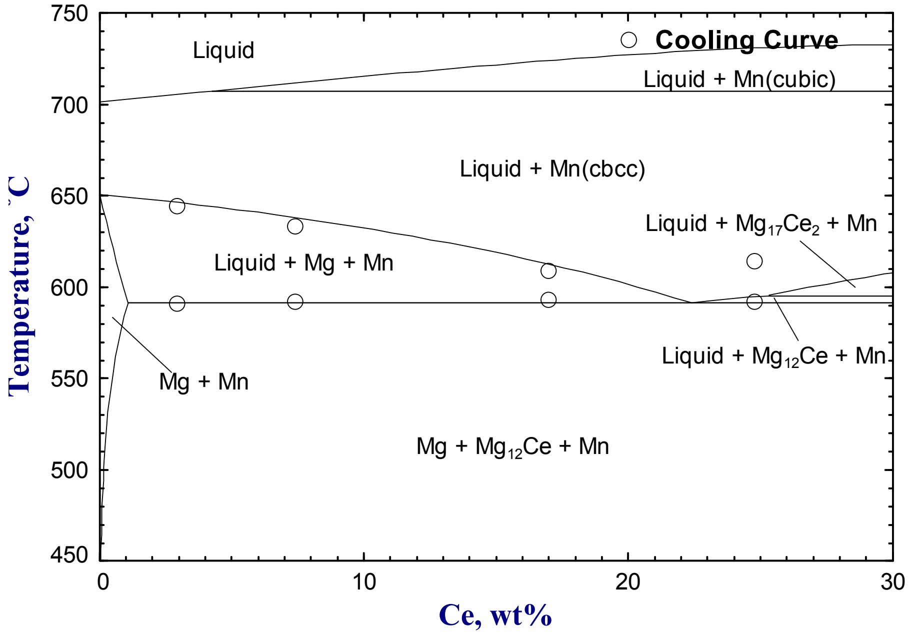

(b)

*Fig. 5.10 (a) Calculated isopleths of 1.8% Mn, and (b) Calculated isopleths of 2.5% Mn with experimental data (Mn stands for complex body centered cubic-Mn).*

Reheat and Quench Tests

The phase fields of the first two isopleths were further determined by conducting quench tests. Three compositions, Mg-0.6Mn-7.6Ce, Mg-1.7Mn-7.4Ce and Mg-1.6Mn-16Ce were chosen, and the microstructures at each quench temperature are presented in Figs. 5.11 to 5.13. The quench tests on binary alloys Mg-7.5Ce and Mg-16Ce were used for comparison with the ternary alloys.

*Mg-0.6Mn-7.6Ce:*

In alloy Mg-0.6Mn-7.6Ce, the quench-test defines the phase fields, and confirms the existence of a phase boundary which appears in the calculated isopleth but which could not be detected via thermal analysis. Fig. 5.11a shows the quenched microstructure of the Mg-0.6Mn-7.6Ce alloy held for 5 hours at 620$^o$C. The structure consists of primary α-Mg and the eutectic structure with Mn in the eutectic region. The light grey, bulk solid phase in the eutectic structure is not a single-phase intermetallic compound, but a very fine eutectic structure, which can be resolved under SEM. This means that the alloy was partially liquid at 620$^o$C with α-Mg phase surrounded by a liquid and when quenched solidified into a very fine eutectic.

The fine eutectic which is Mg + intermetallic analyzed by EPMA (Table 5.4) to give a composition of (Mg, Mn)/Ce= 18.0. The microstructure is similar to the binary alloy quenched from the same temperature (Fig. 5.11e) except for the presence of Mn phase in the ternary alloy. It is understood that the Mn in the ternary alloy is partially precipitated during the quenching of the sample from 620$^o$C. Thus, it can be inferred that the α-Mg and liquid are the equilibrium phases at 620$^o$C for this sample.

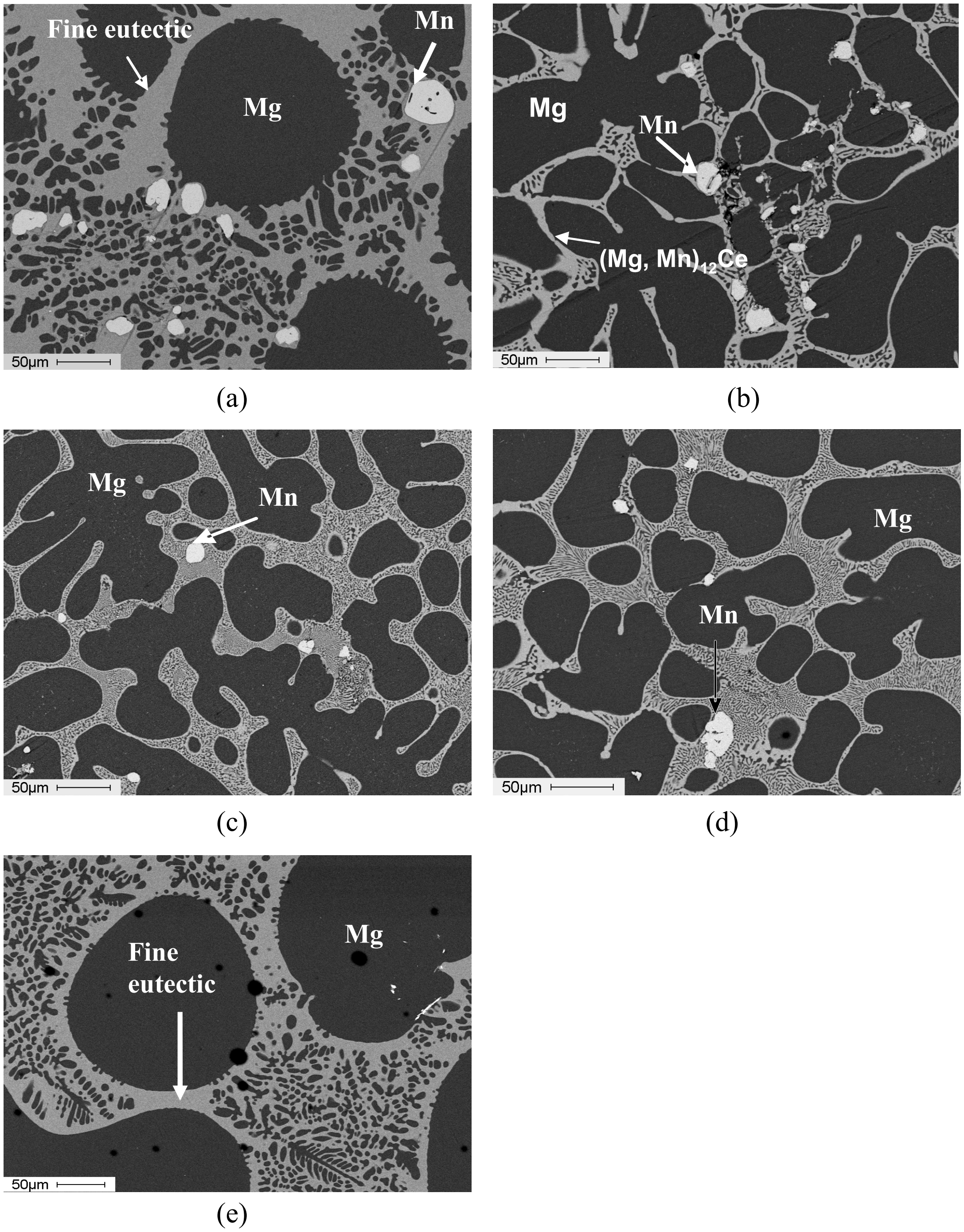

(a) (b)

(c) (d)

(e)

*Fig. 5.11 Microstructures of the alloy Mg-0.6Mn-7.6Ce quenched from (a) 620oC after 5 hrs, (b) 520oC after 5 hrs, (c) 450oC after 20 hrs, (d) The microstructure of ternary Mg-0.6Mn-7.6Ce alloy slowly cooled in furnace, and (e) binary alloy Mg-7.5Ce quenched from 620$^o$C after 5 hrs.*

When the same ternary alloy is quenched from 520°C (Fig. 5.11b), the microstructure consists of primary α-Mg and the eutectic phase with Mn phase particles. In this structure (Fig. 5.11b), the solid phase in the eutectic is the regular intermetallic compound with (Mg, Mn)/Ce=11.7, which means that unlike 620°C no liquid was present at 520°C. When quenched from 450°C (Fig. 5.11c), the microstructure is almost the same as the furnace cooled sample (Fig. 5.11d), with primary Mg, plus the ternary eutectic structure consisting of Mg, Mn and $(Mg, Mn)_{12}Ce$. The EPMA results of the intermetallic compound and the eutectic structure are shown in Table IV.

Table 5.4 EPMA results for $Mg_{12}Ce$ intermetallic compound in various quenched samples

| Alloy* | Quench Temp. (°C) | Mg, at% | Mn, at% | Ce, at% | O, at% | (Al,Fe,Si) at% | Mg/ Ce | (Mg,Mn)/ Ce |
|---|---|---|---|---|---|---|---|---|
| 0.6Mn-7.6Ce | 620 | 93.15 | 0.58 | 5.22 | 1.04 | 0.013 | 17.86 | 17.97 |
| | 520 | 90.67 | 0.60 | 7.83 | 0.89 | 0.012 | 11.58 | 11.66 |
| | 450 | 91.12 | 0.53 | 7.47 | 0.87 | 0.007 | 12.21 | 12.28 |
| 1.6Mn-16Ce | 640 | 93.70 | 0.61 | 4.79 | 0.88 | 0.014 | 19.55 | 19.68 |
| 1.7Mn-7.4Ce | 620 | 92.95 | 0.60 | 5.16 | 1.28 | 0.016 | 18.02 | 18.13 |
| | 450 | 90.88 | 0.33 | 7.90 | 0.87 | 0.018 | 11.50 | 11.54 |

*alloy compositions in wt%.

*Mg-1.7Mn-7.4Ce and Mg1.6Mn-16Ce*

The solidification of Mg-1.7Mn-7.4Ce quenched from 620°C (Fig. 5.12a) and Mg-1.6Mn-16Ce from 640°C (Fig. 5.13a) are different from Mg-0.6Mn-7.6Ce quenched from 620°C. In these alloys, the primary phase in the structure is Mn, which is surrounded by Mg and the eutectic constituent. Both the size and the quantity of this phase are small due to the very limited amount of Mn in this isopleth (1.8wt% Mn). Since both quench tests are conducted from the semi-liquid state, a very fine eutectic structure formed at (Mg, Mn)/Ce= 18.0 and 19.7, respectively (Table 5.4).

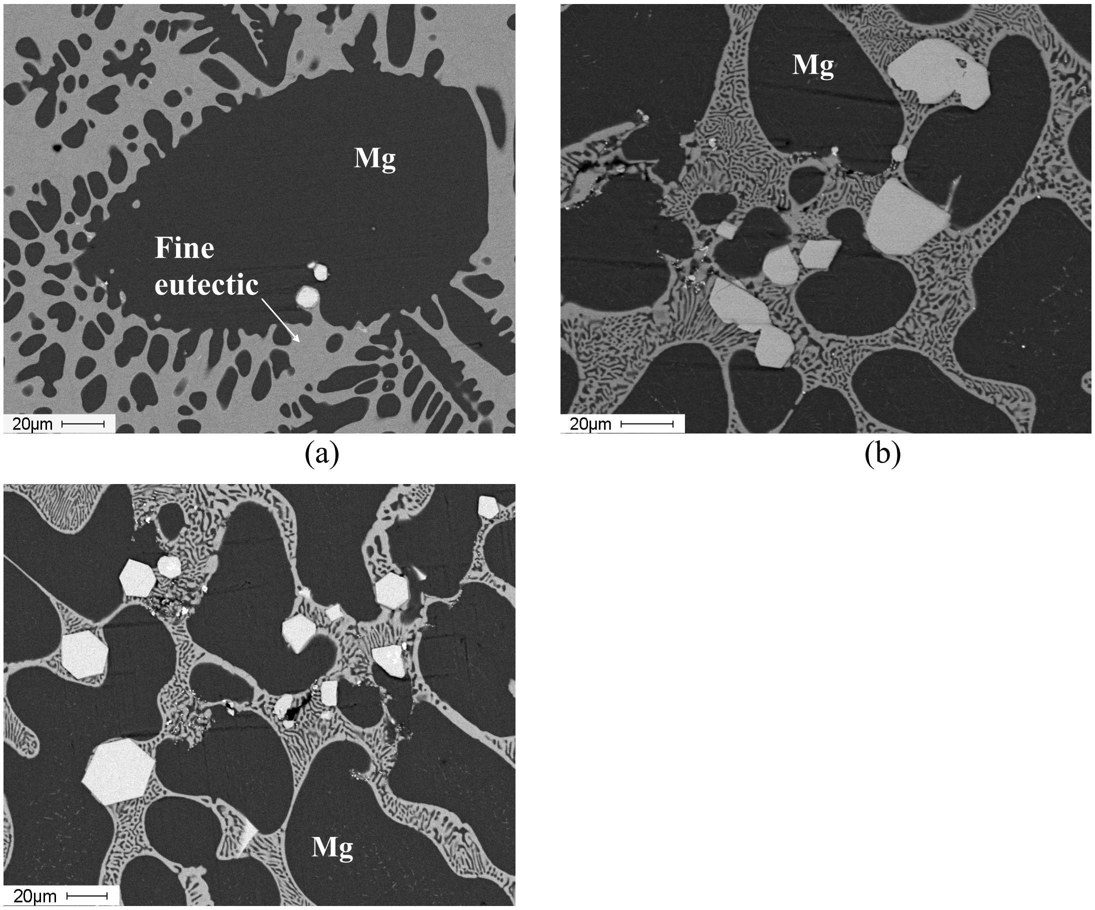

(a) (b)

(c)

*Fig. 5.12 Microstructures of the alloy Mg-1.7Mn-7.4Ce quenched from (a) 620*$^{o}$*C after 5hrs, (b) 450*$^{o}$*C after 20 hrs. (c)The microstructure of the same alloy sample slowly cooled in furnace.*

The quenched microstructure of alloy Mg-1.7Mn-7.4Ce from the solid state at 450$^{o}$C is similar to its furnace cooled sample (Fig. 5.12b and c) with a typical eutectic structure surrounding the Mg phase. It should be noted that the composition of alloy Mg-1.6Mn-16Ce is very close to the ternary eutectic composition, therefore most of the structure in Fig. 5.13 is eutectic. The results tell that there is a ternary eutectic involving L → α-Mg + Mn + $Mg_{12}Ce$ around 22% Ce and 1% Mn. The eutectic temperature is around 591$^{o}$C based on experimental results. According to the thermodynamic calculations, the eutectic reaction occurs at a composition of Mg-1.07Mn-22.72Ce (in wt%) and at 591$^{o}$C, which is in good agreement with the present experimental results.

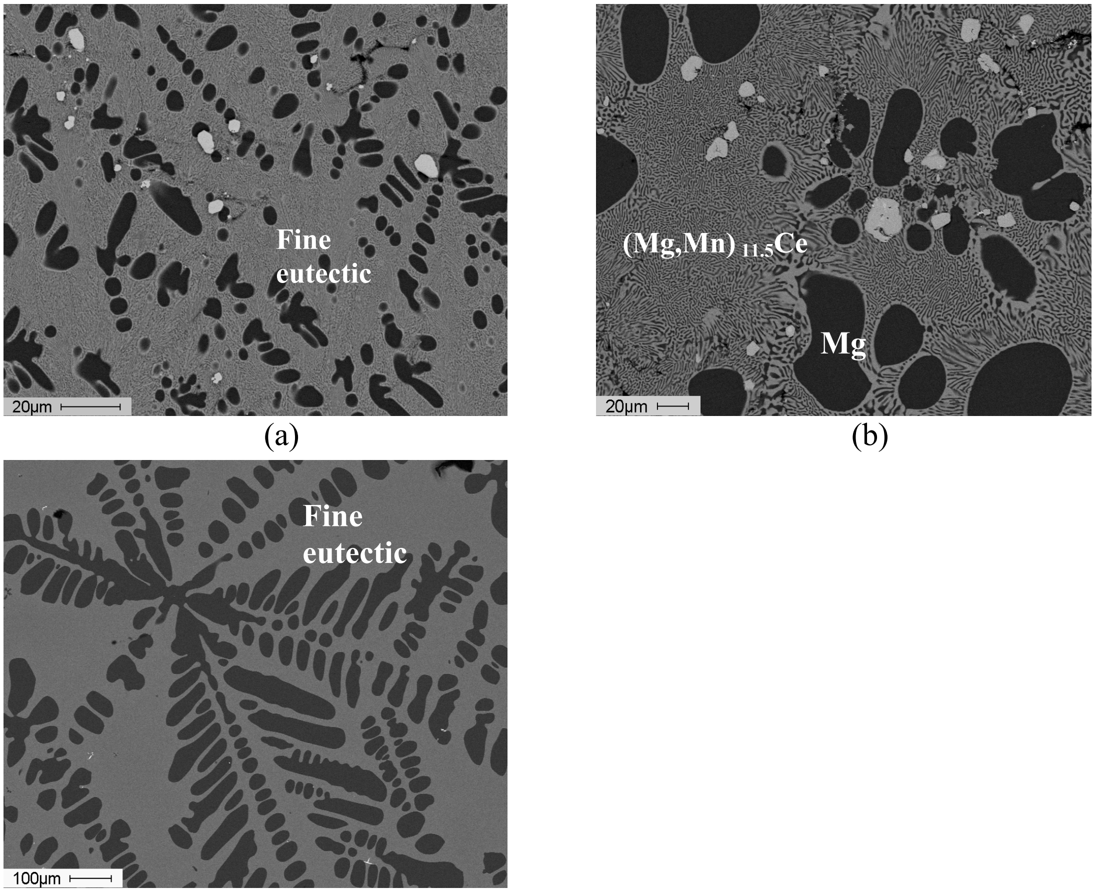

(a) (b)

(c)

*Fig. 5.13 Microstructures of the alloy Mg-1.6Mn-16Ce quenched from (a) 640$^{o}$C after 5hrs, and (c) binary alloy Mg-16Ce quenched from 620$^{o}$C after 5 hrs. (b) The microstructure of the Mg-1.6Mn-16Ce alloy sample slowly cooled in furnace.*

## 5.5 Conclusions

1. The ternary eutectic temperature in the Mg-Mn-Ce in the Mg-rich corner is at 591°C and the eutectic composition is 1wt% Mn and 22wt% Ce.
2. The composition and the temperature of the ternary invariant are very close to the eutectic invariant of L → $\alpha$-Mg+$Mg_{12}Ce$ in the binary Mg-Ce system.
3. A solid-solution type of ternary intermetallic compound $(Mg, Mn)_{12}Ce$ is formed, holding the same tetragonal structure as $Mg_{12}Ce$. The solid solution of Mn in $Mg_{12}Ce$ varies between 0.3~0.6 at%, depending on alloy composition and quenching temperature.
4. In order to reproduce the experimental results, the Gibbs energy of $Mg_{12}Ce$ phase is reoptimized and the revised data can accurately reproduce the experimental results within experimental error limits.

## Appendix I Reassessment of the Gibbs Energy of $Mg_{12}Ce$ Phase.

Recently, Kang et al [7, 8] have performed the thermodynamic modeling of the binary Mg-Ce and ternary Mg-Ce-Mn alloy systems. This study found that the calculated eutectic temperature for L → $\alpha$-Mg + $Mg_{12}Ce$ from their model parameters is consistently higher than the present experimental data by 8°C. Thus, in order to reproduce the present experimental data better, the Gibbs energy of $Mg_{12}Ce$ was slightly adjusted as follows:

$$G_{Mg_{12}Ce} = H^{o}_{298.15} + \int_{298.15}^{T} \mathrm{Cp}\,dT - T[S^{o}_{298.15} + \int_{298.15}^{T} (\mathrm{Cp}/T)dT]$$

The value of $H^{o}_{298.15}$ of $Mg_{12}Ce$ was changed from -139880 J/mol to -137580 J/mol (+ 2.3 kJ/mol). The values for enthalpy at 298 K ($S^{o}_{298.15}$) and heat capacity ($Cp$) are kept the same. All the other model parameters for other phases were kept as same as the results of Kang et al [7, 8].

## 5.6 References

1. K. Grube, J.A. Davis, L.W. Eastwood, J. Inst. Met., 88 (1959-60) 417.
2. E. F. Emley, Principles of Magnesium Technology, Pergamon press Ltd., London, 1966.
3. X. Zhang, D. Kevorkov, M. Pekguleryuz, J. Alloys Compd. (2008), doi:10.1016/j.jallcom.2008.07.042.
4. M. Pezat, A. Hbika and B. Darriet, Materials Research Bulletin, 15 (1980) 139-146.
5. P. Villars and L.D. Calvert, Pearson's Handbook of Crystallographic Data for Intermetallic Phases, 2nd ed., Materials Park, OH: ASM International, 1991.
6. C.W. Bale, P. Chartrand, S.A. Degterov, G. Eriksson, K. Hack, R.B. Mahfoud, J. Melançon, A.D. Pelton and S. Petersen: Calphad, 26 (2002), 189-228.
7. Y.-B. Kang, A.D. Pelton, P. Chartrand, P. Spencer, C.D. Fuerst, J. Phase Equil. Diff., 28 (2007), 342-354.
8. Y.-B. Kang, A.D. Pelton, P. Chartrand, P. Sepncer, C.D. Fuerst, Metall. Mater. Trans. A, 38A (2007) 1231-1243.

# CHAPTER 6

# CONCLUSIONS

An experimental investigation of the Mg-Mn-Ce system complemented by thermodynamic assessment, where necessary, was undertaken. Since the ternary phase diagram calculation is based on the accuracy of the binaries, an investigation of the three binary systems, Mg-Ce, Mg-Mn and Mn-Ce was carried out to determine and to clarify the type of phases, phase stoichiometry and their compositional ranges. By means of diffusion couple technique, microstructure observation (SEM/EPMA) and XRD method, and thermodynamic calculations, the following conclusions were drawn:

*Mg-Mn and Mn-Ce Systems*

1. It has been confirmed that there is no intermetallic compound formation in either Mn-Ce or Mg-Mn binary system as determined via the diffusion couple method.
2. The calculated binary Mn-Ce system carried out with FactSage is in good agreement with experimental result.

*Mg-Ce System*

3. In the Mg-Ce system, the $Mg_{12}Ce$ has been re-designated as $Mg_{11}Ce$ at 8.5at% Ce. Its new compositional range is $Mg_{(11.17-10.81)}Ce$ at ambient temperature and

$Mg_{(11.31-10.75)}Ce$ at 530°C. It is postulated that the phase is a defect structure of $Mg_{12}Ce$ with vacancies substituting Mg sites.

4. The position of line compound $Mg_{41}Ce_5$ was re-designated as $Mg_{39}Ce_5$ and its composition is relocated from 10.9at% to 11.3at% Ce.

5. A new phase, $Mg_4Ce$, at Ce-rich side was found with the composition of $Mg_{3.6-3.7}Ce$.

6. $\mu$-$Mg_3Ce$ is considered as metastable form of $Mg_3Ce$ with a possible orthorhombic structure.

7. Based on the above study, a new version of Mg-Ce system in the composition range of 35-70 wt% Ce is suggested in this work.

*Mg-Mn-Ce System*

1. At the Mg-rich corner of the Mg-Mn-Ce system, only one invariant point exists. It is eutectic type $L \rightarrow \alpha\text{-}Mg+Mg_{12}Ce+Mn$.

2. The composition and the temperature of the ternary invariant are very close to the eutectic invariant in the binary Mg-Ce system. The ternary eutectic composition is 1wt% Mn and 22wt% Ce. The eutectic temperature is at 591°C.

3. A ternary intermetallic compound is formed which a solid-solution type, $(Mg,Mn)_{11}Ce$, which has the same tetragonal structure as binary $Mg_{12}Ce$ as revealed by XRD. Quench test shows the solid solution of Mn in $Mg_{11}Ce$ varies between 0.3~0.6 at%.

4. Ternary phase diagram at Mg-rich corner is calculated in the format of three isopleths: 0.6, 1.8, and 2.5wt% Mn. The Gibbs energy of $Mg_{12}Ce$ is re-

optimized because the difference between the experimental results and the calculation. This evaluation can accurately reproduce the experimental results within the error limits.

*Recommendations for Future Work*

1. In the binary Mg-Ce system, it is recommended that samples in the range of 35-70 wt% Ce be exposed to long-term annealing (prolonged annealing time on highly vacuum-sealed samples). There are two advantages in doing this: firstly to attain equilibrium and investigate the stability of the $Mg_{3.6}Ce$ and μ-$Mg_3Ce$ intermetallic phases, and secondly to allow the intermetallic crystals to grow so that particles can be collected for XRD to determine the crystal structures.
2. It is also recommended to thermodynamically model the Mg-Ce system based on the new suggested phase diagram.
3. In the ternary Mg-Mn-Ce system, key experiments beyond the Mg-rich corner should be conducted to evaluate the thermodynamic parameters.
4. The selection of key experiments should be based on the calculated ternary phase diagrams, so that the phase boundaries and phase stoichiometry can be determined via diffusion couple and annealing/quenching tests. TEM can be involved if unknown phases are detected.

# CHAPTER 7

## CONTRIBUTIONS TO ORIGINAL KNOWLEDGE

The major contributions of the study are two-fold:

(A) The refinement of the Mg-Ce binary system with respect to intermetallic phase compositions and boundaries; the discovery of metastable in termetallics that occur in the Mg-Ce system; and a first-time thermodynamic study of the Ce-Mn system.

(B) A first-time experimental (thermal analysis, SEM/EPMA) and thermodynamic computational study of the Mg rich corner of the Mg-Mn-Ce system.

(A) In the Mg-Ce binary system, the existing binary phase diagram is:

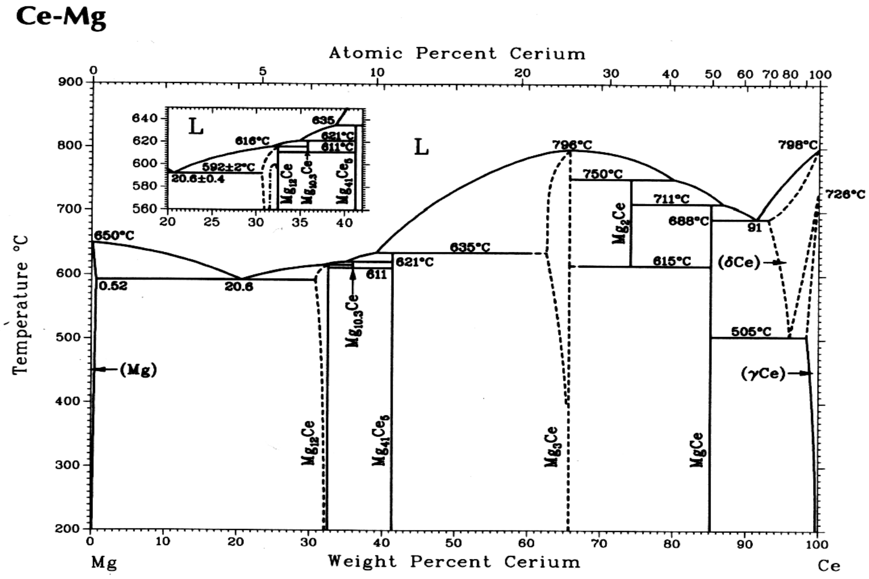

A revised phase diagram is suggested from present work as follows:

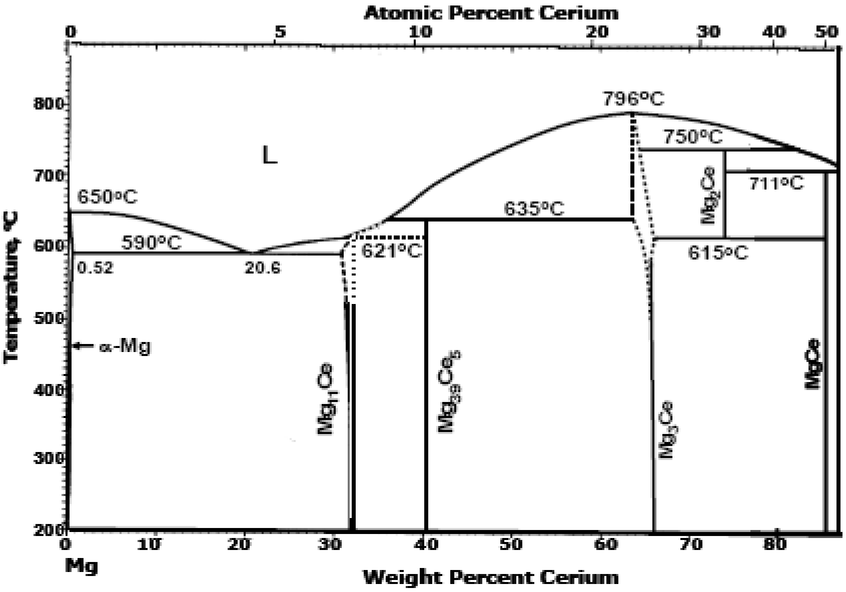

*Fig. 4.25 Revised Mg-Ce phase diagram up to 50at% Ce.*

1. The stoichiometry of compound $Mg_{12}Ce$ was redesignated as $Mg_{11}Ce$ with a new composition range in the Mg-Ce binary system. The occurrence of the stable $Mg_{11}Ce$ as a possible vacancy defect structure is interesting for Mg alloy development (e.g. certain alloying elements in the alloy may dissolve in the intermetallic at different temperatures and influence the thermal/microstructural stability)

2. $Mg_{39}Ce_5$ has replaced $Mg_{41}Ce_5$ as a stable and possible vacancy defect structure.

3. The $Mg_{10.3}Ce$ phase is removed because this high temperature phase was not confirmed by the previous study (whose study? Give reference) and in the present study as $Mg_{11}Ce$ right border is very close to the $Mg_{10.3}Ce$; therefore the presence of another phase is questionable without further study.

4. $Mg_3Ce$ was found to have a high temperature metastable phase μ-$Mg_3Ce$ with a possible orthorhombic structure.

5. A new compound $Mg_4Ce$ was determined as a defect-vacancy structure of $Mg_3Ce$ and is important for hydrogen storage. The diffusion couple data show that this is a metastable phase that occurs in the as-cast alloys.

6. First time thermodynamic optimization on the Ce-Mn system shows good agreement between the experimental phase diagram and the calculated one. However, it also shows the weakness of R-K model that the ordering (minimum at enthalpy and entropy) is naturally occurring at 1/1 ratio of Mn/Ce due to the random mixing entropy term. Later on the quasi-chemical model was applied and predicted the minimum quite well.

(B) In the Mg-Mn-Ce ternary system

6. Mg-Mn-Ce ternary phase diagram was first time studied experimentally via thermal analysis and SEM/EPMA in the Mg-rich corner.

7. The Mg-rich corner of Mg-Mn-Ce ternary system was first time studied thermodynamically via FactSage program based on the experimental data.

8. With the aid of thermodynamic modeling and experiments, a revised phase diagram for the binary Mg-Ce system and the isopleths of 0.6, 1.8 and 2.5wt% Mn were proposed up to 25wt% Ce.

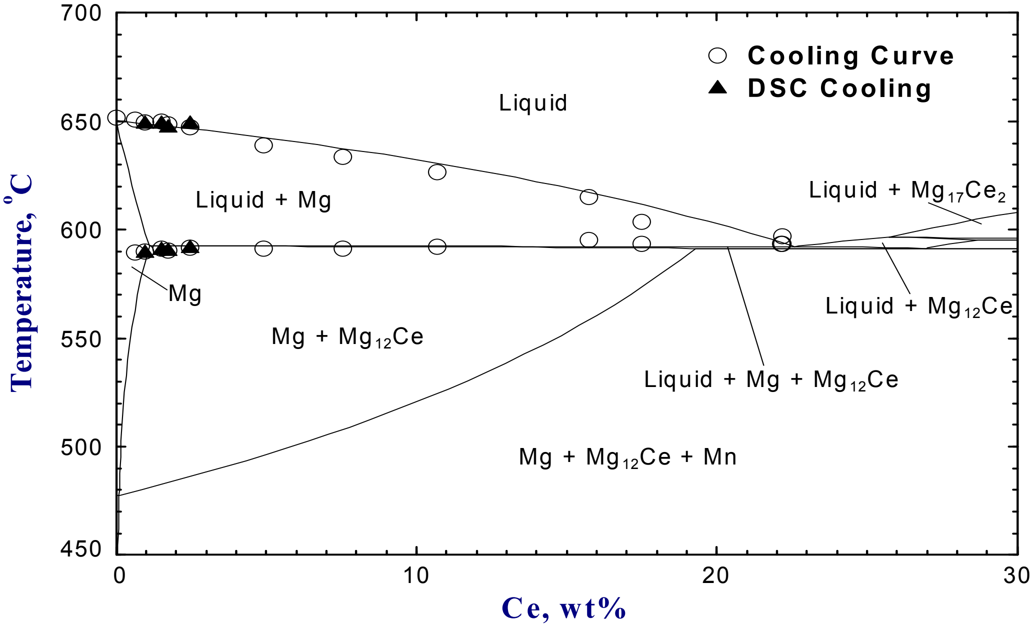

*Fig. 5.9(b) calculated isopleths of 0.6% Mn with experimental data.*

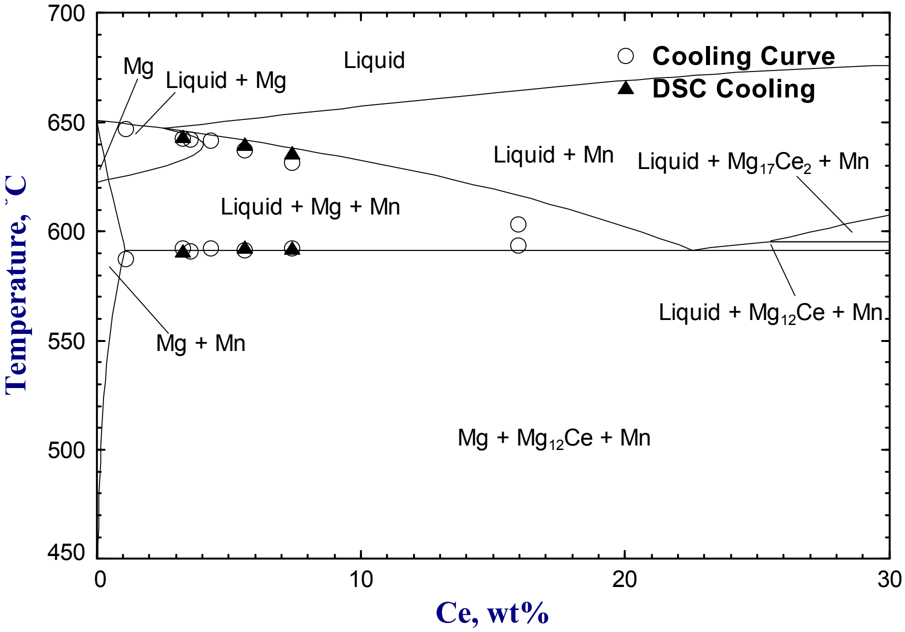

*Fig. 5.10 (a) Calculated isopleths of 1.8% Mn with experimental data.*

# APPENDIX

## SIGNED WAIVERS FROM ANY CO-AUTHORS OF UNPUBLISHED MANUSCRIPTS